INTERFEROMETRIC FIBER SENSORS BASED ON THE MICROSTRUCTURE FIBERS

LI YUJIAN

PhD

The Hong Kong Polytechnic University

2025

The Hong Kong Polytechnic University

Department of Electrical and Electronic Engineering

Interferometric fiber sensors based on the microstructure fibers

Li Yujian

A thesis submitted in partial fulfillment of the
requirements for the degree of Doctor of Philosophy

June 2024

Certificate of Originality

I hereby declare that this thesis is my own work and that, to the best of my knowledge and belief, it reproduces no material previously published or written, nor material that has been accepted for the award of any other degree or diploma, except where due acknowledgment has been made in the text.

(Signed)

Li Yujian (Name of student)

Abstract

In this thesis, the fiber interferometric sensors based on micro-structure fiber are studied for different applications.

First, the fundamental knowledge about optical fiber, including history, structure, modes in fiber, and categories are introduced in detail to give a basic understanding of optical fiber. Next, the working mechanism, advantages, and classification of the optical fiber sensors are presented one by one to get e general view of this study topic. Then, based on the principles of optical interference, the working principles and common fiber interferometer structures are induced and introduced clearly to provide essential knowledge for the following sub-chapter. Also, the Optical Vernier Effect (OVE) is introduced to improve the sensing performance of the single interferometric sensor.

For the sensing device part, four different interferometric structures are proposed and demonstrated availability. The optimal fabrication process and parameters are presented in detail after several experiments. The experimental results of the spectrum and sensitivities all coincided with theoretical analysis. The first sensor is proposed for lateral stress measurement based on the Sagnac interferometer (SI) structure. The six-hole high birefringence fiber is used to detect the lateral stress

change based on the stress-caused birefringence effect. The sensitivity is about 1.72 nm/kPa. Because there are no doped particles in the fiber, the sensor is temperature insensitive. In addition, employing single wavelength laser injection and light intensity demodulation method, this SI sensor can monitor the heartbeat and breath rate. The second sensor is an axial strain sensor based on the Mach-Zehnder interferometer (MZI) structure. In this structure, the twin-core single hole is used to provide a transmitting channel for the MZI between the core light and the hole light. Based on the elastic-optical and tensile deformation effects, this structure can measure the axial strain with a sensitivity of 0.59 pm/με. To enhance the sensitivity, two sensor structures are cascaded in series to motivate the OVE. The cascaded structure can amplify sensitivity about 30 times. Furthermore, this cascaded structure enables simultaneous sensing of axial strain and temperature within the acceptable error range. Additionally, a third sensor is introduced for gas pressure measurement, utilizing a Fabry-Perot interferometer (FPI) structure. The main detection element of this sensor is single-core side-hole fiber with several micrometers, leveraging the refractive index change of the air hole induced by gas pressure. Due to the OVE, the proposed sensor has an ultra-high sensitivity of 183 nm/MPa in 0~100 kPa. This sensor is also sensitive to temperature change with a sensitivity of 440 pm/℃. Then, the temperature cross-sensitivity can be calculated as -2.4 kPa/ ℃, which is relatively low. The last sensor is proposed for the lateral stress measurement based on the Michelson interferometer (MI) structure. Different from the traditional MI structure, a section of Panda PMF is used in one of the two arms to motivate the OVE. The normalization sensitivity of it is about 3.76 nm/(kPa·m). Using FBG as a temperature compensation element, temperature fluctuation is monitored and demodulated to achieve no temperature cross-sensitivity usage.

The four sensor structures are all investigated having promising applications in different fields to provide convenience for human beings.

Acknowledgments

When I click the thesis submission button, my Ph.D. study ends officially. Although there has been anxiety and confusion, I had a great study experience during the past three years. I am happy I can get a Ph.D. degree at PolyU.

The first person I want to express appreciation to is my supervisor, Professor Yu Changyuan. Without his help, I may not have had the opportunity to apply for the Ph.D. admission. During my Ph.D. study process, he gave me the greatest freedom in scientific research. Whenever I had a new idea, he always encouraged me to give it a try. Prof. Yu also shows great care in my daily life, especially during the epidemic period. I will never forget the help and support from Prof. Yu during my Ph.D. study.

I also met a lot of interesting people. Dr. Yuan Weihao once helped me revise the journal manuscript sentence by sentence. I have learned many skills from him. Now, he is already a professor at the university. Wish he has a happy life. My senior schoolmates Dr. Wang Zhuo, Dr. Chen Shuyang, Dr. Luo Huaijian, Dr. Yang Zongru, Dr. Liu Yifan, and Dr. Qu Jiaqi help me a lot when I first arrived in Hongkong. Wish them a promising future. I will continuously remember when I stayed with my peer schoolmates Liu Zhongxu, Lyu Weimin, Chen Jiajian, and Zhou Jing. The two international conference journeys with Weimin Lyu impressed me very much. The other research group's teammates Cheng Zhi, Wang Yue, Xupin, Cui Mingjie, Zhang Jingming, and Wang Qing help to create a wonderful study and live atmosphere at PolyU. I enjoyed the time I spent with them.

My friends in Wuhan Qing, Ming, and Xi gave me lots of support and encouragement. I wish they would have a happy life. I must thank my best friend in Shen Zhen, Wei Chuang. His friendship makes me feel not lonely. We talked about everything. I wish he had found the correct person earlier. I owe my parents a great deal because they have devoted most of their time and energy to cultivating me. I hope they are healthy and happy forever.

The most important person for me is my significant other, who said to me on the way we went to the railway station “Don’t worry, please just regard studying in Hong Kong as one individual trip. Just enjoy the food and scenery of Hong Kong. I will offer overall protection for your future life even if you cannot graduate. Do not let yourself bear too much pressure.” At this moment, no words can express my love. We will stay with each other for the rest of our lives.

Finally, I want to thank everyone who ever helped me during my Ph.D. study.

Publications

Journal:

1. **Y. Li**, P. Xu, W. Lyu, Y. Liu and C. Yu, “Fiber Lateral Stress Sensor Based on Michelson Interference and Optical Vernier Effect,” ***Journal of Lightwave Technology***, early access, doi: 10.1109/JLT.2024.3382105.
2. **Y. Li**, W. Yuan, Y. Liu and C. Yu, “An Ultrasensitive Gas Pressure Sensor Based on Single-core Side-hole Fiber with Optical Vernier effect,” ***Journal of Lightwave Technology***, vol. 41, no. 13, pp. 4509-4515, July 2023.
3. **Y. Li**, Y. Liu, W. Yuan, C. Yu, “Simultaneous Measurement of Strain and Temperature Based on Twin-core Single-hole Fiber with Optical Vernier effect,” ***Optics Express.*** vol. 31, no. 2, pp. 1705-1720, January 2023
4. **Y. Li**, Z. Liu, Y. Liu, C. Yu, “Simultaneous measurement of axial strain and lateral stress based on cascaded interference structure,” ***Optics Express***, vol. 30, no. 7, pp. 10942-10952, March 2022
5. **Y. Li**, P. Lu, C. Yu, “An Optical Fiber Sensor for Axial Strain, Curvature, and Temperature Measurement Based on Single-Core

Six-Hole Optical Fiber," ***Sensors***, vol. 22, no. 2, pp.1666.1-13, February 2022

6. Y. Liu, ***Y. Li***, P. Xu, W. Yuan, and C. Yu, "Simultaneous measurement of direction-recognizable curvature and temperature based on Symmetry exposing tilt FBG," ***IEEE Sensors Journal***, vol. 24, no. 3, pp. 2836-2843, February, 2024.
7. P. Xu, Y. Liu, A. A. Noman, X. Cheng, ***Y. Li***, and C. Yu, "Rapid and sensitive detection of aqueous ammonia harnessing nanocomposite functionalized tilted fiber Bragg grating," ***Optics Express***, vol. 31, no.17, pp. 27095-27105, July 2023 (Q1)

Conference paper:

1. ***Y. Li***, W. Lyu, Z. Liu, W. Yuan, and C. Yu, "Optical Fiber Gas Pressure Sensor Based on the Michelson Interferometer with Optical Vernier Effect," ***28th International Conference on Optical Fiber Sensors*** (OFS-28), Hamamatsu, Japan, November 20 to 24, 2023.
2. ***Y. Li***, P. Xu, W. Lyu, Y. Liu, and C. Yu, "Optical Fiber Lateral Stress Sensor Based on Michelson Interference and Optical Vernier Effect," ***28th International Conference on Optical Fiber Sensors*** (OFS-28), Hamamatsu, Japan, November 20 to 24, 2023.

3. ***Y. Li***, W. Lyu, Y. Liu, C. Yu, "Acoustic wave sensor based on the optical fiber-diaphragm composite structure," ***Photonics Global Conference*** (PGC) 2023, Stockholm, Sweden, August 21 to 23, 2023 (**Best Student Paper Award**).
4. ***Y. Li***, Y. Liu, W. Yuan, and C. Yu, "Simultaneous Measurement of Axial Strain and Temperature Based on Twin-core Single-hole Fiber with Vernier effect," ***Asia Communications and Photonics Conference and Exhibition*** (ACP) 2022, Paper 496, pp. 1-5, Shenzhen, China, November 4 to 8, 2022 (**Tingye Li Best Paper Award**)
5. W. Lyu, S. Chen, Z. Liu, P. Xu, ***Y. Li***, and C. Yu, "Non-invasive Vital Signs Monitoring and Premature Beats Recognition System Based on a Six Holes High Birefringence Fiber," ***28th International Conference on Optical Fiber Sensors*** (OFS-28), Hamamatsu, Japan, November 20 to 24, 2023.
6. W. Lyu, S. Chen, W. Yuan, ***Y. Li***, Q. Wang, and C. Yu, "Non-contact Short-term HRV Analysis of Patients with Premature Beats Based on a Fiber Optic Sensor," ***28th International Conference on Optical Fiber Sensors*** (OFS-28), Hamamatsu, Japan, November 20 to 24, 2023.

7. Y. Li W. Lyu, ***Y. Li*,** Q. Wang, X. Wang. W. Yuan, C. Yu, “A Gas Pressure Sensor Based on Optical Fiber Fabry-Perot Interference,” ***2023 Asia Communications and Photonics Conference/2023 International Photonics and Optoelectronics Meetings (ACP/POEM)***, Wuhan, China, 2023, pp. 1-3, doi: 10.1109/ACP/POEM59049.2023.10369909.
8. W. Lyu, ***Y. Li***, S. Chen, Q. Wang, and C. Yu, “Short Time HRV assessment based on a fiber optic sensor,” ***Conference on Lasers and Electro-Optics-Europe*** (CLEO-Europe) 2023, Munich, Germany, June 26 to 30, 2023.
9. W. Lyu, J. Yu, Q. Wang, S. Chen, C. Yu, and ***Y. Li*,** “Drivers’ Heart Rate Monitoring System Based on Dual Fiber Optic Sensors,” ***Photonics Global Conference 2023***, Stockholm, Sweden, August 21 to 23, 2023.

Content

List of Abbreviations

A	
Amplified spontaneous emission	ASE
Analogous fast Fourier transform	A-FFT
B	
Birefringence fiber	BiF
Ballistocardiograph	BCG
E	
Erbium-doped fiber amplifiers	EDFA
Effective refractive index	ERI
Electrocardiography	ECG
F	
Free spectral range	FSR
Fast Fourier transform	FFT
Fabry-Perot interferometer/interference	FPI
Fiber Bragg grating	FBG
G	
Graded index fiber	GIF
H	
Hybrid Magnetic	EH

Hybrid Electric	HE
Heart rate	HR
Hollow-core fiber	HCF
Hollow core Bragg fiber	HCBF
Helical period fiber grating	HLPFG
I	
Interferometric optical fiber sensor	IOFS
L	
Long-period fiber grating	LPFG
Linearly polarized	LP
M	
Mach-Zehnder interferometer/interference	MZI
Multi-mode fiber	MMF
Multi-core fiber	MCF
Michelson interferometer/interference	MI
N	
Non-core fiber	NCF
Non-polarization maintaining fiber	N-PMF
Non-interferometric optical fiber sensor	NIOFS
O	
Optical path	OP

Optical path difference	OPD
Optical Vernier effect	OVE
Optical spectrum analyzer	OSA

P

Photonic crystal fibers	PCF
Photoplethysmogram	PPG
Polarization maintaining fiber	PMF
Photoelectric detector	PD

R

Respiratory rate	RR

S

Step index fiber	SIF
Sagnac interferometer/interference	SI
Single-core side hole fiber	SCSHF
Six-hole high birefringence fiber	SH-HiBiF
Single-mode fiber	SMF

T

Transverse electromagnetic	TEM
Transverse electric	TE
Transverse magnetic	TM
Twin-core photonic crystal fiber	TCPCF

Twin-core fiber	TCF
Twin-core single-hole fiber	TCSHF
Thermo-Electric Cooler	TEC
Title fiber Bragg grating	TFBG

W

Wavelength division multiplexing	WDM

List of Figures

List of Tables

Chapter 1 Introduction

1.1 Overview and Research Motivations

In recent years, because of the rapid improvement of high-speed communication technology, the world has become an always-connected world. Under this circumstance, information collection by sensors is the first and the most important step. Following this, every field has better performance requirements on sensors to build the internet of everything.

Compared to common electrical sensors, optical sensors have the unique advantage of anti-electromagnetic interference, and higher sensitivity, higher accuracy, faster response speed. Among optical sensors, the sensors based on the fibers draw more attention from the researchers because the fiber sensors are more convenient for building up communication sensing integration systems. In addition, optical fiber sensors' unique characteristics: compact size, high pressure, and temperature resistance, long long-term stability, have also been demonstrated by researchers [1-5]. Because of these unique characteristics, optical fiber sensors have been developed and used in many systems. For example, automatic control, online detection, and fault diagnosis for production systems, leakage detection for petroleum or oil transport systems, vital signs monitoring for medical systems, and health parameters monitoring for large buildings.

Extensive use of optical fiber sensors brings higher performance requirements for researchers. How to enhance the sensor’s sensitivity is always an attention hotspot. Applying the Optical Vernier effect (OVE) on the optical fiber sensors is an elegant method to improve sensitivity [6-8]. Some optical fiber sensors’ complex structures also cannot meet the escalating consumer needs of downstream applications such as fabricating portable devices and wearable devices. Thus, designing new sensor structures is also an important study topic of optical fiber sensors. Normally, a sensor can only respond to only one parameter change. However, in many application fields, it is often necessary to simultaneously measure multiple variables for more comprehensive evaluation [9]. So, the realization of multi-functionality is also a promising research direction for optical fiber sensor technology [10].

In this thesis, four different interferometric sensors based on the micro-structure fiber are proposed and demonstrated with better performance than existing sensors. To help get a clear view of optical fiber sensors, the following sub-chapter first introduces the fundamental knowledge of optical fibers.

1.2 Optical Fibers

As a new transmitting medium, optical fiber can transmit light signals over long distances with quite low loss. The birth time of optical fiber traces back several centuries. The concept of light transmitting along a stream of water was proposed as early as the 1790s. John Tyndall demonstrated the phenomenon of light being transmitted through bent water pipes around the 1840s. In the 1880s, Alexander Graham Bell put forward an interesting idea of using the light as a carrier to transmit sound information. However, the technology at that time could not support the realization of this idea. Then, the 1930s saw some advancements in the use of glass rods and tube waveguides for optical transmission. After about 30 years, researchers at Corning Glass Works, Robert Maurer, Donald Keck, and Peter Schultz, fabricated the first low-loss fibers based on a design of glass core and cladding. This breakthrough establishes the foundation for modern fiber optics and enables practical applications. In the 1970s, researchers put their efforts into developing single-mode fiber (SMF), which just allows one mode to propagate at specific wavelengths.

After the 1980s, erbium-doped fiber amplifiers (EDFA) and wavelength division multiplexing (WDM) were invented, enabling efficient amplification of optical signals for longer distance transmission and higher information transmission capacities. By then, the fundamental technologies of optical fiber were ripe for information transmission.

Following this, optical fiber technology's development moves into the direction of high-speed data transmission over long distances, higher bandwidth capabilities, and security, revolutionizing global communication. Ongoing research works continue to seek even faster and more efficient data transmission, expanding outward the boundaries of the optical fiber [11-12].

1.2.1 Optical Fiber Structure

The typical structure of the optical fiber is shown in Fig. 1.1(a), which has three parts: core, cladding, and outer coating, which are concentric with each other in general. However, the core may be off-center depending on the actual application.

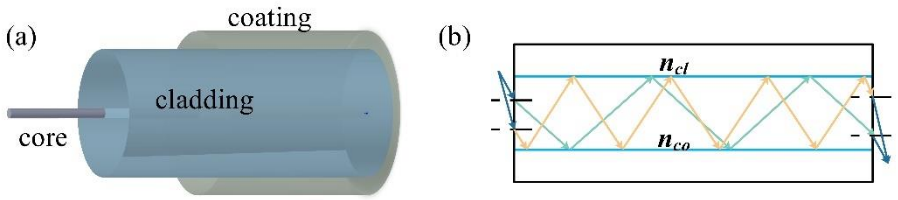

Fig. 1.1 (a) The common structure diagram of the optical fiber; (b) the light beams transmitted in the optical fiber at different injection angles.

The core part is where light signal is transmitted, typically made of glass or plastic with the dopant. The diameter of the core varies from ~8 μm (SMF) to ~52.5 μm (multi-mode fiber, MMF). The core effective refractive index (ERI) n_{co} is determined by the materials used and dosage concentration. Usually, the cladding material is the same as the core but with different doping rates. Usually, the ERI of the cladding n_{cl} is 1% lower than n_{co}. The appropriate ERI difference and light incidence angle can make sure light propagates inside the core without leakage because of the total reflection effect, as shown in Fig. 1.1(b).

The outer coating layer serves as a protective layer surrounding the cladding, usually made of polymer material. It can provide mechanical reinforcement to protect the fiber from external damage and moisture. Because the coating layer will be melted during the high-temperature splicing process, the coating must be stripped to expose only the cladding before fiber fusion splicing

1.2.2 Fiber Modes

Generally speaking, the theory of ray optics and the theory of wave optics are the commonly used two methods to analyze the transmission state of light in fiber[13]. If fiber radius $\boldsymbol{r}$ is much larger than the incidence light wavelength $\boldsymbol{\lambda}$, the light can be approximately replaced by multi-rays. Then, using the geometrical optics model can easily study the propagation path of light rays. However, there are huge errors if the $\boldsymbol{\lambda}$ is close to $\boldsymbol{r}$. Based on this problem, the theory of wave optics is introduced to analyze the fiber transmission characteristics at a micro level. In the theory of wave optics, the stable propagation states in fiber are defined as “Modes”. The finite discrete number of paths down the optical fiber in optical ray theory is equal to the fiber mode number in optical wave theory. For specific optical fiber structures, the actual propagation mode number is only related to the fiber self-parameter, including light wavelength, diameter, core, and cladding ERI.

The mathematical expression of the fiber modes can be derived from the basic electromagnetic field equations, referred to as Maxwell’s equations.

$$\begin{cases} \nabla \times H = \dfrac{\partial D}{\partial t} \\ \nabla \times E = -\dfrac{\partial B}{\partial t} + J \\ \nabla \bullet D = \rho \\ \nabla \bullet B = 0 \end{cases} \tag{1.1}$$

E is the electric field intensity, ***D*** is the displacement vector, ***H*** is the magnetic field intensity, and ***B*** is the magnetic induction intensity. The relationship between them can be expressed as ***D***=***εE***, ***B***=***μH***, where ***ε*** is the dielectric constant, and ***μ*** is magnetic conductivity. ***J*** is the conduction current density, and ***ρ*** is the free electricity density. Because the optical fiber is an electrically insulated and homogeneous medium, there is no conduction current and free electricity. In that case, ***J***=0, ***ρ***=0.

Then Eq. (1.1) can be transformed into the following equations, which are the description of the ***H*** and ***E***.

$$\begin{cases} \nabla^2 E + \nabla\left(E \bullet \dfrac{\nabla \varepsilon}{\varepsilon} \right) = \varepsilon\mu \dfrac{\partial^2 E}{\partial t^2} \\ \nabla^2 H + \left(\dfrac{\nabla \varepsilon}{\varepsilon} \right) \times (\nabla \times H) = \varepsilon\mu \dfrac{\partial^2 H}{\partial t^2} \end{cases} \tag{1.2}$$

For uniform fiber structure, ***ε*** and ***μ*** can be regarded as constant. Then, the above equation can be transformed as:

$$\begin{cases} \nabla^2 E = \varepsilon\mu \dfrac{\partial^2 E}{\partial t^2} \\ \nabla^2 H = \varepsilon\mu \dfrac{\partial^2 H}{\partial t^2} \end{cases} \tag{1.3}$$

The above equations are named as Helmholtz equations. If the boundary conditions of a fiber are given, the solutions of the corresponding Helmholtz equations can be easily calculated. Each solution corresponds to one propagation fiber mode.

The modes within a fiber exhibit diverse characteristics: (1) Transverse electromagnetic mode (TEM): With perpendicular electric and magnetic fields, the electromagnetic wave's propagation occurs perpendicular to the field plane. (2) Transverse electric mode (TE): Characterized by the absence of an electric field component along wave propagation direction, while retaining a magnetic field component. (3) Transverse magnetic mode (TM): This mode lacks a magnetic field component along the wave propagation direction but includes an electric field component. (4) Hybrid electric mode (HE): Dominated by the electric field component in the propagation direction. (5) Hybrid magnetic mode (EH): With the magnetic field component dominating wave propagation direction. (6) Additional hybrid modes exist, including mixed-mode, high-order hybrid modes, hybrid plasmonic modes, and tunneling hybrid modes.

Except for photonic crystal fibers (PCF), conventional optical fibers typically feature a radially symmetric ERI profile and a relatively minor contrast in ERI between the core and cladding. In that case, some exact modes can be merged into one linearly polarized (LP) mode, which is mathematically simpler to describe. The Table of comparison for some low-order exact modes and LP modes is as follows.

Table I The mapping table between the LP mode and actual modes

LP mode	Exact modes
LP_{01}	HE_{11}
LP_{11}	HE_{21}, TE_{01}, TM_{01}
LP_{02}, LP_{21}	HE_{12}, EH11, HE31
LP31	HE41, EH21
LP12	HE22, TE02, TM02
LP03, LP22	HE13, HE32, EH12
LP13	HE23, TE03, TM03

The subscripts are the order of the modes. The lowest order mode is the LP_{01} mode, of which the transverse intensity profile is similar to the Gauss beam. For SMF, it can only transmit LP_{01} mode in the core. At the same time, numerous cladding modes are present, resulting in significant propagation losses at the outer cladding interface. By optical couple methods, the core mode and cladding modes can interfere with each other, constructing fiber version Mach-Zehnder interferometers (MZIs) [14].

1.2.3 Classification of Fiber

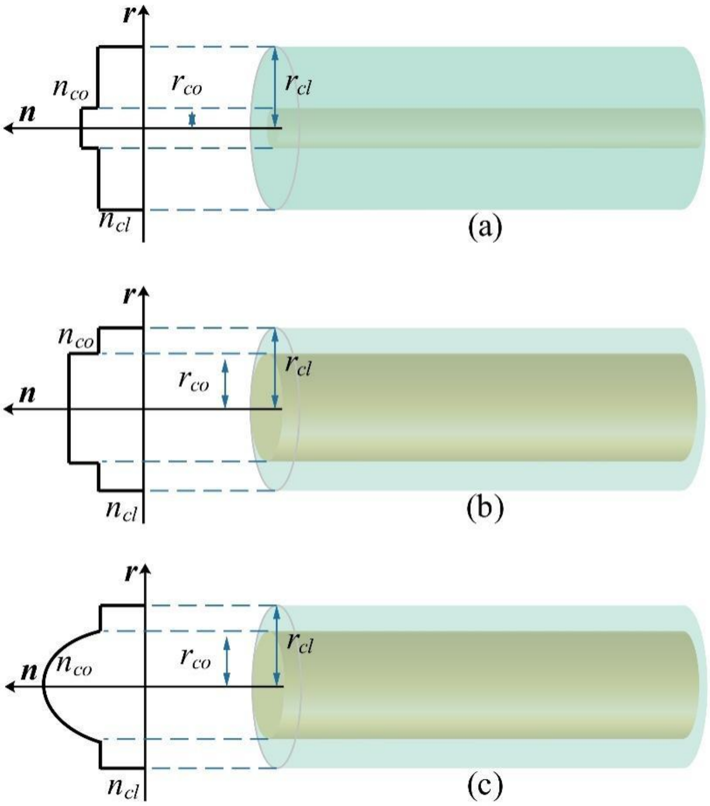

Fig. 1.2 (a) The ERI profile and structure of the SMF, (b) The ERI profile and structure of the SIF-MMF, (c) The ERI profile and structure of the GIF-MMF.

Various standards exist for optical fibers classification. For instance, based on the transmitted light's polarization state, single-mode fiber (SMF) has two types: non-polarization-maintaining fiber (N-PMF) and polarization-maintaining fiber (PMF). PMF includes three distinct types: single-polarized fiber, birefringence fiber (BiF), and circular BiF. Single-polarization optical fibers transmit only one polarization mode, while high birefringent fibers transmit two orthogonal polarization modes with a significant propagation speed difference, and low BiF, with nearly equal propagation speeds. Circular BiFs transmit circularly polarized light.

According to the fiber core ERI profile, the fiber can be categorized into step index fiber (SIF) and graded index fiber (GIF). As shown in Fig. 1.2 (a) and (b), the ERI profile of SIF is homogeneous in the core but mutates at the core and cladding boundary. The ERI profile of GIF changes with the radius in a certain functional relationship as shown in Fig. 1.2 (c).

Characterized by low optical transmission loss, high-purity fused quartz become the commonly used raw material for optical fiber fabrication. The transmission loss at some wavelengths can be low to 0.2dB/km, generally less than 1dB/km. The low-cost polymer can also be used for fabricating optical fiber. However, the disadvantage is that the material loss is large, and temperature performance is poor. In some special needs, the fiber core can be liquid or single crystal.

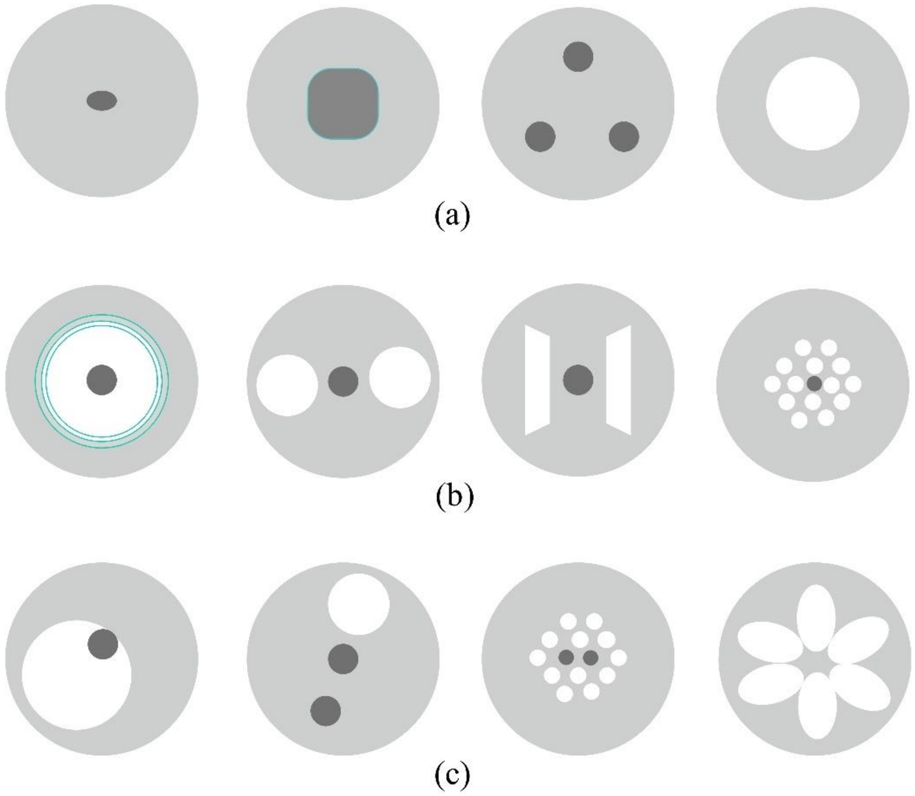

Fig. 1.3 The cross-section of fibers: (a) with special core structure, (b) with special cladding structure, (c) with special core and cladding structure.

Due to the development of fiber drawing technology, fibers with special microstructures are drawn out. As shown in Fig. 1.3, the fibers can be divided into three categories according to the different special parts. First, fibers with special core structures, such as multi-core fiber (MCF), elliptical core fiber, non-core fiber (NCF), hollow core fiber (HCF), square-core fiber, and so on. Secondly, fibers with special cladding structures, such as single-core multi-hole fiber, multi-cladding fiber, and fiber with a stressed zone in the cladding. Finally, fibers with special core and cladding structures, such as suspended core fiber, core-hole composite structure fiber, and multi-core and multi-hole fiber. All the above fibers can be collectively referred to as micro-structure fibers [15].

1.3 Optical Fiber Sensors

The evolution of optical fiber transmission and drawing technology also enabled the development of fiber sensing technology. Lower attenuation of fiber enables transmitting over long distances between sensing points and performing multiplexed measurements. The characteristics of resistance to electromagnetic interference enable fiber sensors superior to electrical sensors in the electromagnetic environment [16]. Microstructure fibers make it possible to fabricate abnormal sensor structures to meet specific measurement requirements [17]. Optical fiber sensors also have the requirement to withstand high temperatures [18]. Because of these unique characteristics, optical fiber sensors become irreplaceable elements in sensing systems of different areas. The following subsection covers the fundamental information about optical fiber sensors, including the working principles, classification, and advantages.

1.3.1 Working Principles

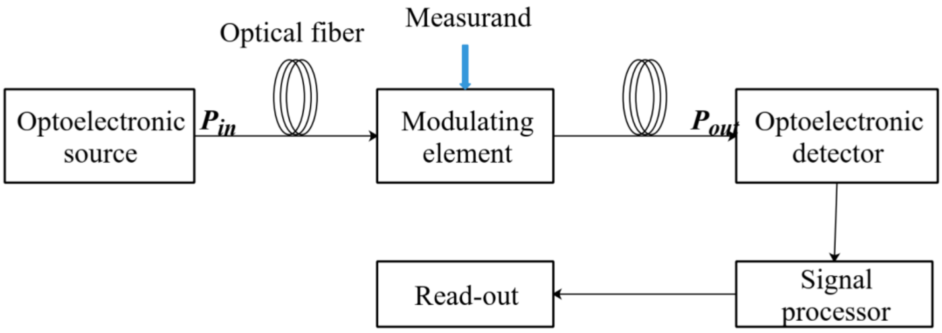

Fig. 1.4 Generic block diagram of optical fiber sensor.

As depicted in Fig. 1.4, an optical fiber sensor consists of an optoelectronic source, a section of transmitting optical fiber, a photodetector, and a signal-processing unit. Initially, the emitted light is directed into the sensing head or modulator. Interaction between the measured parameters and the input light modifies the optical characteristics of the output light, resulting in modulated signal light with variations in wavelength, intensity, frequency, phase, or polarization state. Following this, the photodetector transforms the optical signal into an electrical signal, which is then analyzed to extract the measured physical quantity [19-23].

1.3.2 Classification of Optical Fiber Sensors

According to whether light interference occurs within the sensor structures, optical fiber sensors are categorized into interferometric optical fiber sensors (IOFS) and non-interferometric optical fiber sensors (NIOFS).

NIOFS, also known as amplitude-type fiber sensors, operate by detecting light intensity changes within the fiber. Common mechanisms for inducing light intensity changes include altering the fiber’s bending status, modifying its coupling conditions, and adjusting its light absorption characteristics.

Optical fiber micro-bending sensors, for instance, exploit micro-bending loss between the fiber core and cladding to measure environmental pressure, micro-displacement, and micro-vibration. For the sensor structure in Fig. 1.5 (a), a section of MMF is put in a deformer which can transfer environmental parameters fluctuation to fiber bending state changes. Then, once the photoelectric detector (PD) detects the light intensity variation, the data processing module will give an alarm signal. For this type of fiber sensor, the sensitivity can reach as high as 6 μV/A, which equals to the level of the minimum detectable micro-displace is 0.01 nm. However, the service life of this type of sensor is not long because the fiber is too fragile to be bent too many times. Optical fiber couple sensors utilize the couple conditions change between the sensing fiber and other optical elements to detect surrounding parameters fluctuation.

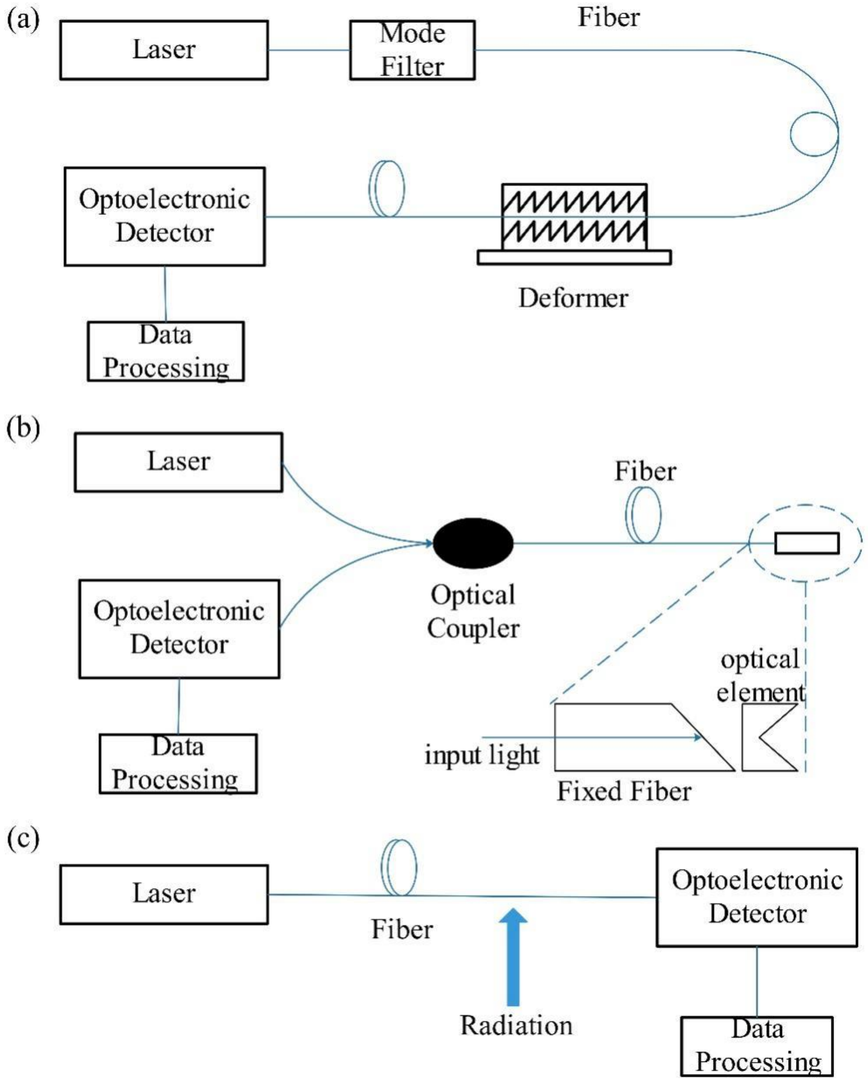

Fig. 1.5 Generic block diagram of NIOFS: (a) micro-bending sensors, (b) couple sensors, (c) absorption sensors.

For the couple sensor structure shown in Fig. 1.5 (b), if the fiber is close to other optical elements, the most output light from the sensing fiber can be coupled to other optical elements or back coupled to the sensing fiber. Once the distance or the medium ERI between optical elements changes, the output light intensity will change accordingly. Using alike structures, many optical gas pressure, concentration, temperature, and micro-displacement sensors have been proposed and demonstrated. However, the biggest problem for optical fiber couple sensors is that the fiber needs to be fixed by precision machines, which sharply increases the use cost.

As shown in Fig. 1.5 (c), optical fiber absorption sensors utilize the absorption loss increasing caused by the X-ray, γ-ray, or other radiation to detect radiation change in the nuclear power station or radioactive storage position. Because the main sensing part of this type of sensor is pure fiber, the sensitivity is related to the fiber length. That is, using longer fiber can increase sensitivity.

IOFS, also called phased-type fiber sensors, work based on light phase change introduced by optical interference [24]. The main characteristics of this type of sensor have four aspects [25]. Firstly, interferometric fiber sensors have ultra-high sensitivity. Sensing based on optical interferometry has become the most sensitive detection technique now because the reference path can help increase the sensitivity sharply. Secondly, interferometric fiber sensors have flexible and diverse construction. Because the fiber itself serves as a sensing part, the sensor structure can be customized according to different usage scenarios. Thirdly, interferometric fiber sensors have much wider effective working objects. Many kinds of parameters can be detected if the parameters influence the optical path of the interferometers. Commonly, one single interferometer can measure two or more different parameters at the same time. Finally, interferometric fiber sensors usually have a special demand for fiber used. In the common fiber interferometers, to obtain light interference from the same fiber modes, the SMF is a better choice rather than MMF. Although using MMF can also get interference fringe, it is difficult for the next data processing part to get accurate information. In addition, some studies have demonstrated that the fiber-coating materials can influence the sensor sensitivity. Through enhancing sensitivity to the parameters to be measured and desensitizing irrelevant parameters by conducting special treatment on fiber. this problem can be solved perfectly.

According to the traditional principles of optical wave interference, there are four commonly used interference fiber optic sensors: Michelson interferometric (MI) fiber optic sensor, MZI fiber optic sensor, Sagnac interferometric (SI) fiber optic sensors, Fabry-Perot interferometric (FPI). The detailed working principles of them are introduced in Chapter 2.2.

1.3.3 Advantages of Optical Fiber Sensors

Compared to traditional electronic sensing technology, optical fiber sensing technology offers numerous advantages:

(1) Immunity to electromagnetic interference and corrosion resistance: Optical fiber sensors transmit information via light waves through electrically insulated and corrosion-resistant mediums. This feature ensures reliability in harsh environments, including those with strong electromagnetic interference or flammable and explosive conditions, making them suitable for applications in electromechanical, petrochemical, and mining industries.

(2) High sensitivity: Utilizing light as an electromagnetic wave with a short wavelength enables precise measurements of optical length. For instance, fiber optic interferometers can detect minute changes in the optical path length due to small mechanical forces or temperature fluctuations.

(3) Rapid measurement speed: Light travels swiftly and can convey two-dimensional information, facilitating high-speed

measurements. Tasks such as radar signal analysis, which demand rapid detection rates, can be effectively addressed through high-speed spectrum analysis leveraging light's diffraction phenomenon, a challenge for electronic methods.

(4) Large information capacity: Utilizing light waves as carriers enables the transmission of signals with high frequencies and accommodating wide frequency bands. Moreover, a single optical fiber can transmit multiple signals simultaneously, enhancing information capacity.

(5) Adaptability to harsh environments: Optical fibers possess characteristics of high temperature, wet, chemical, and pressure resistance. Consequently, they can function effectively in environments unsuitable for other sensor types.

1.4 Research Objectives

The research objectives of works in this thesis mainly focus on developing novel sensor configurations with enhanced performance for fiber sensing systems used in different fields. More specifically, the thesis proposed four different interferometric configurations based on microstructure fiber, and their feasibility is demonstrated by experiments.

- Develop a SI sensor for non-contact human respiratory and heart rate monitoring using six-hole high birefringence fiber (SH-HiBiF).
- Demonstrate an axial strain sensor based on inline Mach-Zehnder interference OVE utilizing Twin-core and Single-hole fiber (TCSHF).
- Investigate an inline dual FPI gas pressure sensor utilizing Single-core Side-hole Fiber (SCSHF) with OVE.
- Design a parallel connection of dual MIs for lateral stress sensing based on PMF with OVE.

1.5 Organization of the Thesis

This thesis is composed of 7 chapters.

Chapter 1 gives an overview of the research background and motivations. The fundamental knowledge of optical fiber and optical fiber sensors is then introduced. Finally, the research objectives and the thesis outline are given,

Chapter 2 firstly introduces the methods to motivate optical wave interference, including the wave-front splitting method and amplitude splitting method. Next, the common structures of different optical fiber interferometers are presented in detail.

Furthermore, the concept of OVE is introduced to help enhance the sensor's sensitivity. Finally, various optical fiber sensor structures based on the OVE are summarized in this chapter.

Chapters 3 to 6 proposed four different interferometric sensors based on microstructure fiber for different sensing usage including vital signs monitoring, axial strain, lateral stress, and gas pressure measurement. The fabrication process and parameters are given in detail after countless experimental attempts. Then, the final spectrum of the four sensors is analyzed mathematically. Finally, the experiment details and results are given to verify the proposed sensor's serviceability.

In the end, chapter 7 summarizes all the works in this thesis and discusses possible future research directions.

Chapter 2 Optical Interference and Vernier Effect

In physics, wave superposition refers to the phenomenon that two or more waves of the same type are incident in the same space. The resultant wave may have greater or lower amplitudes, depending on the vector sum of every wave’s oscillating regime. That is, every wave’s is oscillating regime contributes individually to the final amplitude without influenced by other existing waves. The wave superposition principles are applied uniformly across all types of waves [26], for example, mechanical waves, water waves, gravity waves, electrical waves as well as electromagnetic waves. As one type of electromagnetic wave, optical waves can also produce superposition effects.

Generally speaking, the possible superposition results of optical waves with different frequencies are quite complicated. In this work, only superposition phenomena of optical waves with the same or similar frequency are discussed. The superposition of two or more optical waves with the same vibration frequency, vibration direction, propagating direction and also fixed phase difference will introduce an optical interference effect. If the propagating direction of the just two waves is opposite, there will be a standing wave effect after superposition. The superposition of two or more waves with similar frequency and same vibration direction and propagating direction will motivate OVE.

2.1 Principles of Optical Wave Interference

For the two optical waves' characteristics to be highly consistent to motivate the interference effect, they must be derived from the same origin, and they arrive at the same point by different paths. Commonly used methods now to analyze the resultant wave's characteristics are the amplitude-splitting method and the wavefront-splitting method.

2.1.1 Wavefront-splitting interference

The frequency of the light wave used for communication is usually around 10^{14} Hz [27], which is too high for the detectors now to detect the electric field fluctuation. Thus, observing the interference intensity pattern is a better choice for studying optical wave interference. The light interference pattern was first observed and described by Thomas Young in 1801. His double-slit experiment is based on the wavefront-splitting method, which has a far-reaching influence on the optics field.

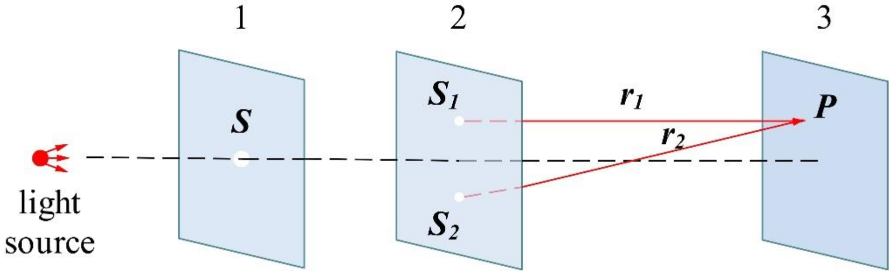

Fig. 2.1 Young’s double-slit interference experiment.

In Fig. 2.1, ***S*** is a little hole illuminated by the light source. $\boldsymbol{S_1}$ and $\boldsymbol{S_2}$ are two little holes on the second screen, which are distributed symmetrically on both sides of the axis. This set can split the combined wavefront from ***S*** into two sub-wavefronts without phase difference. Then, $\boldsymbol{S_1}$ and $\boldsymbol{S_2}$ can be regarded as the same single-wavelength light source. That is the frequency and the vibration direction of optical waves emitted from $\boldsymbol{S_1}$ and $\boldsymbol{S_2}$ are the same as each other. Then the light amplitude of arbitrary point ***P*** in the region where two optical waves meet can be expressed as:

$$\begin{aligned} \vec{E}_1 &= a_1 \cos\left[2\pi\left(\frac{t}{T}-\frac{r_1}{\lambda}\right)\right] \\ \vec{E}_2 &= a_2 \cos\left[2\pi\left(\frac{t}{T}-\frac{r_2}{\lambda}\right)\right] \end{aligned} \tag{2.1}$$

The $\boldsymbol{r_1}$ and $\boldsymbol{r_2}$ are the distances between the specific point ***P*** and two light sources. The $\boldsymbol{a_1}$ and $\boldsymbol{a_2}$ are the vibration amplitude of the two waves. According to the superposition principle, the amplitude of ***P*** is the vector sum of two participating waves’ amplitude, which is

$$\vec{E} = \vec{E}_1 + \vec{E}_2 = a_1 \cos\left[2\pi\left(\frac{t}{T} - \frac{r_1}{\lambda}\right)\right] + a_2 \cos\left[2\pi\left(\frac{t}{T} - \frac{r_2}{\lambda}\right)\right] \quad (2.2)$$

$$\begin{aligned}\vec{E} &= a_1 \cos(\omega t + \alpha_1) + a_2 \cos(\omega t + \alpha_2) \\ &= (a_1 \cos\alpha_1 + a_2 \cos\alpha_2)\cos\omega t - (a_1 \sin\alpha_1 + a_2 \sin\alpha_2)\sin\omega t\end{aligned} \quad (2.3)$$

Because $\boldsymbol{a_1}$, $\boldsymbol{a_2}$, $\boldsymbol{\alpha_1}$, and $\boldsymbol{\alpha_2}$ are constants, the Eq. (2.3) can be simplified as:

$$\begin{aligned}\vec{E} &= A\cos\alpha\cos\omega t - A\sin\alpha\sin\omega t \\ &= A\cos(\omega t + \alpha)\end{aligned} \quad (2.4)$$

Then, $\boldsymbol{A}$ and $\boldsymbol{\alpha}$ can be calculated as:

$$\begin{cases} A^2 = a_1^2 + a_2^2 + 2a_1 a_2 \cos(\alpha_1 - \alpha_2) \\ \tan\alpha = \dfrac{a_1 \sin\alpha_1 + a_2 \sin\alpha_2}{a_1 \cos\alpha_1 + a_2 \cos\alpha_2} \end{cases} \quad (2.5)$$

The vibration status of $\boldsymbol{P}$ is also conforming to simple harmonic vibration. The vibration frequency of $\boldsymbol{P}$ is the same as the light source’s frequency. The amplitude $\boldsymbol{A}$ and the original phase are decided by the two participating optical waves’ amplitude and phase.

The light intensity at a specific point is the square of the average wave amplitude.

$$\begin{aligned}I &= |E|^2 = A^2 = a_1^2 + a_2^2 + 2a_1 a_2 \cos(\alpha_1 - \alpha_2) \\ &= I_1 + I_2 + 2\sqrt{I_1 I_2}\cos\delta\end{aligned} \quad (2.6)$$

$\boldsymbol{I_1 = a_1^2}$, and $\boldsymbol{I_2 = a_2^2}$ are the light intensity of the two participating optical waves. From Eq. (2.6), the light intensity is decided by the phase difference between the two participating waves. Because the original phase of the two waves is the same in this experiment, the phase difference at the ***P*** point between the two waves is introduced by the wave propagation distance difference as:

$$\delta = \frac{2\pi}{\lambda}\left(r_2 - r_1\right) = \frac{2\pi}{\lambda_0} n\left(r_2 - r_1\right) \tag{2.7}$$

Here, the concept of Optical Path (OP) is introduced, which is the product of the optical propagation physical distance in the medium and the medium's ***ERI***. Then, the physical distance of the optical wave propagating in any medium can be converted into the propagating distance in a vacuum, which is convenient for comparison.

The Optical Path difference (OPD) is different at different points in the superposition area of optical waves as Eq. (2.7) shows. Thus, there are stable strong and weak intensity distributions in the superposition area, which is referred to as interference fringe. The light source that can be used for motivating interference effect is called a coherent source.

Except for the double-slit experiment, the Fresnel prism experiment, Lloyd mirror experiment, and Billet lens experiment are all conducted based on the wavefront-splitting method to observe the interference effect.

2.1.2 Amplitude-splitting interference

In the amplitude-splitting method, the light wave from a single-point light source is divided into two parts: reflection and transmission by a beam splitter. The two parts of optical waves travel along different paths and then are superimposed to produce the interference pattern. Commonly used beam splitters are thin film and light-splitting mirrors. Here, a thin film as an example to validate the amplitude-splitting method as shown in Fig. 2.2.

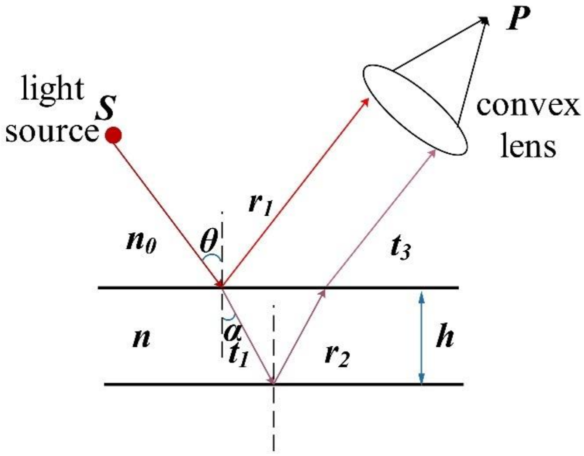

Fig. 2.2 The amplitude-splitting interference experiment.

The light from the light source incidents the upper surface of the film at an angle of θ. The part of reflected light is the first participating light. The transmission light from the upper surface propagates to the lower surface, then is reflected to the upper surface, and finally back to the same direction as the first participating light. Because two lights are in parallel, a convex lens is used to collect the two lights together at the same point ***P***.

To simplify the calculation, the plural expression of optical waves is led into. The original amplitude and phase of the light arriving at the upper surface are $\boldsymbol{E_0}$ and ***0***, respectively. The amplitude reflection and transmission index at the upper surface are $\boldsymbol{r_1}$ and $\boldsymbol{t_1}$, respectively. Then, the amplitude of the two lights at ***P*** can be expressed as:

$$\begin{aligned} E_1 &= r_1 E_0 \exp[-i(\omega t + \frac{2\pi n_0 l_1}{\lambda})] = aE_0 \exp[-i(\omega t + \alpha_1)] \\ E_2 &= t_1 r_2 t_3 E_0 \exp[-i(\omega t + \frac{2\pi n_0}{\lambda}(\frac{2h}{\cos\theta_n} + l_2))] = bE_0 \exp[-i(\omega t + \alpha_2)] \end{aligned} \quad (2.8)$$

To simplify the calculation, the constant terms of amplitude are replaced by ***a*** and ***b***, the phase terms are replaced by $\boldsymbol{\alpha_1}$ and $\boldsymbol{\alpha_2}$. According to wave superposition principles, the electric field intensity after superposition can be expressed as:

$$E = aE_0 \exp[-i(\omega t + \alpha_1)] + bE_0 \exp[-i(\omega t + \alpha_2)] \quad (2.9)$$

Then, the output light intensity can be described as:

$$\begin{aligned} I &= |E|^2 = E_0[a^2 + b^2 + 2ab\cos(\alpha_1 - \alpha_2)] \\ &= I_1 + I_2 + 2\sqrt{I_1 I_2}\cos(\alpha_1 - \alpha_2) \end{aligned} \quad (2.10)$$

Thus, for any point in the amplitude-splitting interference output area, the final light intensity is also determined by the phase difference between the two lights.

The definition of thin film for amplitude-splitting interference is broad, any structures with two optical surfaces and a light conductive medium can be regarded as thin film. For example, parallel plate, optical prism, and so on. Several interferometers based on the amplitude-splitting method in free space are designed and used for sensing work: SI, MZI, FPI, and MI. The common structure of the four interferometers is shown in Fig. 2.3.

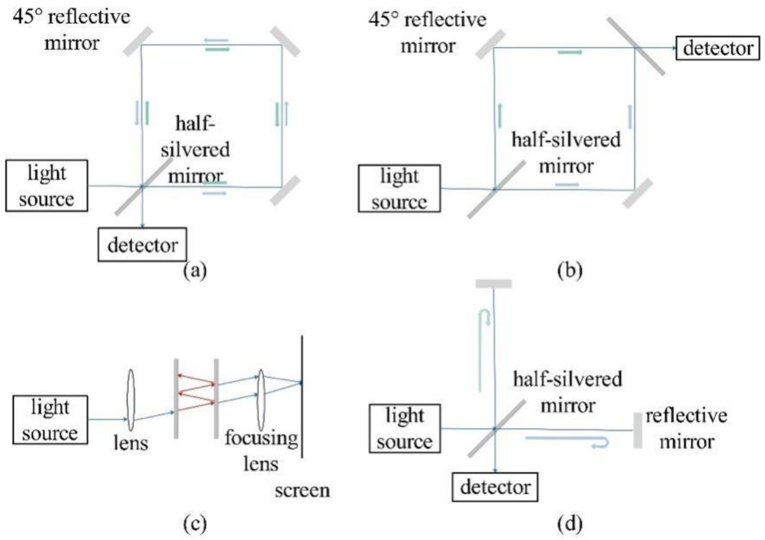

Fig. 2.3 (a) to (d) SI, MZI, FPI, and MI structures build-up by lens and mirrors in free space.

2.2 Optical Fiber Interferometer

The size of optical interferometers building up based on the lens and mirrors in free space is not fitting for the miniaturization of the sensing systems. Considering that optical fiber is a quite lightweight optical waveguide, researchers designed and demonstrated many different optical fiber interferometer structures.

Due to the mechanism of the wavefront splitting method being too complicated to be constructed using the optical fiber, the following part only introduces four commonly used optical fiber interferometers based on the amplitude-splitting method.

2.2.1 Sagnac Interferometer

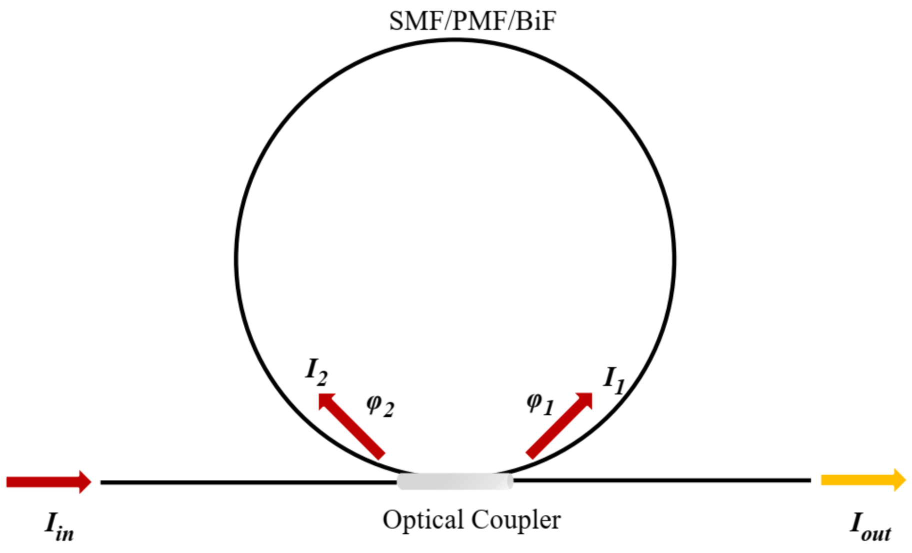

Fig. 2.4 The structure diagram of optical fiber SI.

Over 45 years ago, the optical fiber version of SI was first reported. Like any SIs based on the mirrors, the fiber version also has a loop based on SMF as shown in Fig. 2.4. Usually, there is a section of PMF or BiF in the fiber loop to extend the optical delay and enhance sensitivity. Injected into the fiber loop from one port of the optical coupler, the input light will be divided into two parts propagating along opposite direction in the fiber loop. During the propagation process, the two parts of light have phase differences under the action of external forces because of the superposition of the birefringence effect and the Sagnac effect. Then, they will interfere with each other when they meet again at the optical coupler.

If the incident light intensity of the two lights is I_1 and I_2, the wavelength is λ, the ERI are n_1 and n_2, and the fiber loop length is L, Then, the output interference light intensity can be calculated as:

$$I = I_1 + I_2 + 2\sqrt{I_1 I_2}\cos\left[\frac{2\pi}{\lambda}\left(n_1 L_1 - n_2 L_2\right)\right] \tag{2.11}$$

The final position of the interference fringes is determined by the fiber loop length and the ERI difference. For the parameters that can change the length or the ERI of the fiber loop, the SI can detect directly by demodulating the interference fringe change. The SIs have found numerous applications: fiber loop mirrors, optical fiber Sagnac current sensors, hydrophones, and geophones, not mention to strain and lateral stress sensing.

2.2.2 Mach Zehnder Interferometer

For optical fiber MZI, there are two structures: dual-arm type and inline type. As shown in Fig. 2.5 (a), two optical fiber couplers are necessary to build up a dual-arm type MZI structure. The first optical coupler divides the injected light into two arms with the same original phase. The two arms are typically named the sensing arm and the reference arm. There is a physical length mismatch between the two arms introduced by length difference or other disturbances that can cause fiber length change, introducing a phase difference between arms. Then, the interference effect can be observed after outputting from the second optical coupler.

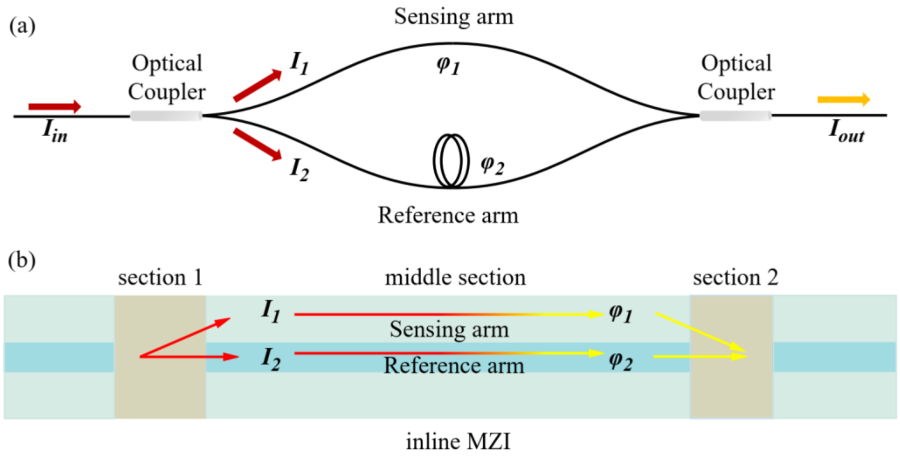

Fig. 2.5 The structure diagram: (a) the traditional dual-arm fiber MZI, (b) the inline fiber MZI.

For inline MZ structures, light input, division, interference, and output are all occurring in the same fiber. The common structure is based on the Sandwich structure as shown in Fig. 2.5 (b). The function of sections 1 and 2 is the same as the optical coupler. The first component can enlarge the filed distribution and then couple the light into different regions of the middle component. The middle component usually is a section of SMF because it can provide at least two different transmission paths with different ERI: core and cladding region. Thus, the two arms are all in the same fiber. Although the length of the arms is entirely the same, the ERI difference introduces a phase difference. Finally, collected by the third component, the light in the core and cladding interferes with each other and then the interference fringe can be observed.

The inline MZI structure is more compact than the traditional MZI structure. The study about inline MZI now mainly focuses on designing structures of components 1 and 2. Up to now, MMF, FMF, NCF, FBG, LPG, HLPG, spherical structure, taper structure, twist structure, peanut type, and so on have been used to build up inline MZI. If the structure of components 1 and 2 are the same, this type of MZI is named a symmetrical MZI. If components 1 and 2 are different, this type of MZI is named unsymmetrical MZI.

If the light intensity in the two arms is I_1 and I_2, respectively. The lengths of the two arms are L_1 and L_2. The wavelength is λ, and the ERI of the two arms are n_1 and n_2. Then, the output interference spectrum can be expressed as:

$$I = I_1 + I_2 + 2\sqrt{I_1 I_2}\cos\left[\frac{2\pi}{\lambda}\left(n_1 L_1 - n_2 L_2\right)\right] \qquad (2.12)$$

The MZIs have been widely used in physical parameters measurement systems, including twist, strain, temperature, and joint measurement systems. In addition, combined with other materials, the MZIs can also be used in the chemical and biological fields.

2.2.3 Fabry-Perot Interferometer

Developing from the optical FPI in free space, the fiber version of FPI also has a cavity between two reflectors. The reflectors can be fiber end, optical film, or other things that can reflect the light. Three types of fiber FPI structures have been demonstrated now: intrinsic FPI, extrinsic FPI, and composite FPI as shown in Fig. 2.6.

The original research on FPI focused on intrinsic FPI, the main characteristic of which is that the cavity is built up by the optical fiber itself. In Fig. 2.6(a), a part of SMF is divided into A, B, and

C three sections. After coating with high reflective films at the end of A and B, three sections are fusion spliced together to build an intrinsic FPI. Section B serves as the FPI’s cavity. Usually, the cavity length of this type of FPI is at the level of several micrometers, offering challenges for fabrication. The high reflective films are later replaced by fiber grating, eliminating the cleave and fusion splicing process. However, because the cavity is fiber, the length and ERI of the fiber are all easily influenced by the surrounding environment, resulting in the output spectrum signal being a dual-parameter function. How to demodulate the actual cavity length change value becomes an urgent problem to be solved for actual applications.

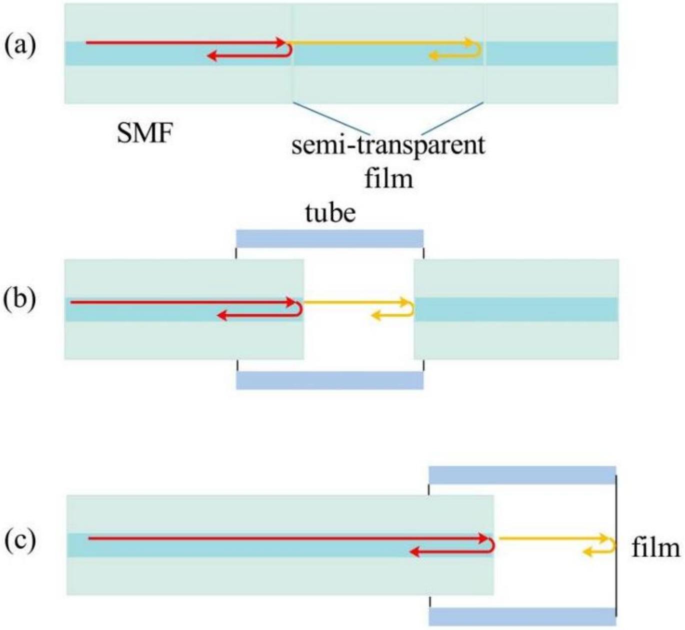

Fig. 2.6 (a) Intrinsic FPI, (b) Extrinsic FPI, (c) composite FPI.

The extrinsic FPI is the most popularly used in many fields now. As shown in Fig. 2.6 (b), two sections of SMF with a coating end are sealed co-axially in a tube to build up a classical extrinsic FPI. An air cavity appears between the fiber ends. The cavity can also be filled with other types of gas or liquid for sensing applications. If the thermal expansivity of the tube material and fiber are entirely the same, the heat elongation value of the tube can offset the heat elongation value of the fiber, resulting in no length change of the cavity. Thus, there is no need to consider the temperature cross-sensitivity problem when using the extrinsic FPI.

For composite FPI structure, only one reflected mirror is the end of a section of fiber, the other mirror can be any reflective surface such as film, flat metal surface, and so on. As shown in Fig. 2.6(c), composite FPI based on the film can be used for acoustic wave detection because the film's forced vibration can periodically change the cavity length. Composite FPI based on the metal and beam structure can be used for earthquake measurement.

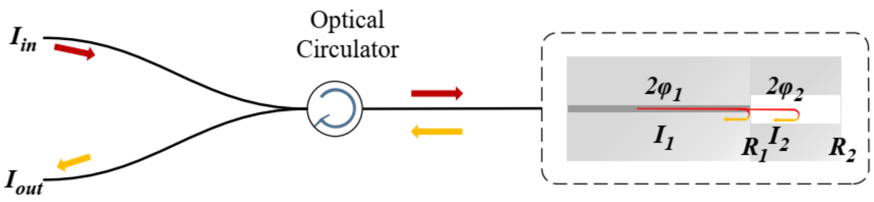

Fig. 2.7 The common sensing system based on FPI.

For either type of FPI, to obtain the reflected light, an optical circulator is necessary as shown in Fig. 2.7. the incident light intensity is I_0, the reflectivity of the first and second surfaces is R_1 and R_2, the cavity length is L, the wavelength is λ, and the ERI of the cavity medium is n. Then, the calculation equation of the output spectrum is:

$$I = I_0 R_1 + I_0 (1 - R_1) + 2I_0 \sqrt{R_1 (1 - R_1)} \cos \frac{4\pi n L}{\lambda} \qquad (2.13)$$

From the above equation, the output light intensity is determined by the L and n. Thus, any environmental parameters that can change the L and n can be detected by the FPI. For example, the temperature can change the L and n simultaneously, gas pressure can only change the n, vibration can only change the L, and so on.

In addition, combined with other materials or structures, FPIs have found extended applications in many fields. For example, FPIS with specific identification material can be used for the identification of noble gases. FPI's cavity filled with magneto fluid can be used for magnetic field detection, and FPIs based on the high resonant frequency film can be used for discharge monitoring in the oil pipeline.

2.2.4 Michelson Interferometer

Like the optical fiber FPI, the fiber version MI also works based on the reflected lights based on two arms structure. As shown in Fig. 2.8 (a), divided by an optical coupler, the incidence light is injected into two arms. After being reflected from the fiber end and meeting at the coupler, two beams interfere with each other. The arms' length difference inserts an OPD for interference. If the light intensity in the two arms is **I_1** and **I_2**, the length difference is **ΔL**, the fiber refractivity is **n**, and the output light intensity calculation equation is:

$$I = I_1 + I_2 + 2\sqrt{I_1 I_2}\cos\frac{4\pi n\Delta L}{\lambda} \qquad (2.14)$$

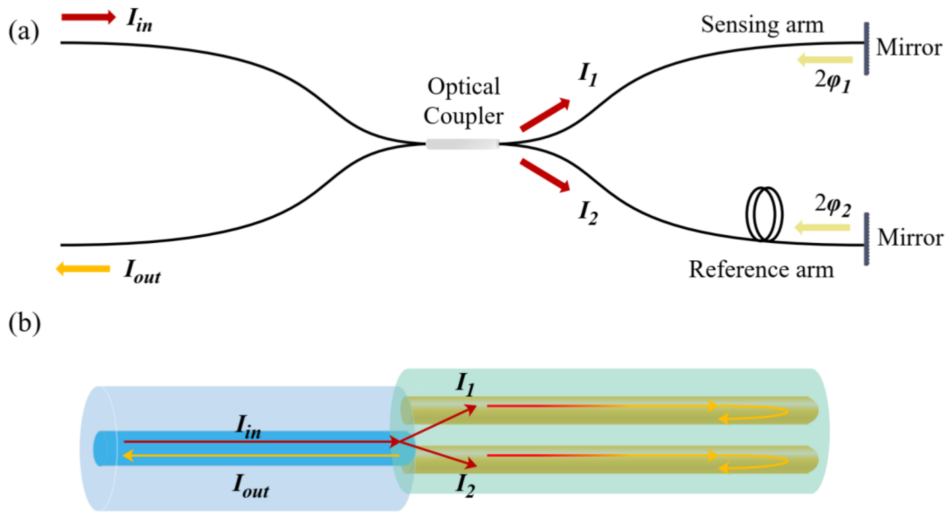

Fig. 2.8 (a) Traditional two arms MI, (b) Inline MI.

The MI can detect the external parameters that can change the arm length or refractivity, such as temperature, axial strain, lateral stress, and so on. Usually, the arm used for sensing is referred to as the sensing arm, while the other one is referred to as the reference arm.

In addition, all in-fiber MI structures have also been demonstrated over the past years by using MCF. The core-off fusion splicing structure acts as the optical coupler to split the amplitude of the incidence light into different cores as shown in Fig. 2.8 (b). Although the different cores' lengths are totally the same, the different refractivity between cores provides OPD for motivating the interference effect. Due to the compact size and high sensitivity, the in-fiber MI could be used in the fields of chemical and biomedical sensing.

2.2.5 Spectrum Parameters

The spectrum equation of the above four fiber interferometers can be unified as:

$$I = A + B\cos(\frac{2\pi}{\lambda} \bullet OPD) \tag{2.15}$$

When the ***OPD/λ*** equals 2m+1 (m=0,1,2,3... ...), the output light intensity reaches the minimum value I_m. Conversely, the ***OPD/λ*** equals 2n (n=0,1,2,3... ...), and the output light intensity reaches the maximum value I_M.

The fringe contrast of an interference spectrum is defined as:

$$K = \frac{I_M - I_m}{I_M + I_m} = \frac{B}{A} = \frac{2\sqrt{I_1 I_2}}{I_1 + I_2} \tag{2.16}$$

The greater the difference between ***I_1*** and ***I_2***, the less clear the fringe. If ***I_1=I_2***, ***K*** reaches the maximum value, which is 1. Thus, an actual interference experiment must bring the light intensity of the two participating lights closer together.

The wavelength difference of the adjacent maximum or minimum light intensity points is defined as the free spectral range (FSR), which can be calculated as:

$$FSR = \lambda_2 - \lambda_1 = \frac{\lambda_2 \lambda_1}{OPD} \approx \frac{\lambda^2}{OPD} \tag{2.17}$$

The ***FSR*** of an interferometer is different for different wavelengths. For convenience, the ***FSR*** at the communication wavelength 1550 nm is defined as a specific spectrum parameter for an interferometer. Take the spectrum of y=1+cos(πx) as an example, which is shown in Fig. 2.9, the FSR is 2 nm and the K value is 1.

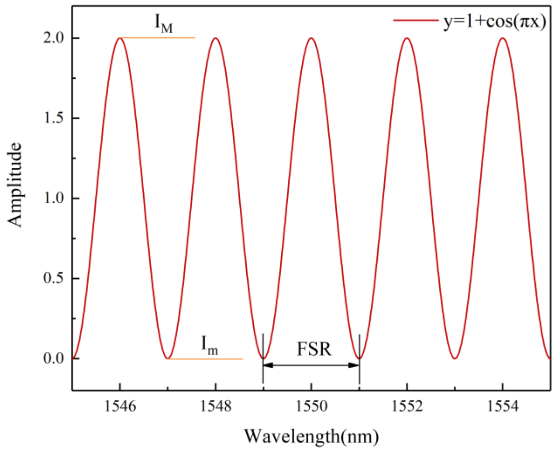

Fig. 2.9 The spectrum of y=1+cos(πx).

Like the frequency definition of a time domain signal, the interference spectrum's frequency is defined as ***f***=1/***FSR***. Then, any interference spectrum equation can be transformed to:

$$I = A + B\cos(2\pi f\lambda) = A + B\cos\omega\lambda \tag{2.18}$$

Drawing an analogy from the fast Fourier transform (FFT) in the time domain, the analogous fast Fourier transform (A-FFT) in the wavelength domain is defined as:

$$F(\omega) = \int_{-\infty}^{+\infty} I(\lambda) e^{-i\omega\lambda} d\lambda \tag{2.19}$$

Then, the frequency characteristics of the interference spectrum in frequency is expressed as:

$$F(I) = C + \frac{B}{2}[\delta(f - f_i) + \delta(f + f_i)] \tag{2.20}$$

δ(f) is the impulse function. C is a constant value, which is related to values of A and B. Usually, the one-sided amplitude spectrum is used, and the negative can be ignored. Thus, the A-FFT algorithm can be used to help analyze the frequency components of any interference spectrum.

The following figure gives examples of single frequencies, double frequencies, and triple frequencies superposition. The FFT results of the three circumstances are presented in Fig 2.10. The frequency component is displayed after calculating by the A-FFT algorithm. The peak amplitude is determined by the coefficient ***B*** of the cosine function as shown in Eq. (2.20).

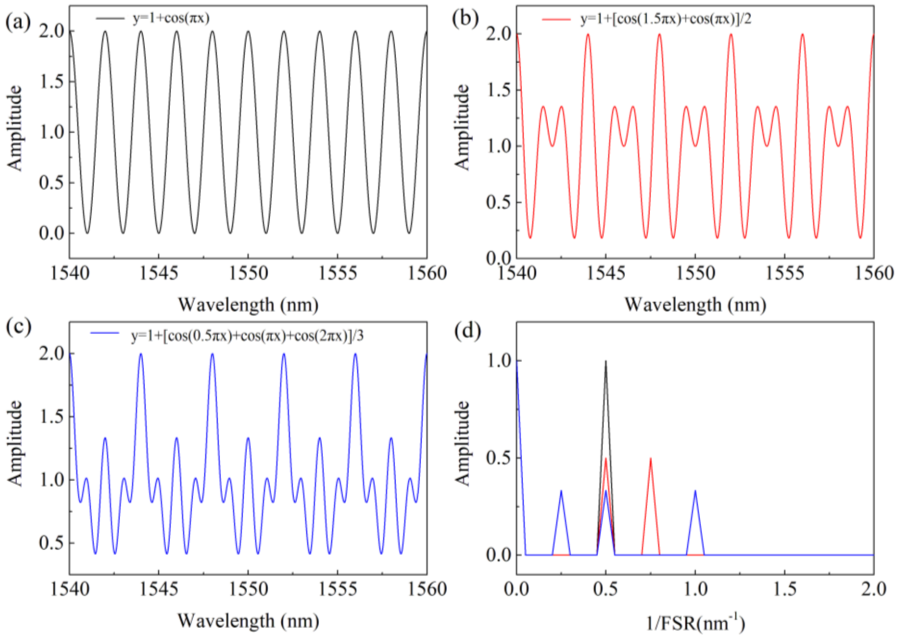

Fig. 2.10 (a) to (c) Examples of wave superposition with single frequency, double frequencies, and triple frequencies, (d) The FFT results of the wave superposition.

2.3 Optical Vernier effect

The rapid advancement of sensing technology leveraging optical fiber sensors has sparked a growing need for structures with heightened sensitivity and resolution. Over the past decade, the OVE has emerged as a solution to address these requirements.

The term "Vernier effect" derives its name from the Vernier caliper, devised by Pierre Vernier in 1631. The Vernier caliper incorporates two measurement scales: the main scale and a graduated auxiliary scale. By employing the graduated auxiliary scale, errors stemming from human estimation are mitigated, consequently enhancing measurement resolution.

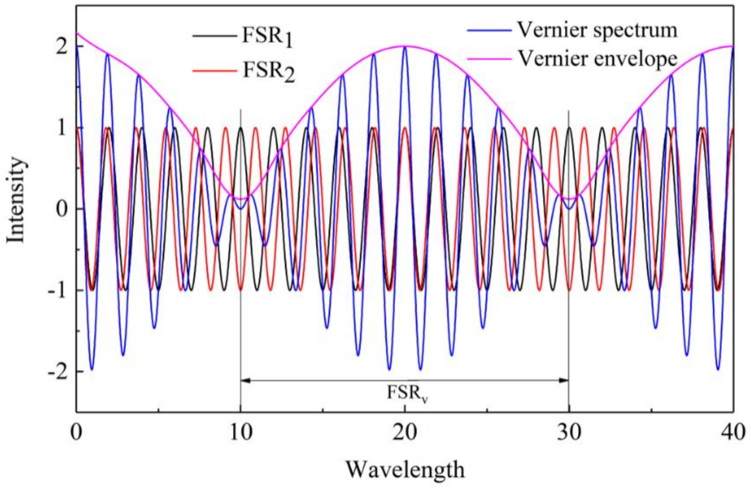

Fig. 2.11 The simulation superposition result of two cosine waves.

For OVE, it is built up by combining two interference signals with slight frequency differences together. The simulation superposition result of two cosine waves with a slight period difference is shown in Fig. 2.11. Generating from two interference signals overlapping, the Vernier envelope has enhancing characteristics. The two interference signals can be regarded as the two different scales of the Vernier caliper as shown in Fig. 2.12.

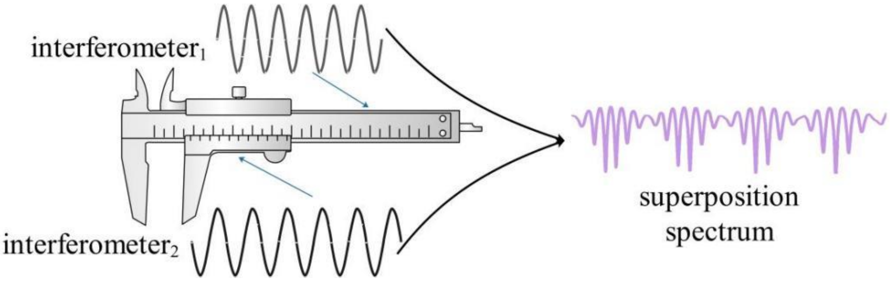

Fig. 2.12 The concept figure of the optical vernier effect.

2.3.1 Principle of Optical Vernier Effect

From the analysis in Chapter 2.1, the superposition of light intensity is essentially due to the vector sum results of vibration amplitudes. If the vibration amplitudes of two separate interference signals are expressed as:

$$\begin{aligned} E_1 &= a_1 + \mathrm{b}_1 \exp(-i\frac{2\pi}{\lambda}OPD_1) \\ E_2 &= a_2 + b_2 \exp(-i\frac{2\pi}{\lambda}OPD_2) \end{aligned} \tag{2.21}$$

The slight frequency difference used to introduce the OVE can be described mathematically, which is ***OPD*₁≈*OPD*₂**.

The light intensity superposition results can be calculated as:

$$\begin{aligned} I &= \left(a_1 + a_2\right)^2 + 2(a_1 + a_2)b_1 \cos(\frac{2\pi}{\lambda}OPD_1) \\ &+2(a_1 + a_2)b_2 \cos(\frac{2\pi}{\lambda}OPD_2) + b_1 b_2 \cos\left(\frac{2\pi}{\lambda}OPD_1 - OPD_2\right) \\ &+b_1{}^2 + b_2{}^2 \end{aligned} \tag{2.22}$$

Because ***OPD₁≈OPD₂*** >> ***OPD₁-OPD₂***, there is a frequency-dependent sinusoidal envelope modulating on the final light intensity and the ***FSR*** of it can be calculated as:

$$FSR_v = \frac{\lambda^2}{|OPD_1 - OPD_2|} = \frac{FSR_1 \bullet FSR_2}{|FSR_1 - FSR_2|} \qquad (2.23)$$

Where ***FSR₁*** and ***FSR₂*** are the ***FSR***s of the two interference signals, respectively. Note that the ***FSRᵥ*** can be adjusted by changing the frequency difference between the two interference signals.

A crucial attribute of the Vernier effect is the magnification factor ***M***, which indicates the extent to which the FSR of the envelope surpasses that of the individual interference signal.

$$M = \frac{FSR_v}{FSR_2} = \frac{FSR_1}{|FSR_1 - FSR_2|} \qquad (2.24)$$

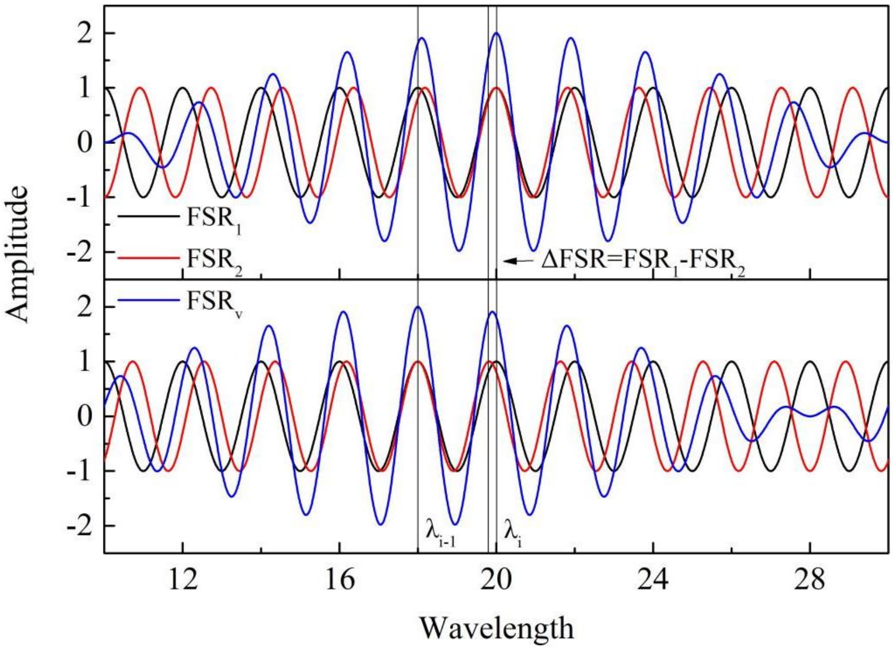

Fig. 2.13 Illustration of Vernier spectrum before and after shifting with a special value of (FSR_1-FSR_2).

Another definition of ***M*** is commonly used in the sensing field. In this case, ***M*** is the ratio of the envelope shifting value to the individual interference signal wavelength shifting value. As shown in Fig. 2.13, if $\boldsymbol{FSR_1>FSR_2}$, the envelope peak occurs at a wavelength of $\boldsymbol{\lambda_i}$. Then, if interference signals 2 blue shifts with $\boldsymbol{\Delta\lambda=FSR_1-FSR_2}$, two signals are coincident again at $\boldsymbol{\lambda_{i-1}}$. Then, the M can be calculated as:

$$M=\frac{\lambda_{i+1}-\lambda_i}{|FSR_1-FSR_2|}=\frac{FSR_1}{|FSR_1-FSR_2|} \qquad (2.25)$$

The above assumption wavelength shifting value can be deduced to any value and the M value will be entirely the same [28].

2.3.2 Configurations to produce Vernier Effect

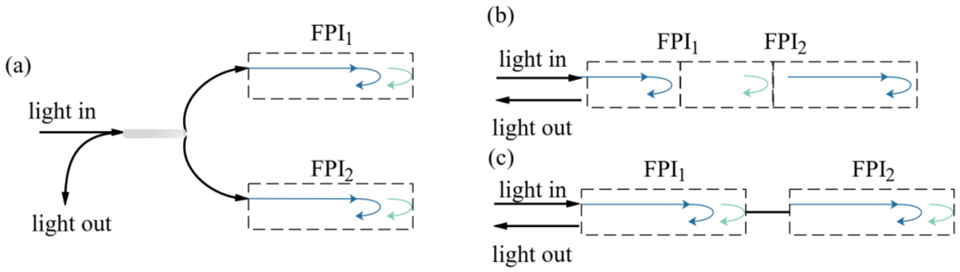

Fig. 2.14 Cascaded FPI configuration: (a) in parallel, (b) in series.

In terms of optical fiber interferometers, the OVE can be applied to different kinds of interferometer structures. The configurations based on the same type of interferometer are referred to as single-type Vernier sensors. The configurations based on different types of interferometers are referred to as hybrid-type Vernier sensors.

Among sensor structures based on the single type of interferometers, the dual FPI structures account for nearly half [29]. As shown in Fig. 2.14(a), one structure is to assemble two FPIs in parallel by using an optical coupler. The other structure is to assemble two FPIs in series. If the two FPIs are physically connected, there usually are three reflected mirrors in series to build up two FPIs. For two separated FPIs in series, they are connected by a section of fiber as shown in Fig. 2.14 (b) [30-32].

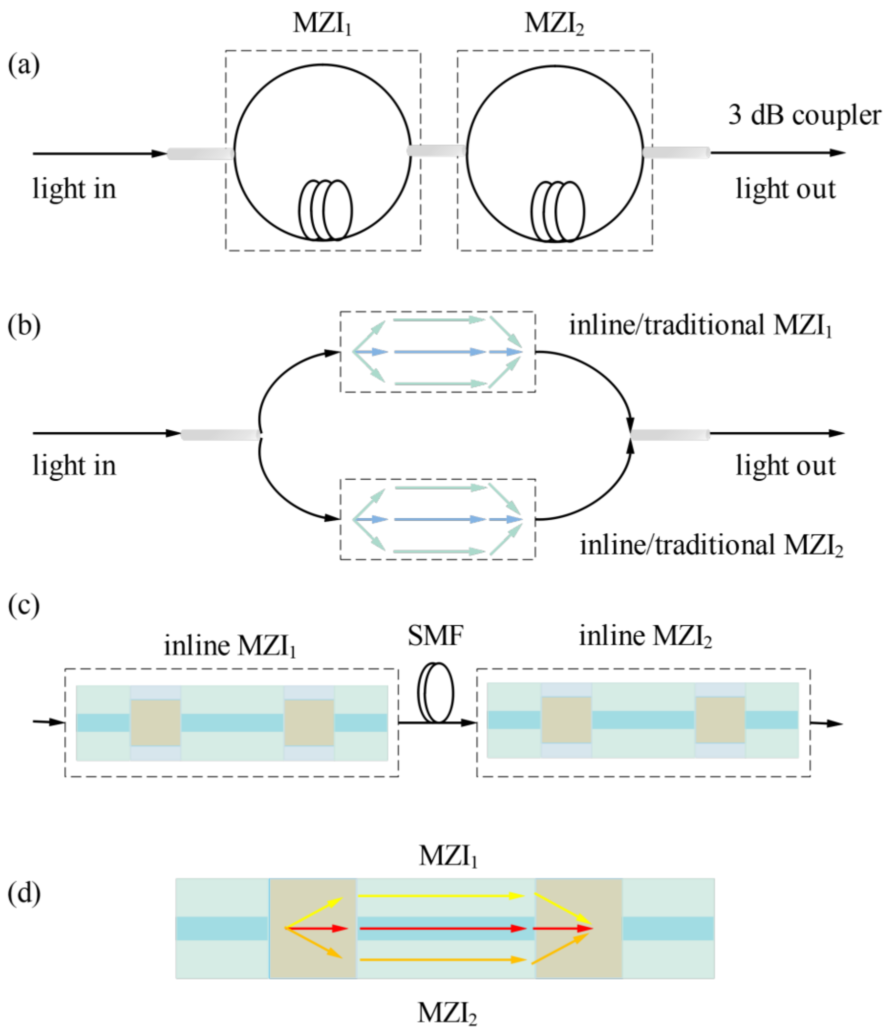

Fig. 2.15 Cascaded Mach-Zehnder interferometer configuration: (a) in series based on traditional MZIs, (b) in parallel, (c) in series based on inline MZIs, (d) all in one fiber.

The first demonstration of introducing OVE based on MZIs was reported by Liao et al. in 2017 [33]. In their work, two traditional MZIs with two arms are connected in series by an optical coupler as shown in Fig. 2.15(a). Soon afterward, a parallel configuration is designed and used by Wang et al as shown in Fig. 2.15(b) [74]. For configurations based on the inline MZIs structure, connected in series by SMF is the most common method as shown in Fig.

2.15(c) [34]. Moreover, parallel connection can also be integrated in the same fiber as shown in Fig. 2.15(d) [35].

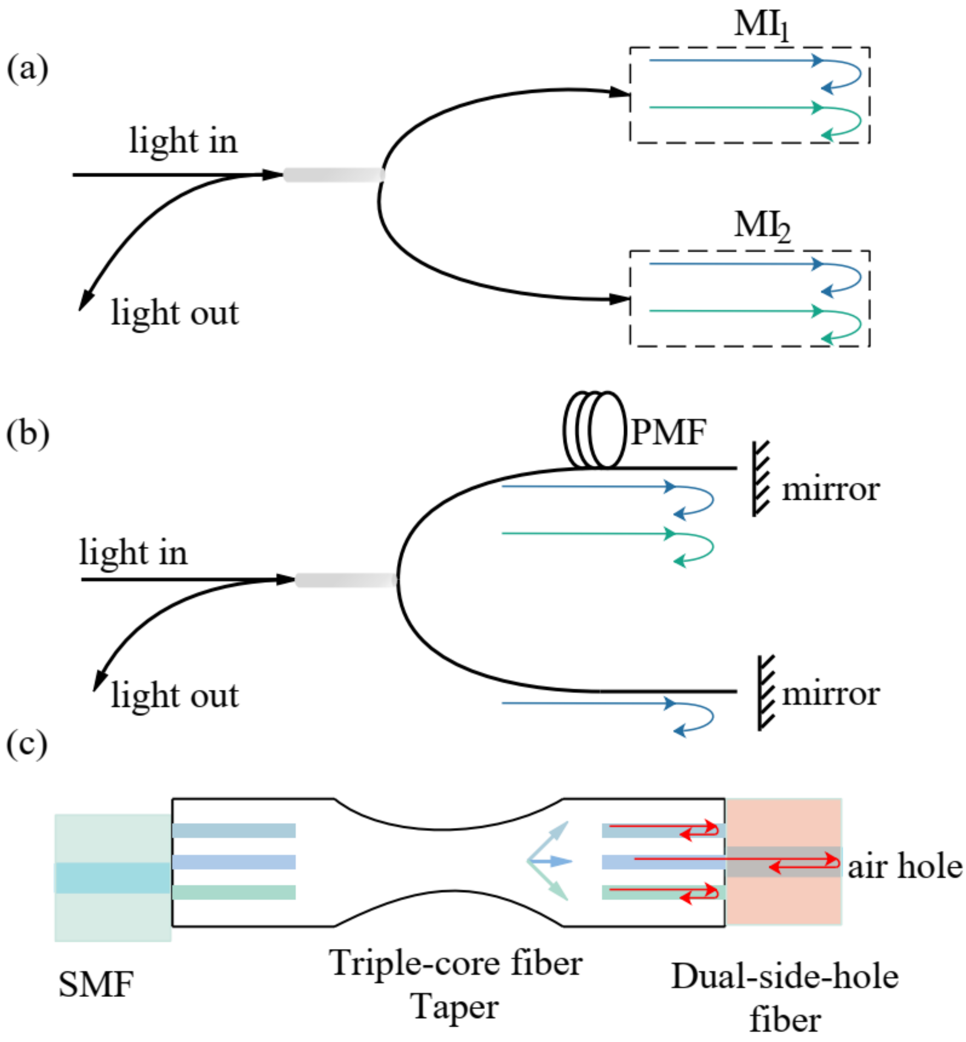

Fig. 2.16 Cascade Michelson interferometer configuration: (a) in parallel, (b) in parallel based on high BiF, (c) in one fiber.

Like the MZIs, the MIs also have two arms, but work based on the reflected lights. Connecting the output port of one MI with the input port of another MI or connecting two output ports to an optical coupler are available methods to introduce the OVE to MI as shown in Fig. 2.16 (a). However, the insert loss of this type of configuration is too high to be used in a sensing system. As shown in Fig. 2.16 (b), using the high BiF can build an inline MI vernier structure with only one optical coupler, and this structure is introduced in detail in Chapter 6 of this thesis [36]. Using the MCF as the light transmission channel can also help build an all-in-fiber MI vernier structure as shown in Fig. 2.16(c) [37].

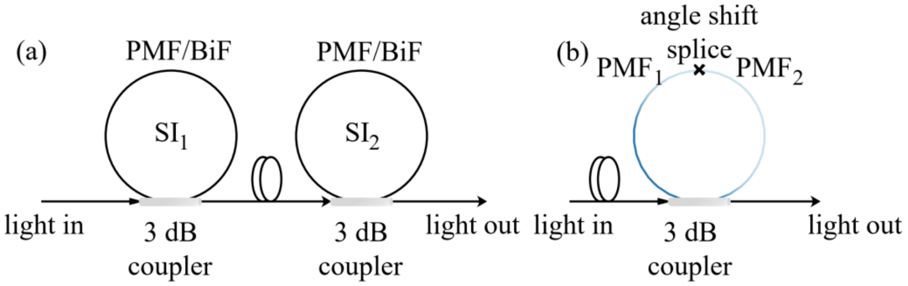

Fig. 2.17 Cascaded Sagnac interferometer configuration: (a) in series, (b) in the same fiber ring.

Because of the fiber loop in the SI, only in-series configurations are used to introduce the OVE before 2018 [38]. As shown in Fig. 2.17 (a), the output port of the first SI is connected to the input port of the second SI. A compact version to introduce OVE with SIs was presented by Wu et al. in 2018. By angle shifting splicing fusion of two sections of PMFs, the OVE is introduced in a single fiber ring as shown in Fig. 2.17 (b) [39].

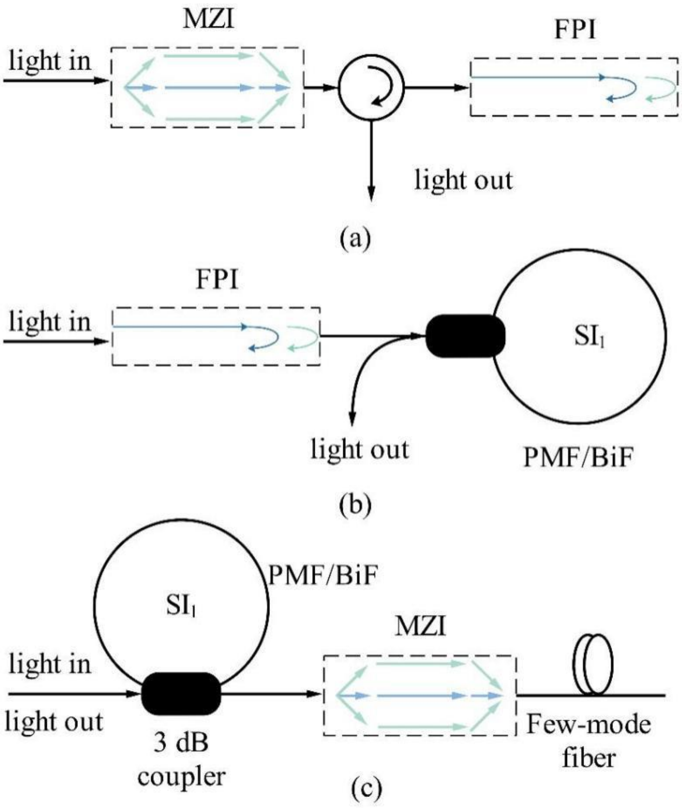

Fig. 2.18 The hybrid-type Vernier sensors: (a) MZI+FPI, (b) FPI+SI, (c) SI+MZI

For the single-type Vernier sensor, only one interferometer is used for sensing applications while the other one is just for reference applications. However, the hybrid type Vernier sensor can bring advantages together of both types of interferometers. Using two different types of interferometers can easily build up a dual-parameter sensing system. For example, the configuration based on MZI and FPI can simultaneously measure the temperature and acoustic wave as shown in Fig. 2.18 (a). Using one type of interferometer as the demodulation tool for another type of interferometer based on OVE, as introduced in [40]. In addition, if two interferometers have opposite sensitivities, the enhanced OVE can be introduced for high-resolution sensing. In this special case, there is no specific reference interferometer, the two interferometers reference each other [41]. Fig. 2.18 (b) and (c) show some other hybrid-type Vernier sensors.

2.4 Summary

In this chapter, the common methods to motivate interference in the optical field are introduced first. Then, four different fiber interferometer structures and their work mechanism are presented one by one. To improve the interferometers’ sensitivity, the concept of OVE is introduced, including the working principle and key parameters. Finally, common configurations based on different interferometers are presented to help get a clear understanding of the OVE.

Chapter 3 A Sagnac Interferometer Sensor for Respiratory and Heart Rate Monitoring Based on the Six-hole High Birefringence Fiber

3.1 Introduction

The variation of respiratory rate (RR) and heart rate (HR) is an important early warning signal of many diseases, such as cardiovascular diseases [42], fatigue [43], apnea [44], mental stress [45], and respiratory abnormalities [46]. Constantly RR and HR monitoring of the patients allows medical workers to evaluate the patient’s physiological condition timely and then implement intervention therapy appropriately.

In recent years, various electronic sensors based on different data acquisition methods have been proposed for HR monitoring, such as fingertip cardio tachometer [47], wrist cardio tachometer [48], and chest electrodes electrocardiogram instrument [49]. As for RR monitoring, the head-mounted respiratory monitor takes up the primary market [50]. However, all electronic sensors cannot be used in the high electromagnetic environment, such as magnetic resonance imaging equipment, because they are sensitive to electromagnetic interference. Moreover, most electronic sensors are contact type, which is uncomfortable with constraints to the person’s activities.

Utilizing indirect contact optical fiber sensors as the primary sensing component in a vital signs monitoring system offers a clever solution to electromagnetic interference and comfort issues. Moreover, optical fiber sensors boast numerous unique advantages, including compact size, lightweight, resistance to chemical corrosion, and long-term stability [51]. An increasing number of monitoring systems based on optical fiber sensors, proposed by researchers worldwide, further validate these advantages.

In 2014, Chen et al. employed a micro-bend MMF-based sensor to simultaneously measure HR and RR [52]. Subsequently, Massaroni developed a smart textile integrating fiber Bragg grating (FBG) technology for RR monitoring [53]. Then, Tan et al. introduced a sensor based on twin-core fiber (TCF) for non-invasive monitoring of both RR and HR in 2019 [54]. Finally, Yuan et al. successfully manufactured a hollow-core Bragg fiber (HCBF) based MZI sensor for RR monitoring [55]. However, a limitation present in these sensors is their sensitivity to temperature variations, requiring recalibration under varying temperature conditions.

In this chapter, we propose a temperature-insensitive fiber system for non-contact vital signs monitoring. The core sensing element comprises a Sagnac interferometer (SI) constructed using an optical coupler and SH-HiBiF. The SH-HiBiF, composed of pure fused silica without any additional doping, exhibits temperature insensitivity. Due to the stress-induced birefringence effect in this fiber, the interference spectrum of the SI, generated by a broad-spectrum light source, experiences linear shifts with variations in lateral stress. Injecting single-wavelength light around the Q points (the points on the interference spectrum with the highest slope) into the SI enables modulation of the output light intensity by the HR and RR signals. Through demodulation using a photodetector (PD), the output light intensity signal, along with the HR and RR signals, can be converted into an electronic signal. Subsequent data processing facilitates the extraction of the individual's HR and RR signals.

3.2 Sensor Structure and Fabrication Process

3.2.1 Six-hole high birefringence fiber

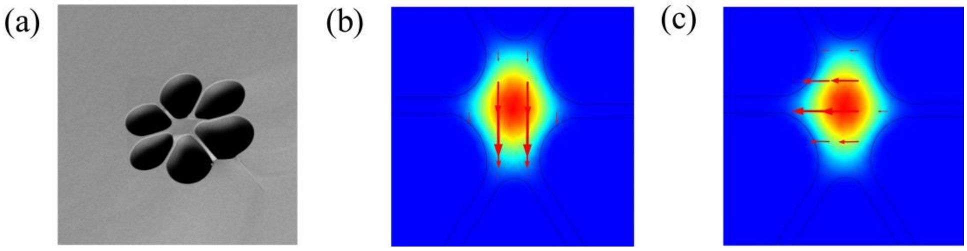

Fig. 3.1 (a) The cross-section view of the SH-HiBiF under the SEM. (b) and (c): The simulation mode field distribution: LP_{01}-x and LP_{01}-y.

The SH-HiBiF cross-section view is displayed in Fig. 3.1(a). Same as the standard SMF, the SH-HiBiF outer diameter is 125 µm. Six drop-shaped air holes distributed evenly surround the fiber's central point. The dimension of each hole is ~22 µm×~27 µm. Because of the circular asymmetric structure of the suspended core part, a stress-induced birefringent effect is introduced into this fiber. The size of the central suspend part is ~8 µm×4 µm.

The simulation results of the core mode are shown in Fig. 3.1(b) and (c). The red arrows point out the electric fields' direction of the fundamental mode LP_{01}. The calculated fundamental mode is elliptical, which has two perpendicular polarization states LP_0-x and LP_0-y. The ERI of them are 1.43546, and 1.43572 @ 1550 nm, giving a phase modal birefringence of ~ 2.59×10^{-4}. Thus, this fiber can be used for building up SI.

3.2.2 Sensor Fabrication

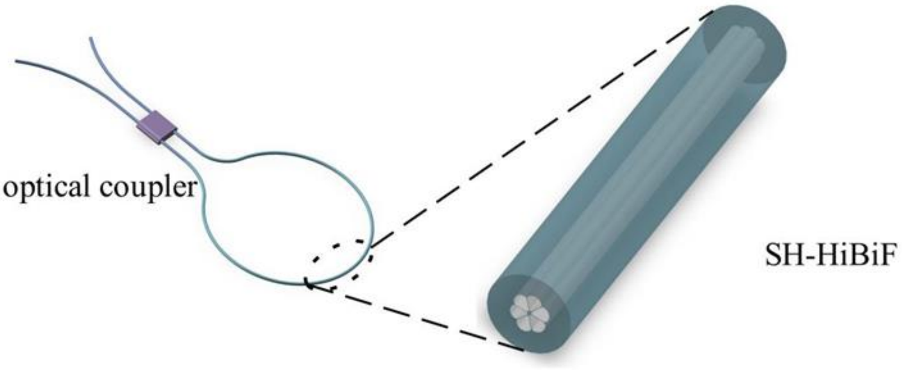

Fig. 3.2 The structure diagram of the SI based on the SH-HiBiF.

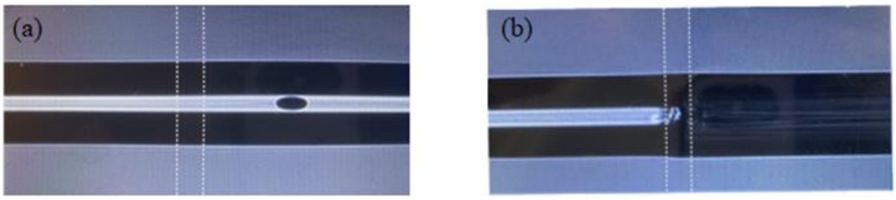

Fig. 3.3 The fusion splicing image between SMF and SH-HiBiF: (a) under a single-time high-power mode; (b) under a multi-time low-power mode.

The SI structure is shown in Fig. 3.2. When fusion splicing the SMF with the SH-HiBiF, manual fusion mode is chosen because of the large air holes in the SH-HiBiF. Meanwhile, multiple low-power fusion methods are utilized instead of employing a single high-power fusion method. The fusion splicing power is 30 units, the discharge time is 100 ms and the fusion splicing time is 5. The comparison of fusion outcomes between SMF and SH-HiBiF is depicted in the figure. Employing a single high-power method leads to collapse at the fusion point, thereby altering the structure of SH-HiBiF. Conversely, when fibers are fused using multiple low-power methods, the boundary between SMF and SH-HiBiF is easily discernible.

3.3 Spectrum Analysis and Sensing Principle

The spectrum obtained with 25 cm SH-HiBiF is shown in Fig. 3.4. The waveform of the spectrum is similar to the waveform of the cosine function. Thus, it can be inferred that the birefringence effect is stimulated in the fiber. The FSR of it is about 4.2 nm. According to Chapter 2.2.1, the output light intensity of the proposed SI is expressed as

$$I = I_1 + I_2 + 2\sqrt{I_1 I_2}\cos\left[\frac{2\pi}{\lambda}\left(n_1 - n_2\right)L\right] \tag{3.1}$$

The light intensity of the two perpendicular polarization states are $\boldsymbol{I_1}$ and $\boldsymbol{I_2}$, the wavelength is $\boldsymbol{\lambda}$, the ERI are $\boldsymbol{n_1}$ and $\boldsymbol{n_2}$, and the fiber length is $\boldsymbol{L}$. If the phase equals (2m+1)π, the intensity of the output light will reach the minimum value. Then the spectrum dip wavelength can be calculated by:

$$\lambda = \frac{2\left(n_1 - n_2\right)L}{2m+1} \tag{3.2}$$

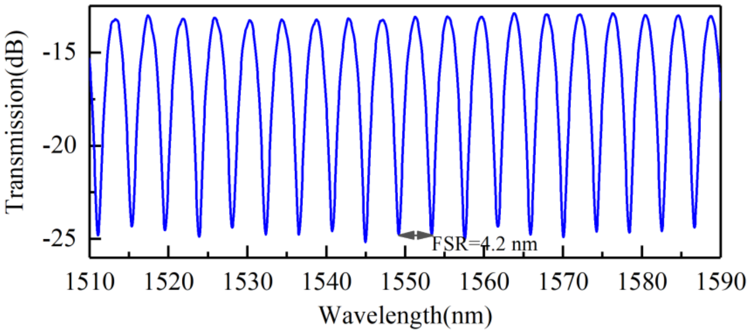

Fig. 3.4 The interference spectrum of the proposed SI.

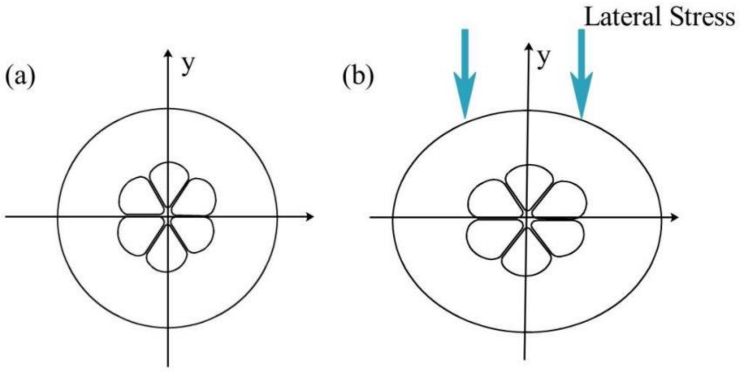

Fig. 3.5 The cross-section of the SH-HiBiF (a) before being added lateral stress, (b) after being added lateral stress.

When the fiber is added lateral stress, the fiber will deform as shown in Fig. 3.5. Then, the ERI of the two perpendicular polarization lights change correspondingly, resulting in the interference dip shift. The wavelength shift value can be obtained:

$$\frac{d\lambda}{dP}=\frac{2L}{2m+1}\left(\frac{dn_1}{dP}-\frac{dn_2}{dP}\right) \tag{3.3}$$

3.4 Experimental Results

3.4.1 Lateral Stress Sensing

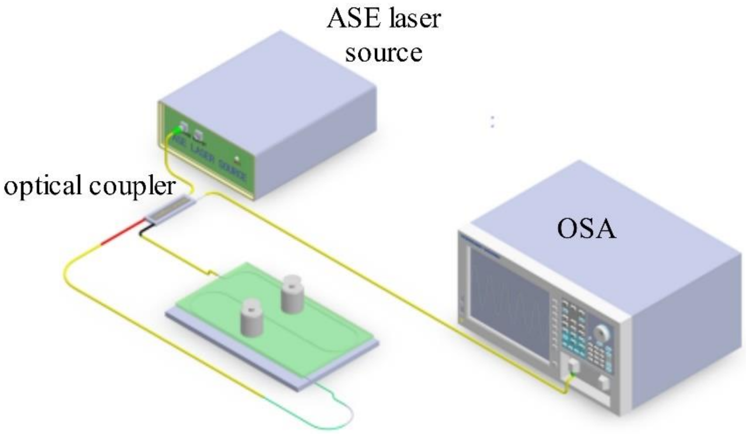

Fig. 3.6 The experiment system for the lateral stress sensing.

The emitted light originates from an amplified spontaneous emission (ASE) laser, spanning a spectral range from 1500 nm to 1600 nm. Subsequently, the final spectrum is captured utilizing an optical spectrum analyzer (OSA, AQ6070D), of which the resolution is 0.02 nm. To facilitate measurement, approximately 15 cm of SH-HiBiF is coiled and secured to a horizontal platform. Another acrylic plate is then positioned atop the fiber to ensure uniform pressure distribution. Notably, lateral stress is exclusively applied to the SH-HiBiF. This lateral stress variance is induced by the pressure exerted by weights, with each weight measuring 1.25 kg. The weights are put at the central point of the upper plate to make sure the upper plate is in a horizontal position. With the dimensions of the acrylic plate at 20 cm × 10 cm, the pressure intensity exerted on the fiber by each weight is calculated as 625 Pa.

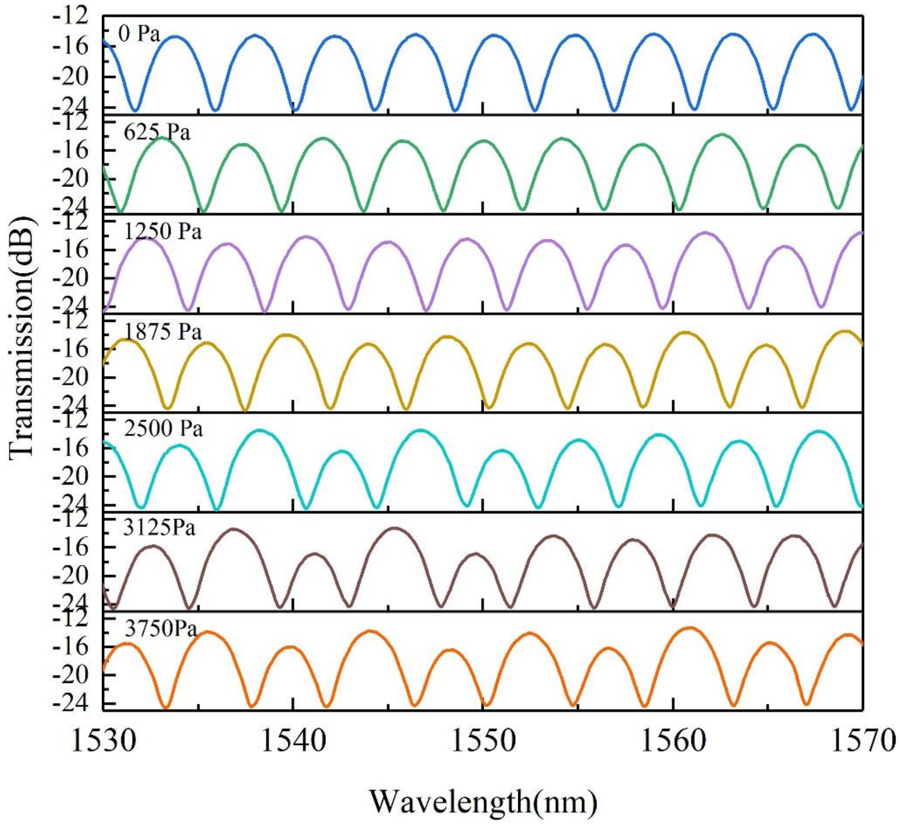

Fig. 3.7 The sensor spectrum under different lateral stress.

The interference dip shifts with variations in lateral stress, as depicted in Fig. 3.7. Notably, the spectrum shifts towards shorter wavelengths with increasing lateral stress. Fig. 3.8 displays the linear relationship between pressure intensity and dip wavelength around 1550 nm. The slope of the fitting curve signifies the sensitivity, computed as 1.72 pm/Pa (equivalent to 1.72 nm/kPa). The substantial degree of fitting, with an R^2 value of 0.99043, suggests that the sensor demonstrates a linear response to alterations in lateral stress.

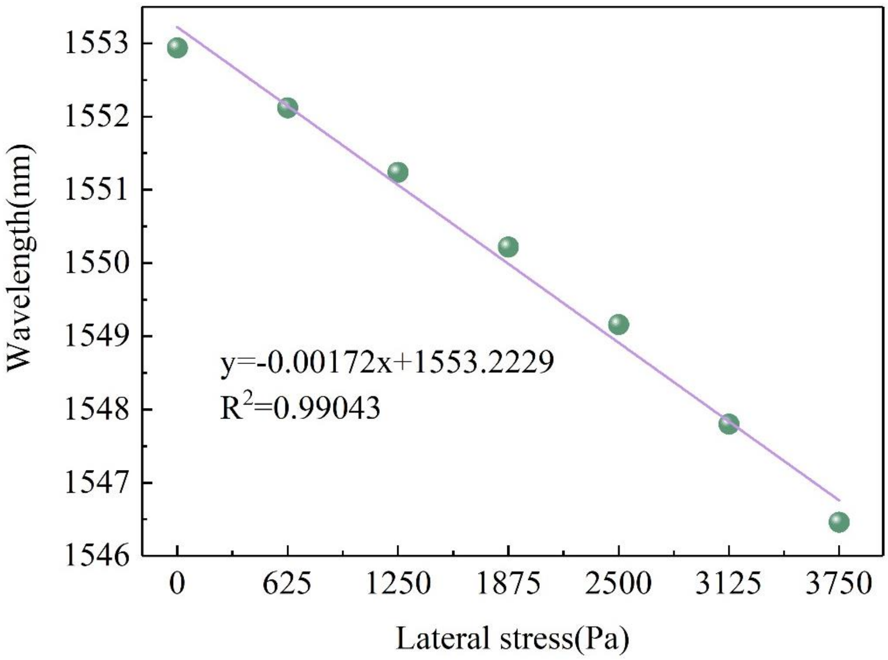

Fig. 3.8 The fitting curve between the interference dip around 1550 nm and added lateral stress.

3.4.2 Vital Signs Monitoring

From the experiment results mentioned above, it's evident that the designed SI effectively detects lateral stress changes by monitoring the interference dip shift under a broadband light source. If a single wavelength laser is employed as the light source, the lateral stress variation would manifest as a change in the output light intensity. For optimal performance, the laser wavelength should align at the wavelength of the spectrum's Q points. Q points are the points with the highest slope in the spectrum. If the input lateral stress change is a periodical signal, the following output light intensity change is also a periodical signal with the same frequency as shown in Fig. 3.9. Then, a PD can be used for demodulating the light intensity change, with outputting an electrical signal, of which the frequency is the same as the original input HR and RR signals. Thus, the proposed SI structure can be used for vital signs monitoring.

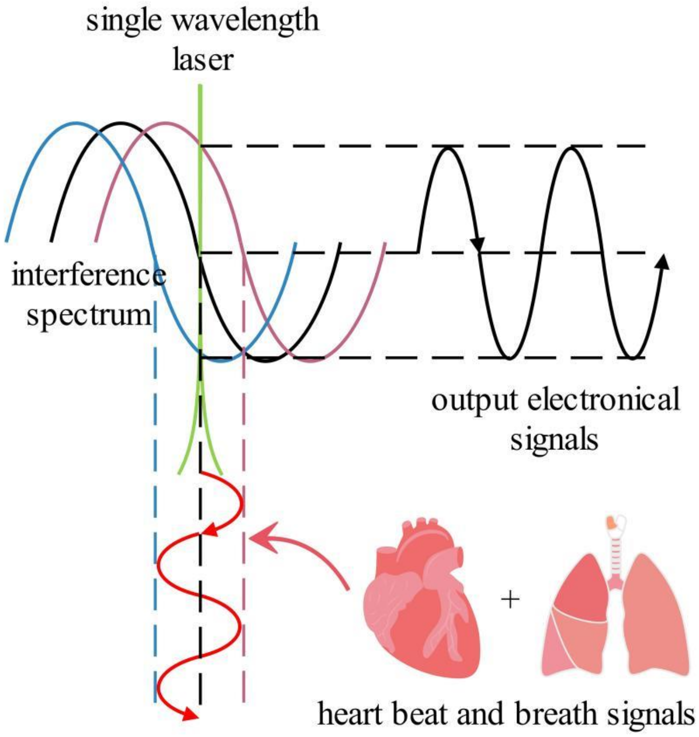

Fig. 3.9 The principal diagram of light intensity demodulation.

As shown in Fig. 3.10, a section of the SI is struck between two acrylic plates and then put under the body of a still-lying person. The people’s heartbeat and breath introduce a periodical lateral stress fluctuation on the sensor. Using this sensor and a PD, the heartbeat and breath signal can be transferred into an electrical signal, which is more easily analyzed and recorded. The HR signal recorded by this method is a ballistic force signal generated by the heart, which is referred to as a ballistocardiograph (BCG).

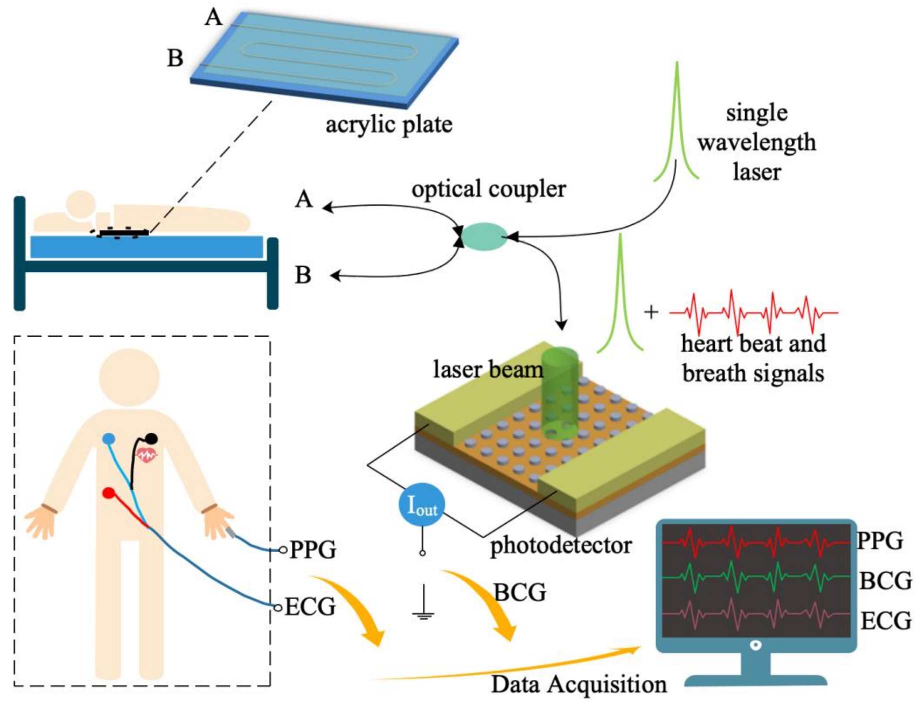

Fig. 3.10 The vital signs monitoring system.

The photoplethysmography (PPG) and Electrocardiography (ECG) signals are recorded simultaneously to verify the usability of the proposed sensor. The PPG and ECG signals are recorded by a fingertip and electrode-type cardio-tachometer, respectively. The three different vital signals in a time range of 30 seconds are displayed in Fig. 3.11. The orange line is the PPG signal, which only has a heartbeat signal but no breath signal. The purple line is the ECG signal, which has a less obvious breath signal. The blue line is the original output signal from the photodetector. There are several peaks, which is one by one corresponding to the ECG and PPG heartbeat signal. That is, the peaks are introduced by the heartbeat. Filtered by a low-frequency filter, the breath signal is obtained and marked as a green line. The breath fluctuation is more obvious than the ECG signal. The experimenter's breathing frequency is about 13 times every minute, which is in the normal range of the human respiratory rate.

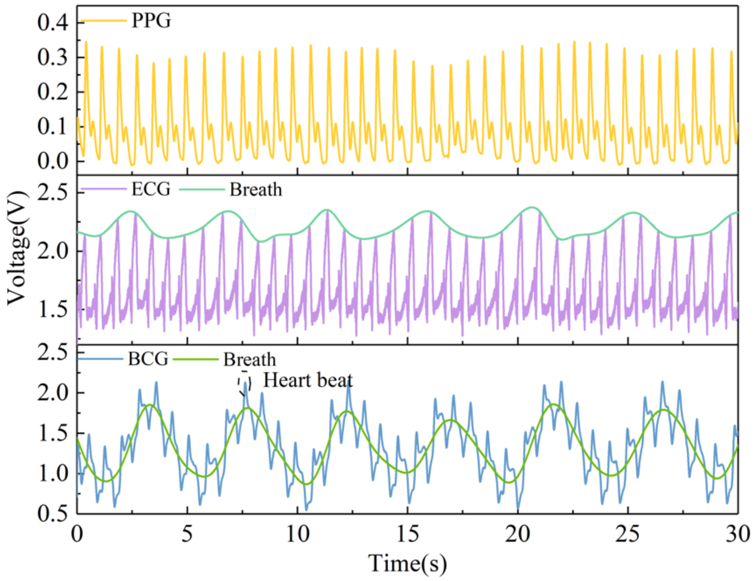

Fig. 3.11 The original vital signs data were obtained at three different body parts: PPG, ECG, and BCG.

Because the frequency of the heartbeat signal is around 1 Hz, a band-pass frequency filter is used to extract the heartbeat signal. The result is shown in Fig. 3.12 by a red line. It can be seen that the proposed sensor recovers the heartbeat signal detail by detail. There is a time delay between the BCG and ECG signal. The reason for this phenomenon is that the monitoring mechanisms for the two signals are entirely different. The ECG signal is obtained by monitoring the electronic signal during the heartbeat. The BCG signal is obtained by monitoring the body vibration caused by the heartbeat.

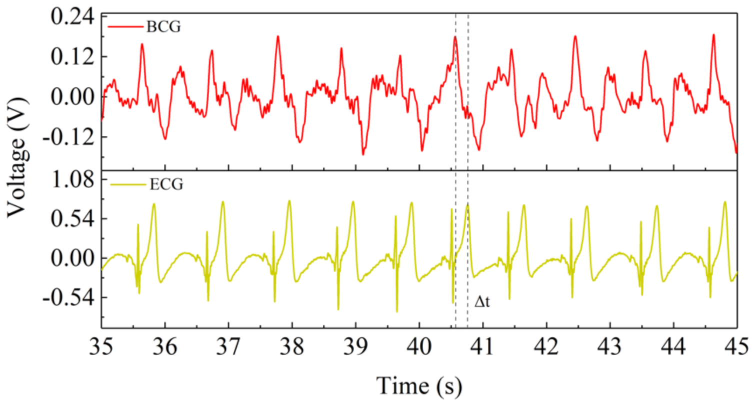

Fig. 3.12 The heartbeat signals after being by a 1 Hz band-pass frequency filter.

To validate the accuracy of the BCG signal obtained by the proposed sensor, the FFT algorithm is employed to determine its frequency. The results are depicted in Fig. 3.13. Notably, the main FFT peaks of both the BCG and ECG signals align precisely at a frequency of 1.0737 Hz. This indicates that the duration of a single heartbeat period for both signals is identical, yielding an approximate heart rate of 65 beats per minute. Consequently, the proposed sensor effectively captures the heartbeat signal and can serve as a reliable alternative to electric cardio-tachometers, particularly in environments prone to high electromagnetic interference

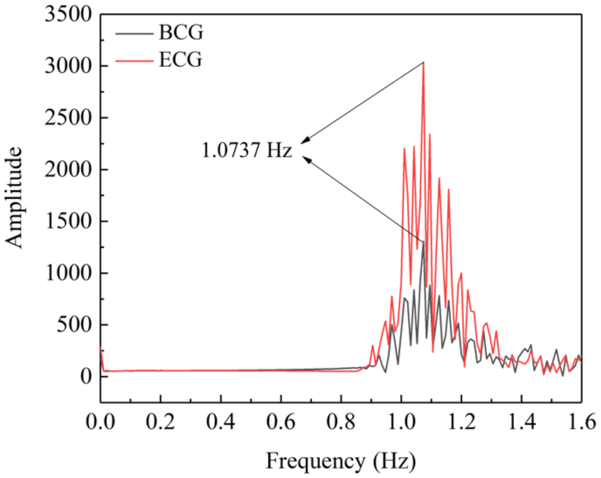

Fig. 3.13 The FFT result of the BCG and ECG signal.

Furthermore, the sensor exhibits minimal sensitivity to temperature fluctuations owing to the fabrication material of the SH-HiBiF, which consists of pure fused silica without any doped particles. Consequently, temperature variations do not affect the characteristics of the sensor, rendering it more stable for practical applications.

3.5 Summary

In this chapter, an optical respiratory and heart rate non-invasive monitoring system is set up and proven to work well. The core part of this system is an optical fiber SI, built up by a 3 dB coupler and a section of homemade SH-HiBiF. Because of the circular asymmetric structure in the fiber, the time-domain spectroscopy of the SI will shift linearly as the lateral stress changes with a sensitivity of 1.72 nm/kPa. Thus, if a single wavelength laser is injected into the fiber, the respiratory and heart rate signals can modulate the light intensity and finally be demodulated out by a PD even if not in contact with the human body, which is more comfortable for the patient. The temperature cross-sensitivity of this monitoring system is relatively low because the raw material of the sensing part is pure fused silica. Performed experiments demonstrate the system’s feasibility in further research in the biomedical field.

Chapter 4 Inline Mach-Zehnder Interferometer for Axial Strain Measurement Based on the Twin-core and Single-hole fiber

4.1 Introduction

Axial strain is one of optical fiber sensors' commonly measured physical parameters. Researchers have proposed many structures based on single-mode fiber (SMF) for axial strain measurement. For example, different types of fiber grating, including FBG [56], long-period fiber grating (LPFG) [57], long helical period fiber grating (HLPFG) [58], and tilted fiber Bragg grating (TFBG) [59] are inscribed in SMFs because the grating period changes with the applied axial strain linearly. Many SMF-based interference structures, including but not limited to taper [60], offset [61], and S or Z-shaped structures [62-64], are designed and fabricated with the expectation of higher sensitivity. In addition, several axial strain sensors based on special microstructure fibers are gradually emerging with the development of fiber drawing technology. Hollow-core fiber (HCF) [65], polarization-maintaining fiber (PMF) [66], and twin-core photonic crystal fiber (TCPCF) [67] are some examples. However, such axial strain sensors' sensitivities are relatively low, always under 10 pm/με [68].

An effective way to enhance the sensitivity of the optical fiber sensors is by building a cascaded interference structure based on the OVE [69]. As introduced in Chapter 2.3, SI, FPI, MI, MZI, and hybrid-type configurations can all be used for exciting the OVE. However, it is unsuitable for measuring the axial strain change along one dimension for optical fiber SI because of the fiber ring. For optical fiber FPI, the common structures are fusion splicing SMF with HCF [70], splicing fusion SMF based on offset structure [71], or etching an air cavity by laser [72]. The cavity length of the FPI is about 50 μm which needs a relatively high precision control process. Thus, FPI sensors with good repeatability are challenging to obtain. Two MIs cascaded structures are rarely reported because their complex sensing structures are difficult to build up. The hybrid-type configuration is built up by combining different types of interferometers, which are always associated with complicated structures and complex fabrication processes. For MZI, the sensing mechanism is easy to achieve, and the fabrication process does not need high precision because its size is always at the level of ~5 mm.

The first demonstration of using MZIs based on the OVE was reported by Liao et al. in 2017 [73]. In their work, two traditional MZIs with two light arms are connected in series by 3 dB couplers to measure curvature and temperature. Then, Wang et al. a parallel configuration based on two MZIs separated by two 3 dB couplers in 2019 [74]. The other type of MZI-based sensor is building up the two MZIs all in the fiber, which do not need any other connected devices. Compared to the aforementioned two types of structure, the size of the third sensor's design is much smaller, which is helpful in integrated systems. In addition, the sensitivity of the third type of sensor is much higher than the other two types [75].

In this Chapter, a cascaded MZI sensor based on the OVE is designed and fabricated in one fiber to measure axial strain and temperature simultaneously. Every single MZI is based on the TCSHF. Since the construction method of the MZI is quite simple and does not need high precision, the repeatability of the fabrication process can be guaranteed. By optimizing the fusion splicing parameters, the fusion collapse is avoided, and then an MZI with good robustness is achieved. After two MZIs are cascaded together, the sensor can measure the axial strain with a sensitivity of ~ 17 pm/με from 0 to 2000 με and temperature with a sensitivity of ~1.16 nm/°C from 30 to 70 °C. The sensitivities are much higher than the common MZIs proposed before. Moreover, the cascaded structure can simultaneously detect the axial strain and temperature change in the acceptable error range.

4.2 Sensor Structure and Fabrication Process

4.2.1 Mach-Zehnder Interferometer

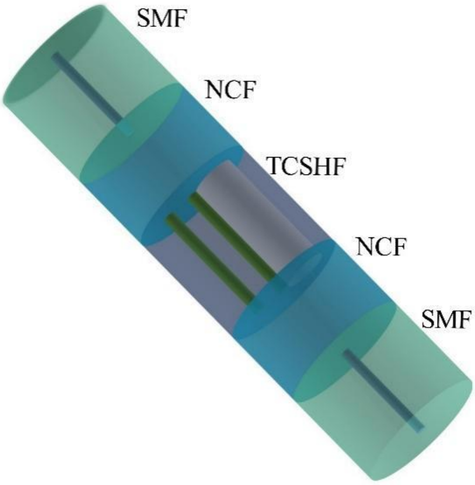

Fig. 4.1 The schematic diagram of the MZI structure is based on NCF and TCSHF

As shown in Fig. 4. 1, a short section of TCSHF is fusion spliced between two pieces of No core fiber (NCF). The function of the NCF is quite the same as that of the optical coupler. It can enlarge the mold field so that the input light can be divided evenly into the different transmitted channels of the TCSHF and couple the light from different channels together so that the final output light can propagate in SMF. The two cores and the air hole create the possibility of building up an MZI.

4.2.2 No Core Fiber

The refractive index profile in NCF is usually graded, with the RI gradually decreasing from the center to its edge, which makes the fiber act as a lens to focus light at a specific length. A simulation experiment is conducted to determine the appropriate length of the NCF, impacting the mode field distribution both at the fusion splicing point with the TCSHF and NCF itself. To accommodate the circular symmetry of both the SMF and NCF, a 2D model of the SMF-NCF structure is established, as shown in Fig. 4.2 (a). The SMF has a length of 5 mm, with an ERI of 1.4504 for the core and 1.4447 for the cladding. The NCF measures 20 mm in length, with an ERI of 1.4575. Fig. 4.2 (b) illustrates the mode field distribution within the SMF-NCF structure. It can be seen that there will be many autofocus points along the direction of light transmissions, such as the trisection autofocus points at the position of ~5 mm NCF, the halving autofocus points at the position of ~7.5 mm NCF, and the entire autofocus point at the position of ~10 mm NCF. The blue line in Fig. 4.2 (c) represents the relative optical field intensity in the SMF-NCF structure. The position of the maximum intensity value 1 is at the entire autofocus point.

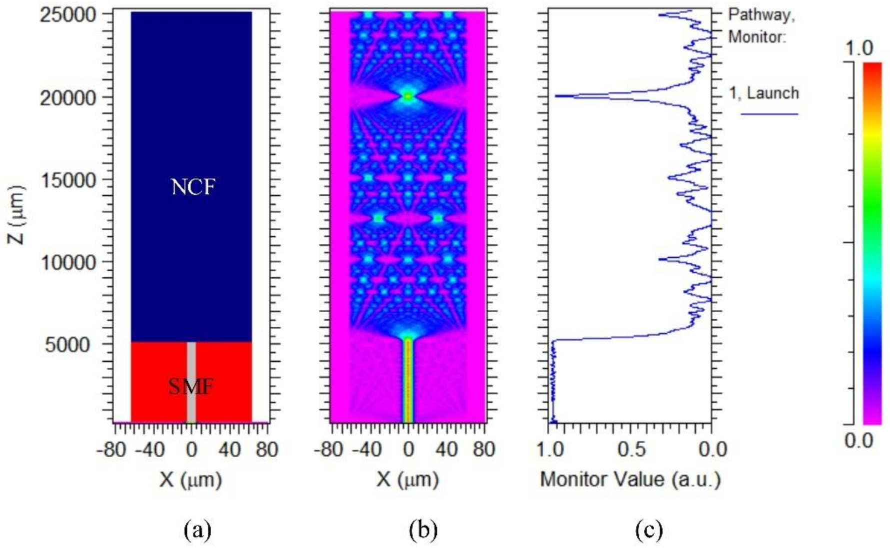

Fig. 4.2 (a) The 2D model of the SMF-NCF structure, (b) The mode field distribution in the SMF-NCF structure, (c) The corresponding transmission light intensity in the SMF-NCF structure.

For building up an MZI in TCSHF, the light field should be as even as possible at the NCF-TCSHF fusion splicing point. Thus, the length of the halving auto-focus points and the entire autofocus point cannot help to achieve the objective. Finally, taking the final size of the sensor and the cutting precision of the optical fiber cleaver (SUMITOMO ELECTRIC INDUSTRIES, LTD. FC-6S) into account, the final length of the NCF is determined as 5 mm.

4.2.3 Twin-core Single-hole Fiber

The TCSHF utilized in this study was custom-designed and manufactured by Yangtze Optical Electronic Co., Ltd. As illustrated in Fig. 4.3 (a), the TCSHF features a clear cross-section revealing its structure. It consists of two cores, namely core A and core B, along with an air hole. Core A, positioned centrally within the fiber, has a diameter of approximately 9.8 μm. Positioned at a distance of roughly 25 μm from the central point, core B shares the same diameter as core A. Similarly, the air hole, with a diameter of around 42.2 μm, is situated off-center at a distance of approximately 27 μm. Notably, the center points of both cores and the air hole align along the same line, as depicted in Fig. 4.3. The effective refractive index (ERI) of the material composing the two cores is measured at 1.4625@630nm, while the ERI of the cladding material is recorded at 1.4575@630nm.

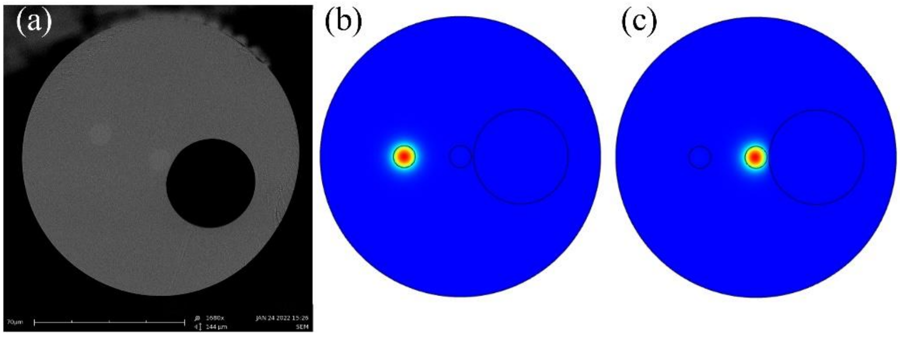

Fig. 4.3 (a) The cross-section chart of the TCSHF under an electron microscope, (b) The fundamental mode at core A, (c) The fundamental mode at core B.

Fig. 4.3 (b) and Fig. 4.3 (c) display the fundamental mode distribution simulation results in the TCSHF. The simulation wavelength is 1550 nm. Different from the uniform distribution of the mode field in core A, the mode field distribution in core B is off the center point and away from the air hole. The EFI of the fundamental mode in cores A and B is 1.460148 and 1.460009, respectively.

Since there is a big air hole in the TCSHF, a collapse will appear when TCSHF is spliced with other fiber types. Several splicing fusion experiments were conducted to find out the most proper splicing fusion parameters, which can help avoid this undesirable collapse feature. The final optimum fusion parameters are shown in Table II.

Table II The Optimum Fusion Parameters Between TCSHF and NCF

Parameter	Value
Clean discharge intensity	30
Clean discharge time	100 ms
The first discharge intensity	90
The first discharge time	300 ms
The second discharge intensity	20
The second discharge time	200 ms
Pre-melting time	100 ms

Splicing fusion front-end	20 µm
Propulsion distance along the Z-	15 µm
Alignment type	cladding

Fig. 4.4 displays the fusion splicing point between NCF and TCSHF based on the parameters in Table II. The boundary between the two types of fiber is distinct, and the collapse phenomenon did not happen as expected.

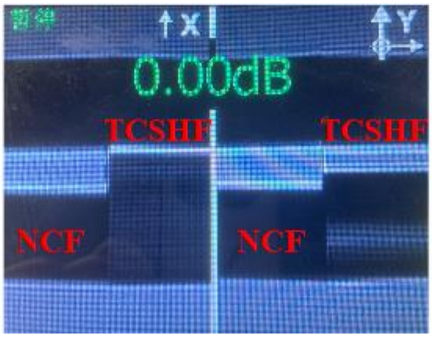

Fig. 4.4 The microscope image of the fusion splicing point between NCF and TCSHF

The MZI-based sensors with different lengths of the TCSHF are obtained, as shown in Fig. 4.5. The transmission spectrum of the MZI structure contains an envelope curve and a cosine curve. In this work, the sensing characteristic of the envelope curve is not used or discussed. As the length increases, the period of the cosine curve gets smaller. According to the theory of MZ interference, the FSR can be calculated by the following equation.

$$FSR = \Delta\lambda = \frac{\lambda_1\lambda_2}{\Delta nL} \approx \frac{\lambda^2}{\Delta nL}. \qquad (4.1)$$

Where $\boldsymbol{\lambda}$ is the wavelength interference dip, $\boldsymbol{L}$ is the length of the TCSHF, and $\boldsymbol{\Delta n}$ is the difference in the ERI. Take 3 mm TCSHF as an example. The $\boldsymbol{FSR}$ is 1.86 nm, and the $\boldsymbol{\Delta n}$ can be calculated as 0.423 according to Eq. (4.1). Thus, one of the two light beams is involved in the MZI transmitting in the air hole, and the other is in the fiber core. This sensor is marked as Sensor 1 in the following discussion for convenience.

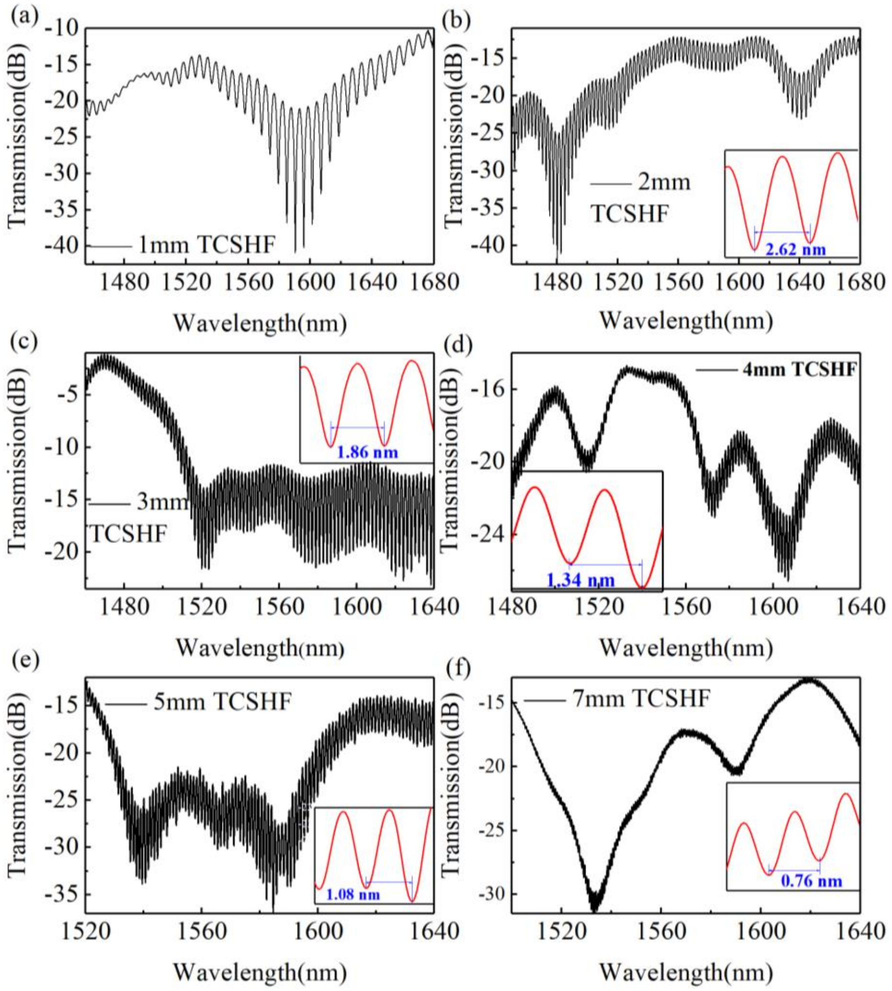

Fig. 4.5 The experimental transmission spectrums of the MZI structures under different lengths of TCSHF.

To figure out whether the length of NCF can influence the final spectrum, a comparative experiment is conducted by fabricating a new sensor with different fabrication parameters. The length of NCF and TCSHF in this sensor structure is 2 mm and 3 mm, respectively. The transmitted spectrum is shown in Fig.4 6 by the blue line, and the FSR of this sensor is ~1.86 nm. Thus, it can be inferred that the length of NCF does not influence the FSR of the MZI, and the FSR of the MZI is only determined by the length of TCSHF. Once again, it is demonstrated that the MZ interference only occurs in the TCSHF. Finally, taking the final size of the sensor and the complexity of preparation into account, the final length of the TCSHF is determined as 3 mm.

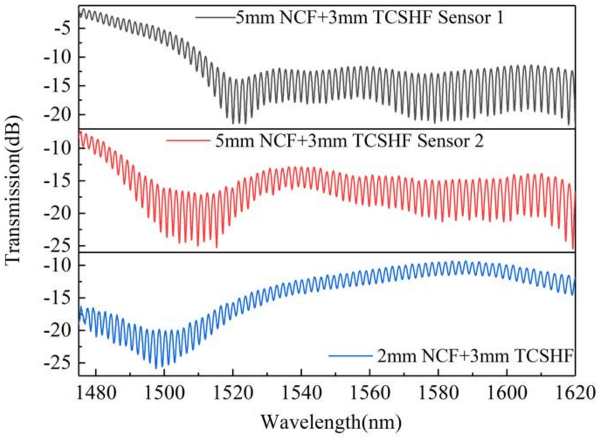

Fig. 4.6 The transmission spectrum of the MZI structure under different fabrication parameters.

Another sensor with the same fabrication parameters as Sensor 1 is fabricated to test the repeatability of the proposed TCSHF sensor and its spectrum is shown in Fig. 4.6 by a red line. This sensor is marked as Sensor 2, and the FSR is ~1.92 nm. The FSR difference between the two sensors is 0.08 nm, which is in the range of the errors permitted because the cutting precision of the optical fiber cleaver is 1 mm. Thus, the preparation repeatability of the proposed MZI sensor is quite good.

4.3 Sensing Principles

4.3.1 Mach-Zehnder interference

Concluded from the above analysis, the spectrum of the TCSHF sensor can be expressed as:

$$I = I_1 + I_2 + 2\sqrt{I_1 I_2}\cos\varphi \tag{4.2}$$

I_1 and I_2 are the light intensity of the beams in the core and air hole, respectively. The phase difference φ between the two light beams is related to the λ, Δn, and L.

$$\varphi = 2\pi\frac{\Delta nL}{\lambda}. \tag{4.3}$$

When the φ equals $(2m+1)\,\pi$, the intensity of the transmission light will reach the minimum value. Then the dip wavelength can be expressed as:

$$\lambda = \frac{2}{2m+1}\Delta nL. \tag{4.4}$$

If the sensor is used for temperature measurement, the relationship between λ and ΔT can be expressed as Eq. (4.5) based on the thermo-optic and thermal-expansion effects.

$$\frac{d\lambda}{dT}=\frac{2}{2m+1}\left(\Delta n\frac{dL}{dT}+\frac{d\Delta n}{dT}L\right). \tag{4.5}$$

As for axial strain measurement, Eq. (4.4) can be transformed into Eq. (4.6) according to the elastic-optical and tensile deformation effects.

$$\frac{d\lambda}{d\varepsilon}=\frac{2}{2m+1}\left(\Delta n\frac{dL}{d\varepsilon}+\frac{d\Delta n}{d\varepsilon}L\right). \tag{2.6}$$

4.3.2 Optical Vernier Effect

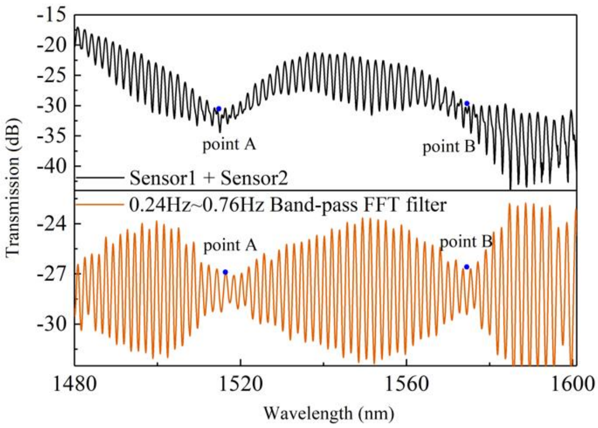

Fig. 4.7 The original transmission spectrum of the cascaded structure and the spectrum of it after the FFT filter.

The black line in Fig. 4.7 is the obtained spectrum after combining Sensors 1 and 2. There are two optical vernier points in the spectrum at the wavelength of ~1520 nm and ~1575 nm. However, this spectrum is not a typical spectrum of the OVE, which cannot be used for sensing applications. A bandpass FFT filter algorithm can be used to filter out useless frequency components to get a clear view of the Optical Vernier spectrum. The result is shown by the orange line in Fig. 4.7. The threshold of the FFT filter is 0.24 Hz~0.76 Hz because the spatial frequencies of the two MZIs are around 1/1.86 nm≈0.54 nm^{-1} (Hz). The FSR envelope curve read from the orange line is ~55 nm, marked as FSR_v. The theoretical value of FSR_v is related to the FSRs of the two single interferometers, which can be calculated by the following equation.

$$FSR_v = \frac{FSR_1 FSR_2}{\left|FSR_1 - FSR_2\right|} \tag{4.7}$$

After substituting 1.86 nm and 1.92 nm into Eq. (4.7), the theoretical value of FSR_v is obtained as 59.52 nm, which is close to the experimental value.

$$M = \frac{FSR_v}{FSR_1} = \frac{FSR_2}{\left|FSR_1 - FSR_2\right|}. \tag{4.8}$$

The magnification factor $\boldsymbol{M}$ of the cascaded structure compared to a single MZI can be calculated by Eq. (2.8). The theoretical value of $\boldsymbol{M}$ is 31.8.

4.4. Experiments based on the MZI structure

4.4.1 MZI for Temperature Sensing Experiment

Fig. 4.8 is the abridged general view of the temperature sensing system. The input light is provided by an ASE laser, and the output light is recorded by an MCF (AQ6070D, YOKOGAWA). The temperature change is controlled by a Thermo−Electric Cooler (TEC, TLTP−TEC0510, Wuhan Talent Century Technology Co., Ltd). The function of the acrylic plate in this system is to ensure an even temperature distribution around the sensor.

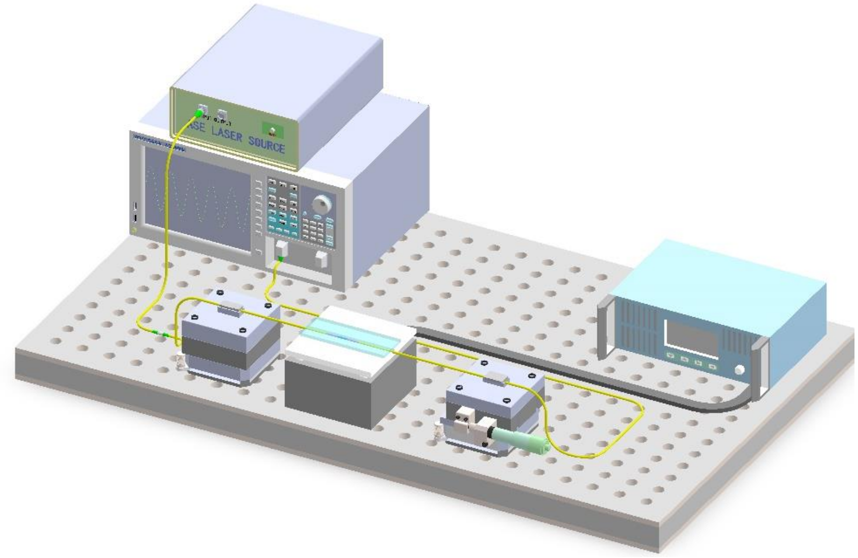

Fig. 4.8 The experiment system for temperature measurement.

Figure 4.9 (a) illustrates the spectra of Sensor 1 across various temperatures ranging from 30 ℃ to 65 ℃, with intervals of 5 ℃. The inset provides an enlarged view of the spectra around 1550 nm. Notably, as temperature increases, the spectrum of Sensor 1 consistently shifts towards longer wavelengths. This relationship is further depicted in Fig. 4.9 (b), where specific curves correlating temperature and dip wavelength are plotted. These curves are well-described by linear equations, with their slopes representing the sensitivity of dip wavelength to temperature change. The sensitivities of three selected dips are measured at 34.19 pm/°C, 34.19 pm/°C, and 33.14 pm/°C, respectively. Remarkably, these sensitivity values exhibit only marginal differences, indicating a uniform shift towards longer wavelengths across the entire spectrum of Sensor 1. Additionally, to confirm the repeatability of the proposed sensor, the temperature response of Sensor 2 is also evaluated, yielding a sensitivity of approximately 34 pm/°C.

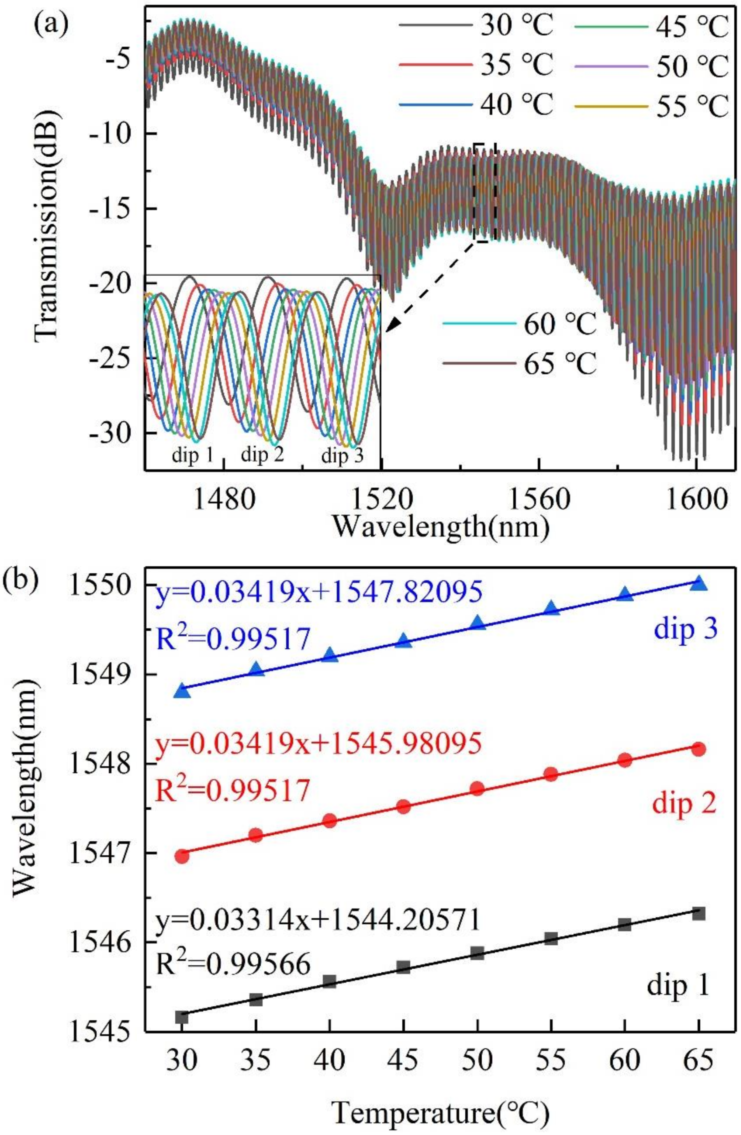

Fig. 4.9 (a) The spectrums of Sensor 1 at different temperatures, (b) The fitted curves of three dips between temperature change and dip wavelength shift

4.4.2 MZI for Axial Strain Sensing Experiment

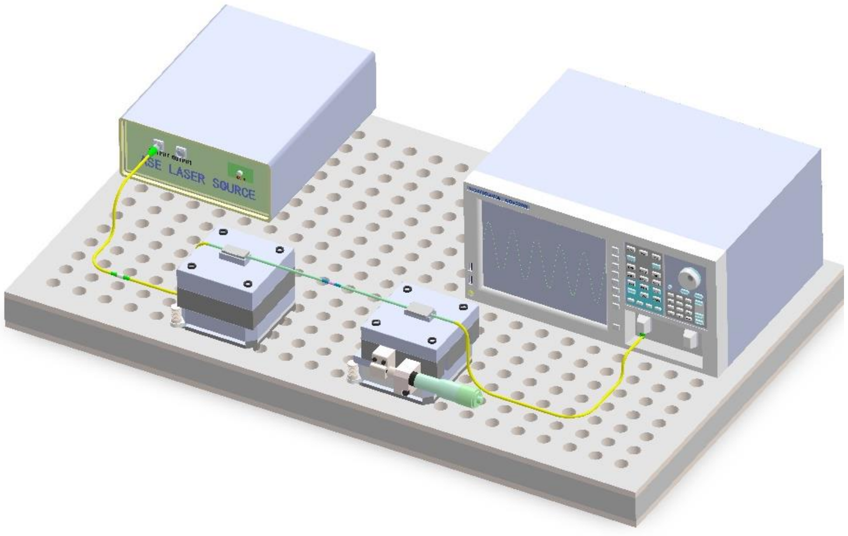

Fig. 4.10 The experiment system for axial strain measurement.

Identical to the temperature sensing experiment, the two ends of the Sensor 1 are fixed on the translation stages by fiber clamps as shown in Fig. 4.10. The resolution of the translation stages is 0.01 mm, and the distance between the two translation stages is 20 cm. Thus, the axial strain change step value can be calculated as: 0.01/20 cm=50 με. The spectrums of Sensor 1 under different axial strains in the range from 0 με to 1800 με are displayed in Fig. 4.11(a) with an interval of 200 με. From the illustration in Fig. 4.11(a), it can be easily observed that the dip wavelength shifts to the longer wavelength with the axial strain increasing.

The sensitivities of the Sensor 1 to axial strain change at the three chosen dips can be calculated out: 0.59 pm/με, 0.59 pm/με, and 0.62 pm/με as shown in Fig. 4.11(b). The values of sensitivities are close to each other, which indicates that the spectrum of Sensor 1 moves to the longer wavelength as a whole with the axial strain increasing. The axial strain sensitivities of Sensor 2 are also tested, which are all around 0.6 pm/με.

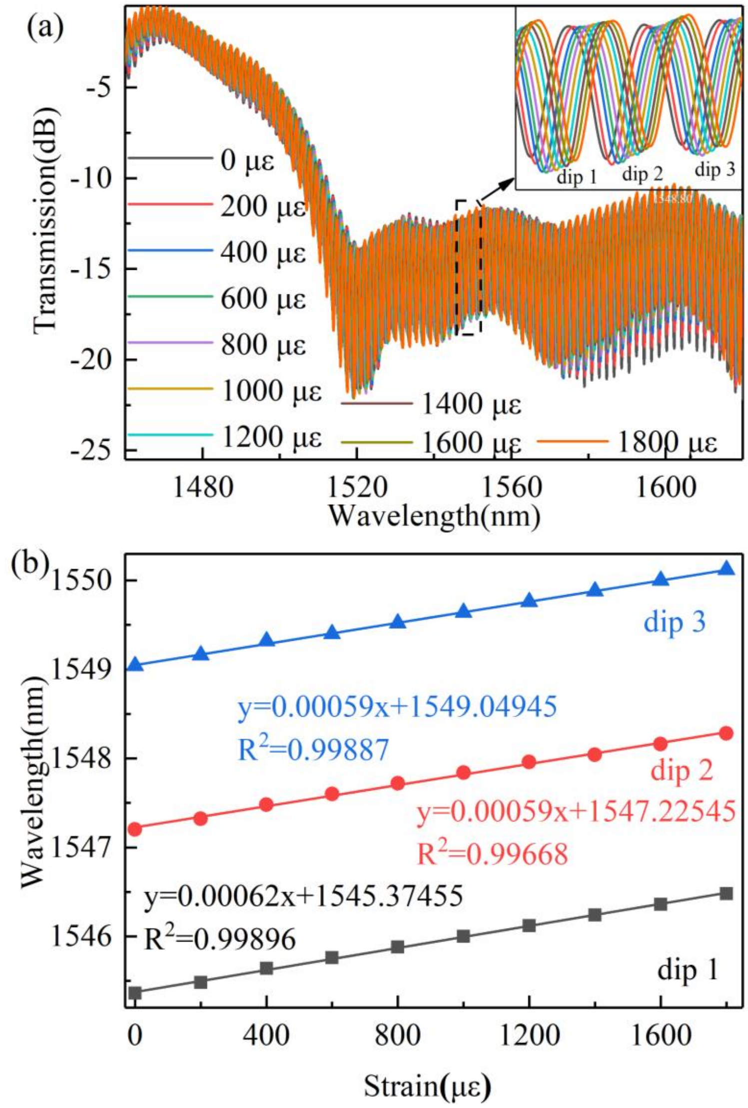

Fig. 4.11 (a) The spectrums of Sensor 1 under different axial strains, (b) The fitted curve between axial strain change and dip wavelength shift.

4.4.3 Comparison Between Different Structures of MZI

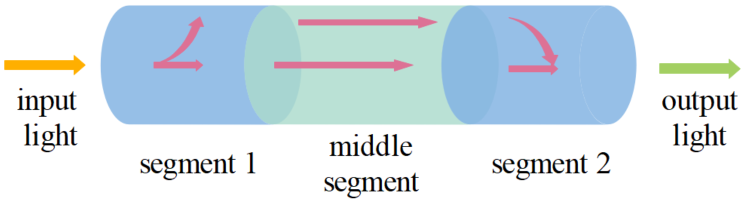

Fig. 4.12 The diagram of MZI with the sandwich structure.

Table III Comparison of the key parameters between the proposed sensor and the other types of MZI sensors

MZI structure	Strain sensitivity (pm/με)	Temperature sensitivity (pm/°C)	Ref.
MMF-TCF-MMF	-2.14	35.2	[76]
TCF-TF-TCF	-0.343	26.19	[77]
MMF-SCSHF-MMF	1.05	35.17	[78]
MMF-PCF-MMF	1.29	-	[79]
SMF-TCPCF-SMF	-0.31	6.68	[80]
NCF-HCF-NCF	0.652	30.92	[81]
NCF-TCSHF-NCF	0.6	34	This work

The sensors in Table III are all based on the symmetrical sandwich structure, as Fig. 4.12 shows. The function of the first and the last segments is like an optical coupler, which can enlarge or converge the mode field distribution. The middle segment can provide transmission paths for the MZ interference. As shown in the Table, the axial strain sensitivities of this sensor structure are generally lower than 2.5 pm/με, and the temperature sensitivities are less than 35 pm/°C. Though the preparation cost of this type of sensor structure is not very high, it is not practical in many measurement fields due to its low sensitivity.

4.5 Experiments Based on Cascaded MZI Structure

It is noted that the fabrication repeatability of the proposed sensor is quite good compared with other structures. Benefitting from this, a cascaded structure based on the OVE is designed and tested to improve the practicability and performance of the proposed sensor. In this paper, Sensor 1 and Sensor 2 are combined to realize the Optical Vinier Effect because of the slight difference between their FSRs. The characteristics of the structure spectrum have been discussed in Chapter 4.3.2.

4.5.1 Cascaded MZIs for Temperature Sensing Experiment

As shown in Fig. 4.13, Sensor 1 is horizontally placed on the TEC heater, and Sensor 2 is fixed between two translation stages.

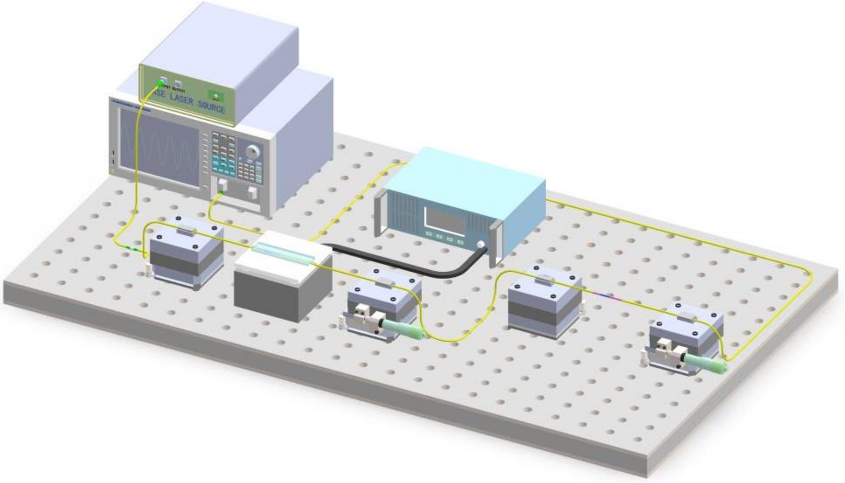

Fig. 4.13 The experiment system is designed for cascaded MZI structures.

In the experiment of temperature sensing, Sensor 1 is the sensing element, while Sensor 2 serves as the reference element. The spectrums of the cascaded structure in different environmental temperatures are shown in Fig. 4.14 (a) with a step of 5 ℃ in the range from 30 ℃ to 70 ℃. The vernier points around 1460 nm,1520 nm, and 1580 nm are marked as points A, B, and C, respectively. It can be observed that the marked points show a redshift when the temperature increases. Limited by the bandwidth of the light source, point A or point C cannot be captured when the environmental temperature is lower than 40 ℃ or higher than 50 ℃. Fig. 4.14 (b) is the fitting curve of the relationship between temperature and the wavelength of gauge points. The fitted degrees are all above 0.99, which indicates that the spectrum of cascaded structures can respond linearly to temperature change.

The sensitivities are 0.76 nm/°C at point A, 1.167 nm/°C at point B, and 1.588 nm/°C at point C.

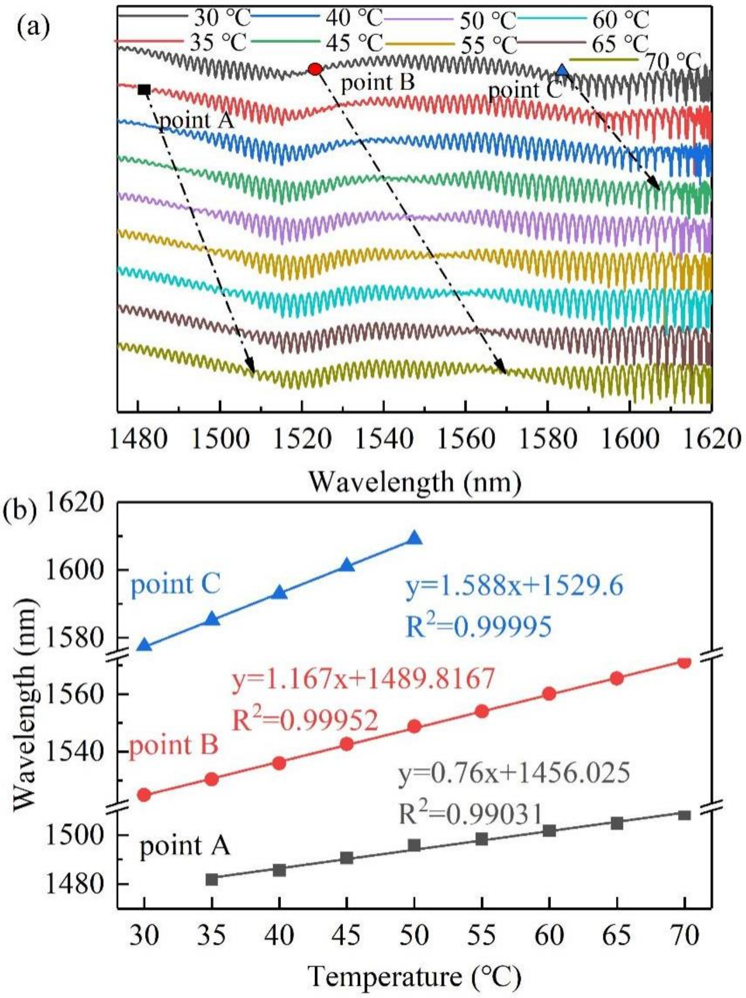

Fig. 4.14 (a)The spectrums of cascaded structure at different temperatures, (b) The fitted curve between temperature change and point wavelength.

Compared to a single MZI's sensitivity, the cascaded structure's sensitivity is much higher. The magnification factor M can be calculated as 1167/34≈34, which is in accord with the theoretical analysis in Chapter 4.3.

4.5.2 Cascaded MZIs for Axial Strain Sensing Experiment

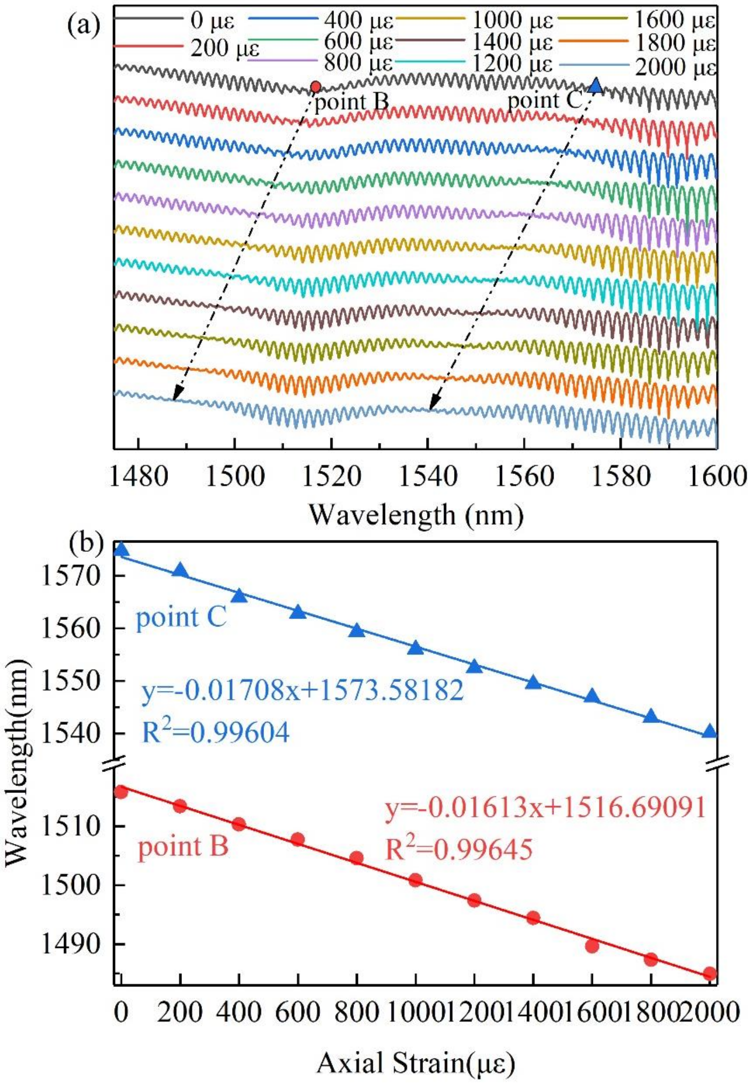

Fig. 4.15 (a)The spectrums of the cascaded structure under different axial strains, (b) The fitted curve between axial strain change and point wavelength shift.

The axial strain measurement experiment is also conducted by the system displayed in Fig. 4.13. The only difference is that Sensor 2 serves as the sensing element while Sensor 1 serves as the reference element. According to the result shown in Fig. 4.15 (a), the maximum range of axial strain measurement is 2000 με.

The point B and C shift to the shorter wavelength with the axial strain increasing. From the slopes and the fitted degree of the curves in Fig. 4.15 (b), it can be concluded that the cascaded structure responds linearly to the axial strain fluctuation with sensitivities of -16.13 pm/με at point B and -17.08 pm/με at point A. The magnification factor M can also be calculated by 17.08/0.6≈28, which verifies the analysis result in Chapter 4.3.

4.5.3 Cascaded MZIs for simultaneous measurement of axial strain and temperature

Since the spectrum of the cascaded structure can separately respond linearly to the temperature or axial strain variation, the spectrum can also shift linearly if the temperature or axial strain changes simultaneously. In this case, points B and C are chosen as the monitoring points. Then, the wavelength offset value can be calculated by the following equation.

$$\begin{cases}\Delta\lambda_B = S_B^{\varepsilon}\Delta\varepsilon + S_B^{T}\Delta T \\ \Delta\lambda_C = S_C^{\varepsilon}\Delta\varepsilon + S_C^{T}\Delta T\end{cases}. \tag{4.9}$$

Where the $\boldsymbol{S^{\varepsilon}}$ and $\boldsymbol{S^{T}}$ are the strain and temperature sensitivities, $\boldsymbol{\Delta\lambda}$ is the value of the wavelength drift. $\boldsymbol{\Delta\varepsilon}$ and $\boldsymbol{\Delta T}$ are the values of the temperature and axial strain change, respectively. Eq. (4.9) can be transformed into the matrix form as follows:

$$\begin{bmatrix} \Delta\lambda_B \\ \Delta\lambda_C \end{bmatrix} = \begin{bmatrix} S_B^{\varepsilon} & S_B^{T} \\ S_C^{\varepsilon} & S_B^{T} \end{bmatrix} \begin{bmatrix} \Delta\varepsilon \\ \Delta T \end{bmatrix}. \tag{4.10}$$

Then, the temperature and axial strain change value can be deduced according to the regulation of matrix operation.

$$\begin{bmatrix} \Delta\varepsilon \\ \Delta T \end{bmatrix} = \begin{bmatrix} S_B^{\varepsilon} & S_B^{T} \\ S_C^{\varepsilon} & S_B^{T} \end{bmatrix}^{-1} \begin{bmatrix} \Delta\lambda_B \\ \Delta\lambda_C \end{bmatrix}. \tag{4.11}$$

The resolution of the OSA used in this work is 0.1 nm. Thus, the theoretical error range of the $\boldsymbol{\Delta\varepsilon}$ and $\boldsymbol{\Delta T}$ can be calculated by Eq. (4.11), which are ±7.4 με and ±0.017 °C.

Based on the above discussion result, the dual-parameter measurement is conducted by the system displayed in Fig. 4.13. In this experiment, Sensor 1 serves as the temperature-sensing element while Sensor 2 serves as the strain-sensing element, separately. The original external temperature around Sensor 1 is 30 °C, and the original axial strain added on Sensor 2 is 0 με. The first step is changing the original axial strain added on Sensor 1 from 0 με to 1000 με. The second step is increasing the external temperature around Sensor 2 from 30 °C to 42 °C with a step value of 2 °C. The spectrums under different states during the experiment process are shown in Fig. 4.16 (a).

The blue points in Fig. 4.16 (b) are the actual calculated values of every experimental state, and the red points are the truth values.

Unfortunately, all experimental values are out of the permitted error range calculated by Eq. (4.11). The major error sources are the sensor itself and the experiment system. For the experiment system in this work, the resolutions of the translation stage and the TEC are the most error parameters for dual-parameter measurement because the wavelength drift value should be the multiple of the OSA resolution then the results will be more accurate. However, it is impossible to achieve such high resolution in the laboratory. The error from the sensor itself is related to the linearity of the sensor response, which can be deduced by improving the fabrication process. The proposed sensor can work well if the permitted error range of the $\boldsymbol{\Delta\varepsilon}$ and $\boldsymbol{\Delta T}$ are extended to ±40 με and ±0. 5 °C as areas shown in Fig. 4.16 (b). Thus, the proposed sensor can be used for roughly measuring axial strain and temperature simultaneously.

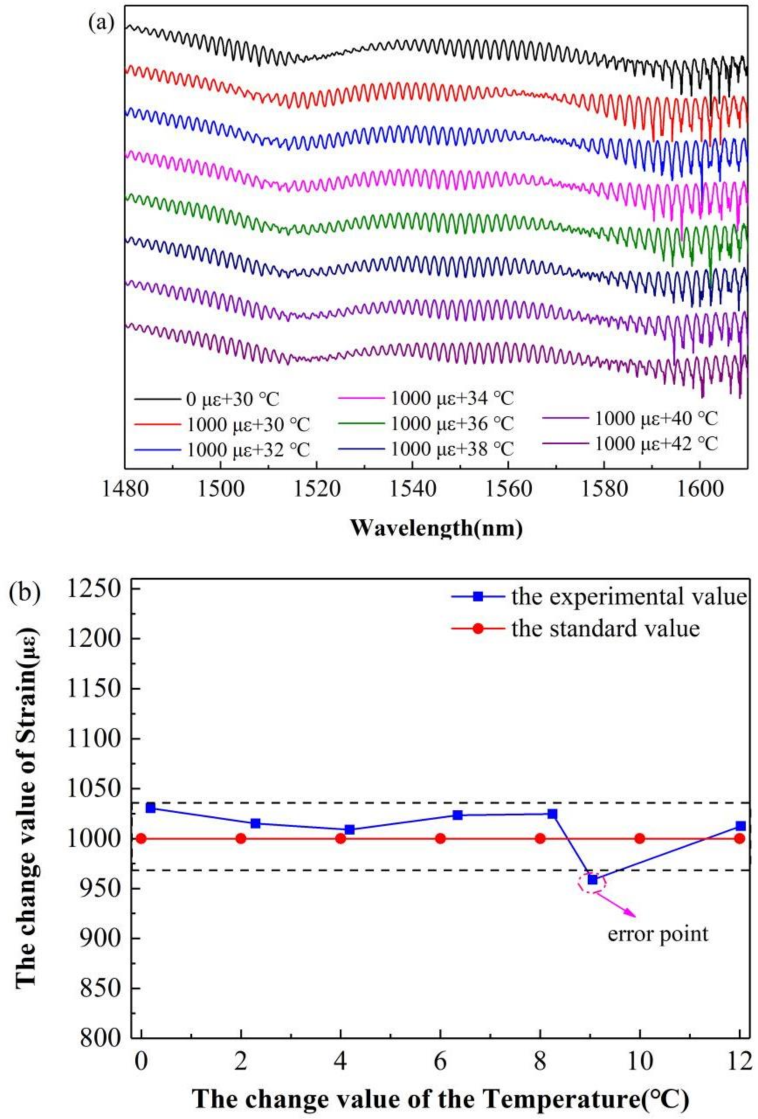

Fig. 4.16 (a)The spectrums of the cascaded structure under different axial strains and temperature, (b) The experimental values and the truth values for the dual parameter sensing experiment.

4.5.4 Comparison with Other Sensors based on the Optical Vernier Effect

Table IV presents a summary of sensitivities for various sensor configurations based on the Optical Vector Analysis (OVE) technique. The proposed sensor exhibits higher sensitivities compared to others and offers the capability to simultaneously measure axial strain and temperature within acceptable error limits.

Table IV Comparison with other sensors' sensing performance

Sensor structure	Strain Sensitivity (pm/με)	Temperature Sensitivity (pm/°C)	Dual-Parameter sensing	Ref.
FPIs	28.11	278.48	-	[82]
SIs	58	-1050	-	[83]
FPI+MZI	-	-107.2		[84]
MIs	-	143	-	[85]
HCF+SMF	18.36	-	-	[86]
FPI+HCF	-43.2	-27	-	[87]
MZIs	17.08	1167	Yes	This work

Notably, the fabrication process for this sensor is relatively straightforward, involving only splicing fusion operations. Furthermore, the sensor demonstrates robustness, aided by the uniform diameter of all fibers used (125 μm), which also simplifies encapsulation challenges. Consequently, the designed sensor holds significant potential across numerous application domains. For instance, it could be instrumental in extensive building health monitoring within engineering contexts, as well as in vital sign detection within the medical field, and other applications.

4.6 Summary

This work proposes a sensor based on the OVE for the dual-parameter measurement of temperature and axial strain. The main structure of the sensor is built up of two MZIs based on the symmetrical sandwich structure with similar structural parameters. The structure parameters are obtained from simulation experiments and the variable-controlled experiment. The splicing fusion parameters are also listed in detail, obtained from repeated experiments. In the experiment part, the sensing performance of the MZI is studied first. Each MZI can respond linearly to the axial strain change with a sensitivity of ~ 0.6 pm/με and temperature sensitivity of ~34 pm/°C. The sensitivities at this level are not competitive. Thus, two MZIs are combined to simplify the sensitivities about 34 times according to the OVE principles. The proposed sensor has many other advantages, such as being fabricated easily, low cost, good robustness, and so on.

However, many downsides of the proposed sensor are also required to be investigated. For example, the accuracy of dual-parameter measurement should be improved. Besides, a simple interrogation system to process the response data of the sensor is an urgent need because it would help put the experimental results into the existing application system.

Chapter 5 An Ultrasensitive Inline Dual Fabry-Perot Gas Pressure Sensor Based on Single-core Side-hole Fiber with Optical Vernier Effect

Due to the complexity of the inline MZI structure, cascading MZIs in series is the best choice for amplifying the sensitivity, which will increase the system instability. Also, the MZI is working based on the transmitted light, which is inconvenient for some specific application scenarios. Such as sensing work in narrow places, remote places, and confined spaces. In those cases, the sensors working based on the reflected lights can exploit the advantages to the full. Generally speaking, the fundamental sensor structures working based on the reflected lights are FPI and MI.

In this chapter, an ultrasensitive inline dual FPI sensor based on Single-core Side-hole Fiber is proposed for gas pressure measurement in confined spaces.

5.1 Introduction

The gas pressure sensor is an essential element in many measurement systems. For example, in the aerospace area, the gas pressure sensor on the carrier rocket body can help monitor the health condition of the rocket’s critical components [88]. In the ocean exploration area, gas pressure sensors can help test the oceanic environment [89]. In the defense and military area, the gas pressure sensor in the weapon system can collect battlefield information in real-time, which can help the man-at-arms adjust their battle plans in time [90]. In the industrial production area, the gas pressure sensor in the assembly line can help directly measure the parameters related to the product quality index [91]. In the biomedical area, the gas pressure sensor can help monitor the patient’s body condition as the core component of many medical testing instruments [92].

Compared to traditional electrical gas pressure sensors, optical gas pressure sensors are more widely used for their advantages of anti-electromagnetic interference, fast response speed, and so on [93-96]. Typically, widespread attention has been drawn to the sensors based on optical fibers due to their unique characteristics such as compact size, high sensitivity, strong remote sensing capability, etc. [97-99]. Over the past few years, a massive number of structures have been designed and experimentally demonstrated. In 2015, Tang induced an LPFG in the air-core photonic bandgap fiber for gas pressure measurement, of which the sensitivity is about -13.7 nm/MPa [100]. In 2017, an FBG-based gas pressure sensor presented by Liang exhibited a sensitivity of nm/MPa [101]. In comparison to the grating-based gas pressure sensors with relatively low sensitivities, sensors based on interferometry such as FPI, MZI, and SI manifest a better performance with the sensitivities varying from -5.8 pm/MPa [103] to 98 nm/Mpa [103], depending on the structure and materials used. In most cases, however, the sensitivities are below 1 nm/MPa, which severely inhibits the potential practical applications.

As discussed before, an effective way for optical fiber sensors to improve sensitivity is by adopting OVE [104]. Up to now, many optical fiber sensors based on the OVE have been proposed for gas pressure measurement. In 2018, two integrated parallel MZIs based on the dual side-hole fiber were demonstrated by Lin with a sensitivity of ~60 nm/Pa in 0~0.8 MPa [105]. Similarly, Zhao designed a cascaded MZIs gas pressure sensor based on a length of open cavity HCF sandwiched in between two pieces of MMF in 2019 [106]. This type of MZI-based sensor relying on the transmission mode is of lower practicability than the probe sensor in the narrow place. The FPI structure can effectively solve this problem. In 2018, P. Chen *et al.* fabricated a capillary glass tube to detect the gas pressure change in the range of 0~0.6 MPa with a sensitivity of 86.64 nm/MPa [107]. In 2019, Li designed a gas pressure FPI probe with a sensitivity of 80.3 nm/Mpa [108] using a side-opened hollow silica tube. However, the fabrication process of the above structures is very complex because it not only needs fusion splicing operation but also uses a femtosecond laser to drill open one air hole.

In this chapter, the SCSHF is employed for fabricating a gas pressure sensor composed of two parallel FPIs based on the OVE. Similar to the sandwich structure, a length of ~1 mm SCSHF is fusion splicing between the NCF and the HCF. The HCF acts as the gas channel to connect the air hole in the SCSHF with the external environment, avoiding drilling an air hole. The experimental results show that the proposed sensor has a sensitivity of 183 nm/MPa in 0~100 kPa. This sensor is also sensitive to temperature change with a sensitivity of 440 pm/°C. Then, the temperature cross-sensitivity can be calculated as -2.4 kPa/ °C, which is relatively low. The sensor’s gas pressure sensing repeatability is quite good, verified by repetitive experiments. In addition, since the proposed sensor works based on the reflective mode, it can be used in narrow places or places difficult for transmissive mode sensors to reach. Thus, the proposed sensor has an excellent outlook for sensing areas requiring high sensitivity, a simple fabrication process, and long-term stability.

5.2 Sensor Structure and Fabrication Process

5.2.1 Single-core and single-hole fiber

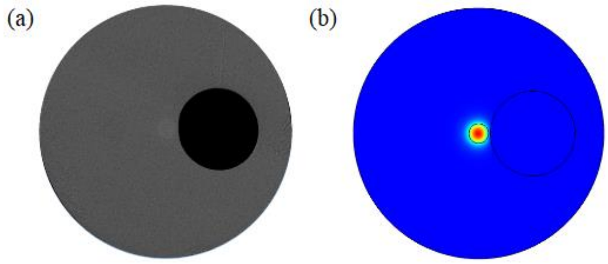

Fig. 5.1 (a) The cross-section of the SCSHF, (b) The fundamental core mode of the SCSHF simulated by the software.

As the main sensing element, the cross-section of the SCSHF can be seen clearly in Fig. 5.1(a). Its diameter is 125 µm, the same as the standard SMF. The diameters of the core and the air hole are ~9.8 µm and ~21 µm, respectively. The ERI of the core's material is 1.4494@1550nm, and the RI of the cladding material is 1.444@1550nm. A simulation experiment was conducted to understand the optical characteristics of the SCSHF, and the result is shown in Fig. 5.1(b). Like the common SMF, the fundamental mode of SCSHF only exists in the fiber core. Influenced by the big air hole, the mode center does not overlap with the core center. The effective RI of the fundamental mode is 1.4468.

Based on the gas pressure sensing command, a short length of NCF is used to enlarge the mode field. This enables a part of the light to be coupled into the air hole. The diameter of the NCF is also 125 μm, and the fiber material is isotropic with an RI of 1.4575@630nm.

The HCF is the gas channel connecting the air hole and the external environment. Thus, the inner diameter of the HCF must be larger than that of the core to ensure the outside air can access the air hole of the SCSHF. In this work, the inner diameter of the HCF is 15 μm.

5.2.2 Fabrication Process and Parameters

Fig. 5.2 shows the diagrammatic drawing of the fabrication process of proposed gas pressure. The fabrication process of this sensor is straightforward, only involving the fusion splicing operation.

The first step is fusion splicing the SMF with the NCF using the Auto Mode of the fiber fusion splicer and then cutting off the NCF well at ~1 mm. The length of NCF is determined based on our previous work to ensure a well-proportioned light field distribution at the fusion splicing point between the NCF and the SCSHF.

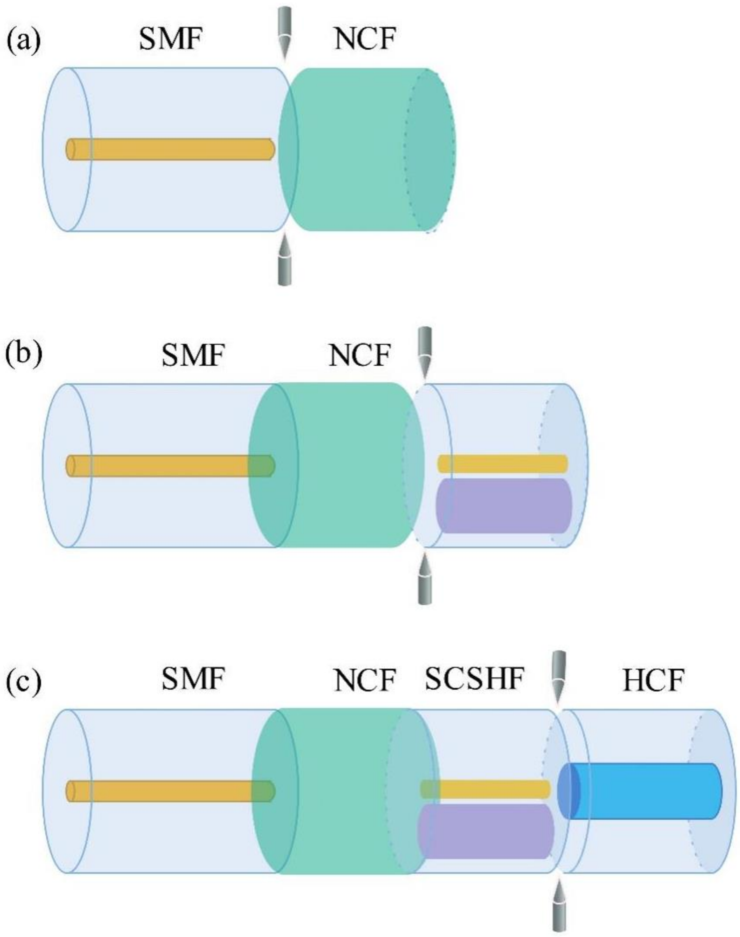

Fig. 5.2 The structure of the proposed gas pressure sensor.

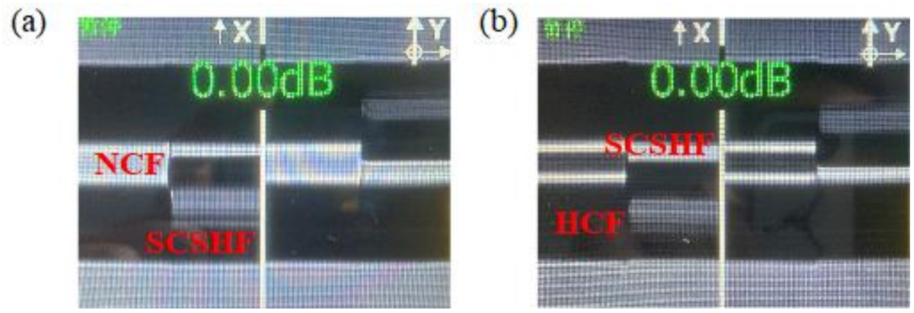

Fig. 5.3 (a) The final fusion splicing result between NCF and SCSHF, (b) The final fusion splicing result between HCF and SCSHF.

The second step is fusion splicing the NCF with the SCSHF using the user-defined mode. Since the air hole will result in a collapse during the fusion splicing process, the fusion splicing parameters are carefully selected by numerous attempts, which are the same as in Table II shown in Chapter 4. The final fusion splicing result is shown in Fig. 5.3 (a). The boundary between the NCF and the SCSHF is clear and there is no collapse at the fusion splicing point.

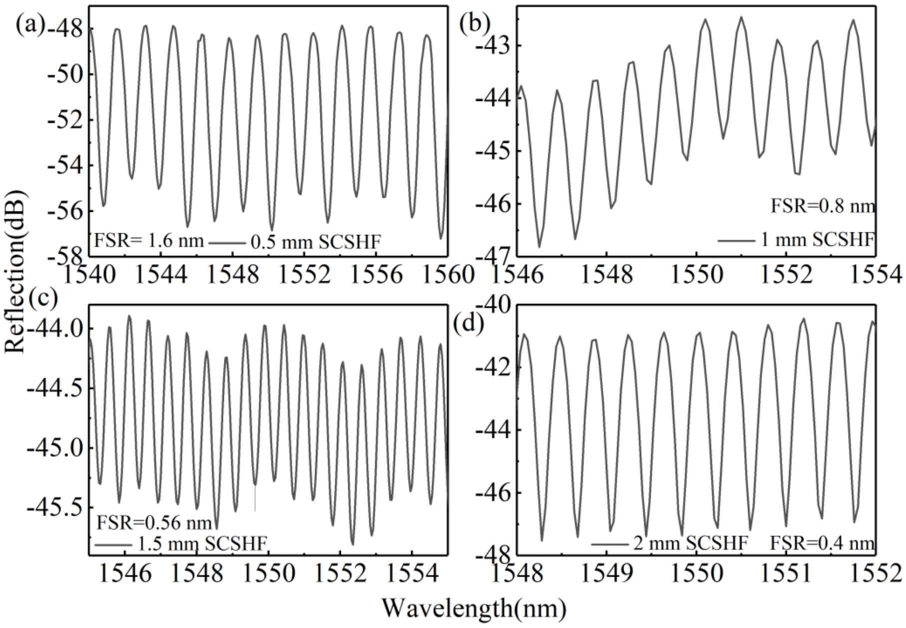

Fig. 5.4 The spectrums of SMF-NCF-SCSHF structure under different lengths of SCSHF.

Then the SCSHF is cleaved well to prepare for the following fusion splicing with the HCF. The spectrums of different lengths of SCSHF after this step are recorded and shown in Fig. 5.4. The waveform of the obtained spectrums is a typical cosine function curve and the FSR changes linearly with the increasing SCSHF length. This indicates there is a two-beam interference occurring in the SCSHF. Taking the 1 mm SCSHF as an example, the ERI difference Δn between the two involved lights can be calculated by $\Delta n=\lambda^2/(2*L*FSR)\approx 1.5016$. The value is close to the ERI (1.4468 obtained by the simulation) of the fundamental mode. That is, one of the two involved lights is transmitted in the core SCSHF and reflected by the cut-end of SCSHF. The other one is the light transmitted in the NCF and reflected by the boundary between the NCF and the air hole in SCSHF.

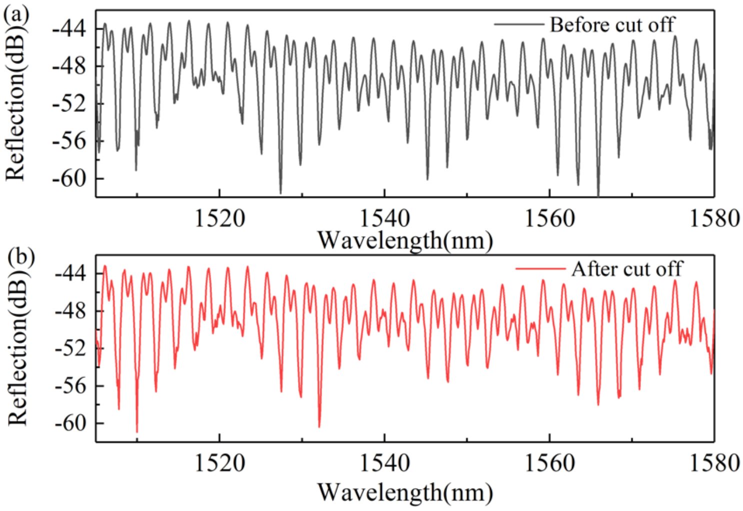

Fig. 5.5 (a) The spectrum of SMF-NCF-SCSHF-HCF structure before cutting off the HCF, (b) The spectrum of SMF-NCF-SCSHF-HCF structure after cutting off the HCF.

The third step is fusion splicing the SCSHF with the HCF. The fusion splicing mode and parameters are the same as in the second step. The fusion splicing result is shown in Fig. 5.3 (b). The boundary between the HCF and the SCSHF is clear and there is no collapse at the fusion splicing point. Thus, the interface between the air hole and the HCF can also reflect the light. The spectrum after this step is shown in Fig. 5.5 (a) by a black line, which is a typical spectrum based on the OVE. To avoid light reflection at the end of HCF, a rough surface of the HCF end is fabricated by cutting the fiber at the length of ~2 mm with a razor blade. As shown in Fig. 5.5 (b), the final spectrum has almost no change compared with the spectrum before cutting off.

5.3 Spectrum Analysis

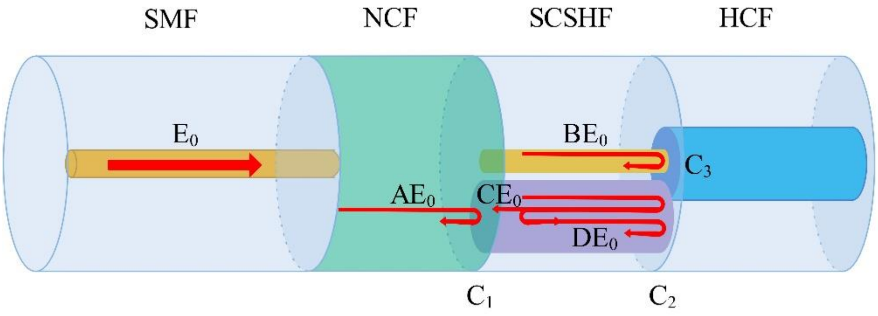

Fig. 5.6 The schematic diagram of optical transmission in the sensor structure.

According to the analysis in Chapter 5.2, there are three reflectors C_1, C_2, and C_3 in the sensor structure as shown in Fig. 5.6. If the incident electric field is set as E_0, the whole reflected electric field E_r can be expressed as [109]:

$$E_r = AE_0 + BE_0 \exp^{-i\varphi_1} + CE_0 \exp^{-i\varphi_2} + DE_0 \exp^{-i(2*\varphi_2)} \quad (5.1)$$

Where AE_0, BE_0, and CE_0 are the electric field reflected by the reflectors C_1, C_2, and C_3. DE_0 is the secondary electric field reflected by the HCF in the side air hole. $\boldsymbol{\varphi_1}$ and $\boldsymbol{\varphi_2}$ are the phase differences introduced by the SCSHF, which are related to the length of the SCSHF $\boldsymbol{L}$ and the effective RI of the core $\boldsymbol{n_1}$ and the air $\boldsymbol{n_2}$.

$$\varphi_1 = \frac{4\pi n_1 L}{\lambda}, \quad \varphi_2 = \frac{4\pi n_2 L}{\lambda} \tag{5.2}$$

Then, the reflected light intensity can be expressed by the following equation.

$$\begin{aligned} I_r &= |E_r||E_r|^* \\ &= E_0^2 \begin{bmatrix} A^2 + B^2 + C^2 + D^2 \\ 2AB\cos(\varphi_1) + 2(AC + CD)\cos(\varphi_2) + 2AD\cos(2\varphi_2) + \\ 2BC\cos(\varphi_2 - \varphi_1) + 2BD\cos(2\varphi_2 - \varphi_1) \end{bmatrix} \end{aligned} \tag{5.3}$$

From Eq. (5.3), the final output spectrum is the superimposition of five cosine function modulated spectrums, which are the interference result of reflected light from different reflectors. The two exact reflected lights that participate in every interferometer can be told by the two coefficients before every cosine function.

Thus, the FSR of the five interferometers can be calculated by the following equations.

$$\begin{cases} FSR_1 \approx \dfrac{\lambda^2}{2n_1L}, FSR_2 \approx \dfrac{\lambda^2}{2n_2L}, FSR_3 \approx \dfrac{\lambda^2}{4n_2L}, \\ FSR_4 \approx \dfrac{\lambda^2}{2(n_1-n_2)L}, FSR_5 \approx \dfrac{\lambda^2}{2(2n_2-n_1)L} \end{cases} \tag{5.4}$$

For the proposed sensor, $\boldsymbol{L}$≈1 mm, $\boldsymbol{n_1}$ ≈1.4494, $\boldsymbol{n_2}$=1 and $\boldsymbol{\lambda}$=1550 nm. Then, it can be obtained that $\boldsymbol{FSR_1}$≈0.83 nm, $\boldsymbol{FSR_2}$≈1.2 nm, $\boldsymbol{FSR_3}$≈0.6 nm, $\boldsymbol{FSR_4}$≈2.67 nm, and $\boldsymbol{FSR_5}$≈2.18 nm.

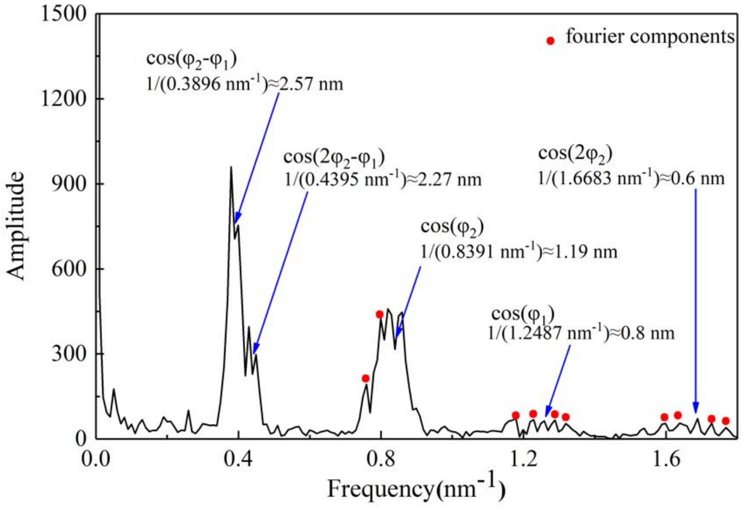

Fig. 5.7 The FFT result of the final spectrum.

Every FSR corresponds to a frequency peak in the MCF consequence if the spectrum is regarded as a normal curve [25]. As shown in Fig. 5.7, the specific frequency peaks could be obtained by taking the FFT on the final spectrum in the wavelength domain. For example, if the spatial frequency of the first peak is ~0.3896 nm^{-1}, then the ***FSR*** of this frequency can be calculated as 1/(0.3896 nm^{-1})≈2.57 nm. This value is very close to the $\boldsymbol{FSR_4}$, meaning that the corresponding interferometer indeed exists in the proposed sensor structure. Marked by the blue arrows, the spatial frequency of the other four interferometers can also be found. The peaks marked by the red points are frequency-doubling components introduced by the FFT algorithm itself [110].

The amplitude of the first two interferometers is larger than the others, meaning that their interference effect is more obvious than others. Their FSRs are close to each other, satisfying the requirement of raising the OVE. In addition, for both aforementioned interferometers, one of the two lights involved in the interference is transmitted in the air hole of SCSHF, which is a necessary condition for gas pressure sensing. Thus, in the following experiment part, only the first two interferometers are considered and discussed while the rest three are all ignored.

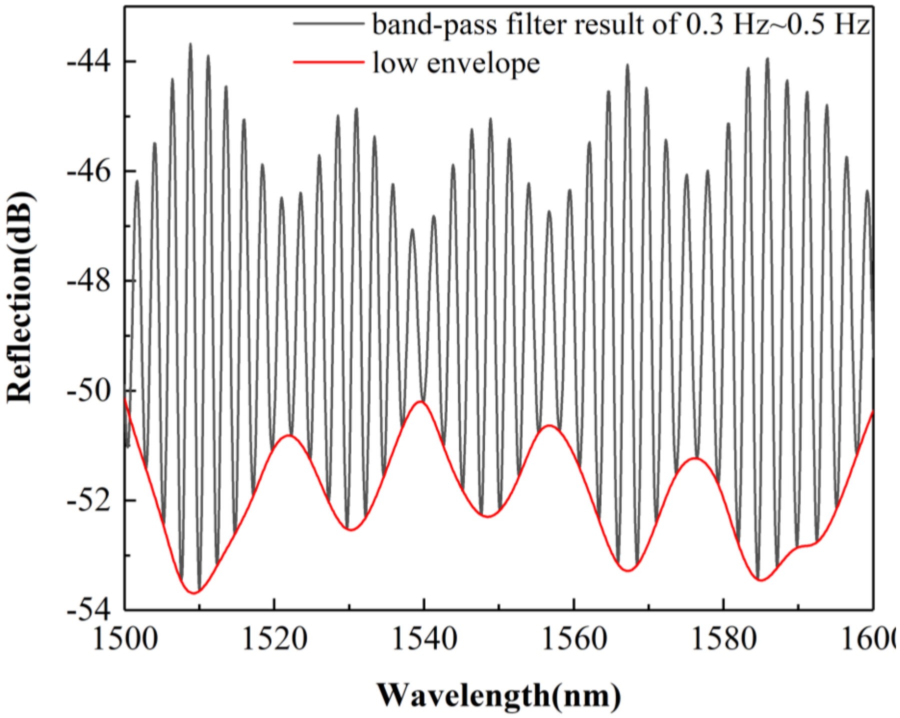

Fig. 5.8 The result of a 0.3~0.5 nm^{-1} band-pass filter.

To get the final spectrum of the two chosen interferometers, a band-pass filter of 0.3~0.5 nm^{-1} is used on the original spectrum, and the result is shown in Fig. 5.8. Obviously, the obtained spectrum is much simpler than the original one to a great extent, reducing the difficulty of subsequent data processing process. The red line in Fig. 5.8 is the low envelope of the obtained spectrum. Usually, the peaks of the fitting envelope curve are chosen as the observation points in the sensing experiments for convenience. Its FSR is ~17 nm. The theoretical $\boldsymbol{FSR_v}$ of the fitting envelope in this work can be expressed as:

$$FSR_v = \frac{FSR_4 \bullet FSR_5}{\left|FSR_4 - FSR_5\right|} = \frac{\lambda^2}{2(3n_2 - 2n_1)L} \approx 15nm \qquad (5.5)$$

From Eq. (5.5), it can be inferred that the ***FSRv*** is only related to the length of SCSHF. The experimental value of ***FSRv*** is close to the theoretical one, demonstrating the correctness of the experiment.

Then the peak wavelength of the fitting envelope can be expressed as:

$$\lambda = \frac{2(3n_2 - 2n_1)L}{m}, m = 1, 2, 3...... \qquad (5.6)$$

5.4 Experiments

In this chapter, the air hole in the SCSHF is used as the sensing element to detect gas pressure and temperature fluctuation because the peak wavelength of the fitting envelope is determined by the RI of the air hole according to Eq. (5.6), which is related to the gas pressure and temperature as Eq. (5.7) shows [108]. That is, the gas pressure and temperature fluctuation will result in the peak wavelength shift of the fitting envelope.

$$n_2 = 1 + \frac{2.8793 \times 10^{-9} \times P}{1 + 0.003671 \times T} \qquad (5.7)$$

5.4.1 Gas Pressure Sensing Experiment

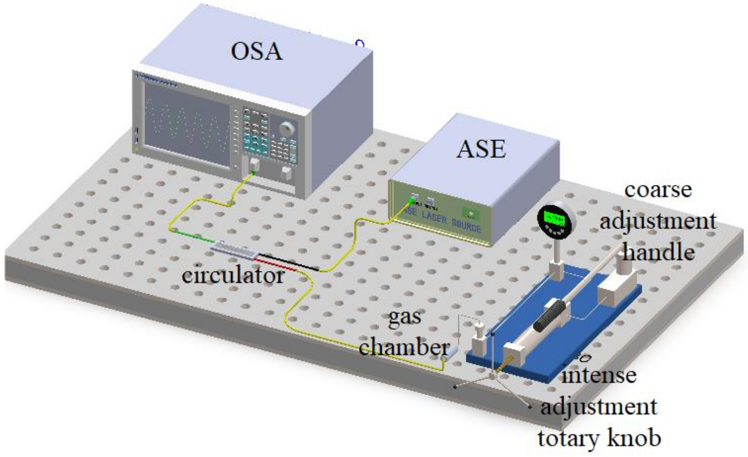

Fig. 5.9 The experiment system for gas pressure measurement.

For the gas pressure measurement, the sensitivity S_P can be calculated by taking the derivative of Eq. (5.6):

$$S_P = \frac{d\lambda}{dP} = \frac{\partial\lambda}{\partial n_2}\frac{\partial n_2}{\partial P} = \frac{2.8793\times10^{-9}}{1+0.003671\times T}\frac{6L}{m} \tag{5.8}$$

Next, by substituting Eq. (5.6) into Eq. (5.8) again, the S_P can be calculated as

$$S_P = \frac{2.8793\times10^{-9}}{1+0.003671\times T}\frac{3\lambda}{3n_2-2n_1} \tag{5.9}$$

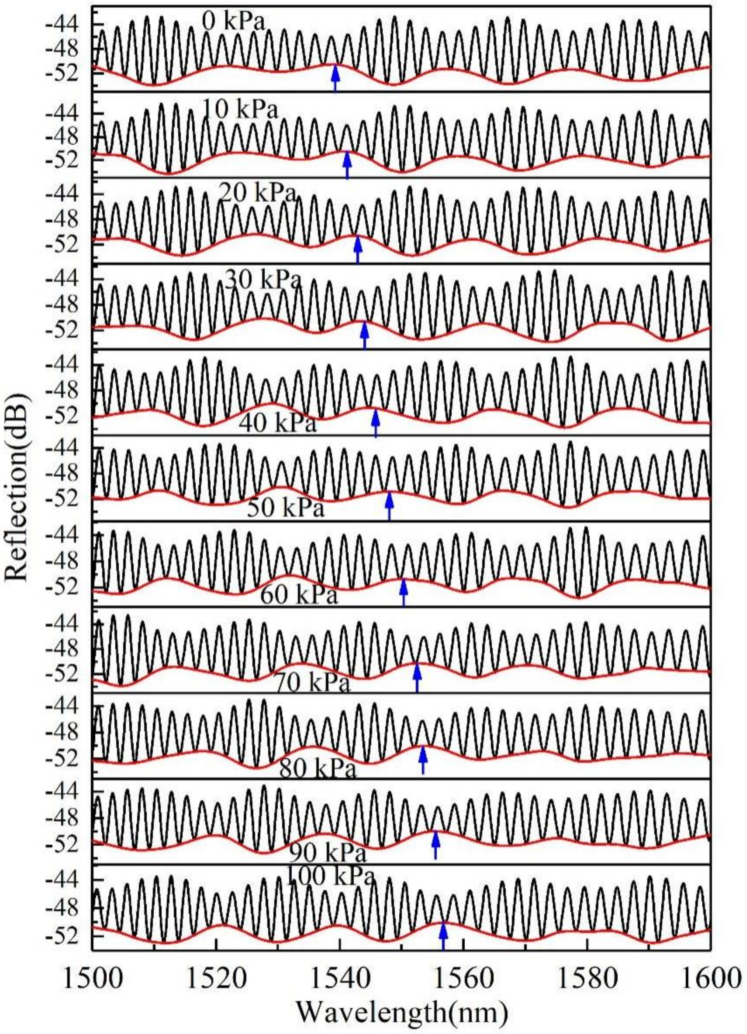

Fig. 5.10 The spectrums of the proposed sensor under different gas pressures.

Then, the theoretical S_P can be calculated to be ~123 nm/MPa at the wavelength 1550 nm of the peak traced under room temperature (20 °C).

As shown in Fig. 5.9, the proposed sensor is placed into a gas chamber with a resolution of 10 kPa. The incident light is emitted by an Amplified Spontaneous Emission (ASE) source. After transmitting through a circulator, the incident light will arrive at the sensor structure. Then, the reflected light will go through the circulator again and finally be recorded by a spectrograph (AQ6070D, YOKOGAWA).

After being filtered by the FFT filter, the spectrum of the proposed sensor under different gas pressures is shown in Fig. 5.10. The red lines are the low envelope of the spectrum under the peak fitting algorithm. The spectrum shifts to the long wavelength monolithically with the air pressure increasing.

With a step of 10 kPa, Fig. 5.11 displays the linear fitting curve between the peak wavelength around 1540 nm and the gas pressure in the range of 0~100 kPa. The fit index R^2 is close to 1, indicating that the proposed sensor responds linearly to the gas pressure change. The sensitivity can be obtained from the slope of the fitting curve, which is ~183 nm/Mpa. This discrepancy between the predicted and measured sensitivity could be attributed to the length of the SCSHF being longer than 1mm or the room temperature being lower than 20 ℃ according to Eq. (5.8).

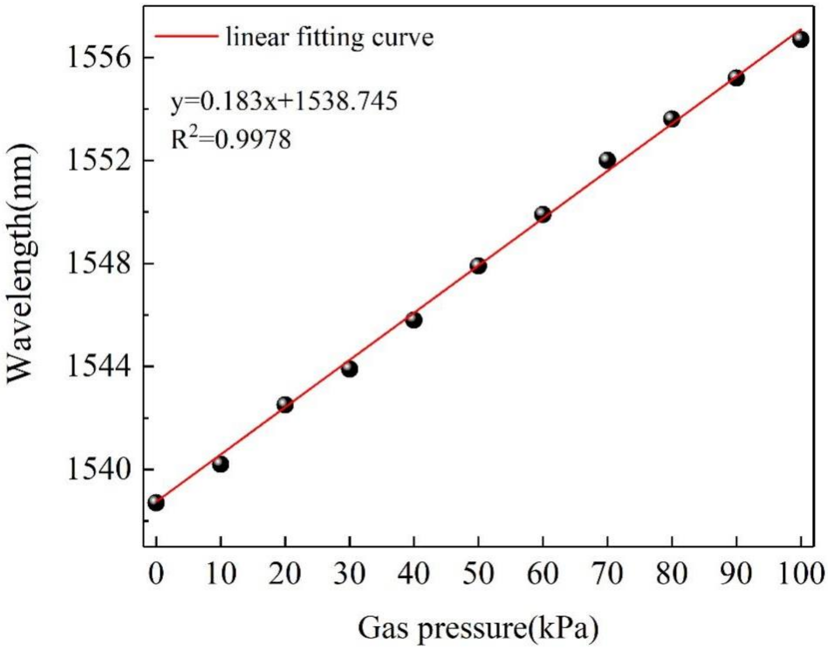

Fig. 5.11 The fitted curves between gas pressure change and wavelength shift of the chosen peak.

The measurement range is limited by the FSR of the envelope since it is not easy to distinguish if the chosen peak overlaps with the next interference peak. Then, the maximum gas pressure the proposed sensor can detect is calculated as FSR_v/SP=17 nm/(0.183 nm/kPa)≈92 kPa.

To test the sensing repeatability of the proposed sensor, a series of repetitive experiments are conducted based on the system in Fig. 5.9. The sensitivities in the processes of pressures increasing and decreasing are tested, as shown in Fig. 5.12 (a) to (c). The direction of the triangle indicates whether the pressure increasing or decreasing. The sensitivities of these three experiments are 187 nm/Mpa, 185 nm/Mpa, and 185 nm/Mpa, respectively. The fluctuation of the sensitivities is relatively small, verifying that the sensing repeatability of the proposed sensor is good.

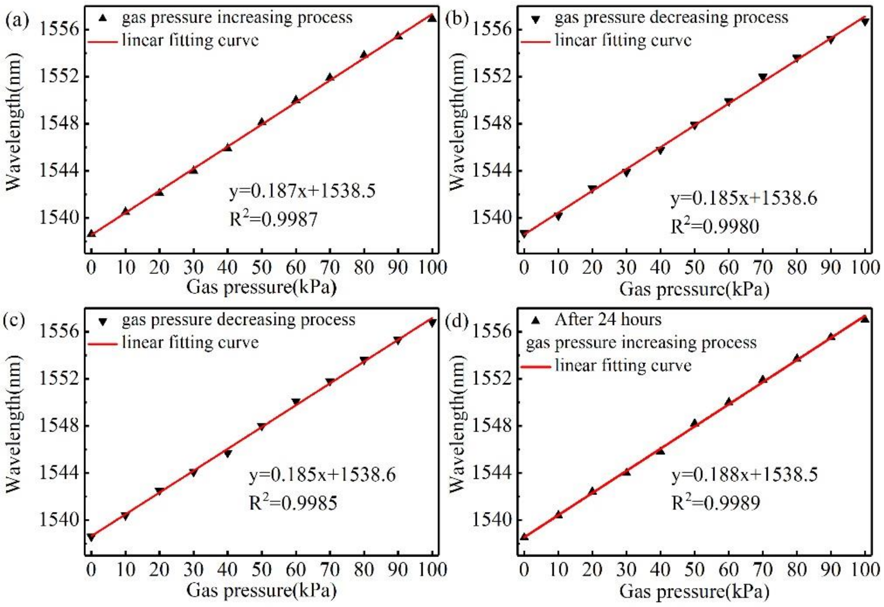

Fig. 5.12 The peak wavelengths under different gas pressures during the gas pressure increasing or decreasing process.

Another experiment is conducted 24 hours after the sensor is fabricated to test the long-term stability of the proposed sensor, and the result is shown in Fig. 5.12 (d). The sensitivity of this experiment is 188 nm/Mpa, which is almost no difference from the before the experiments. Thus, it can be said that the long-term stability of the proposed sensor is also quite good, increasing the value of practical applications.

5.4.2 Temperature Sensing Experiment

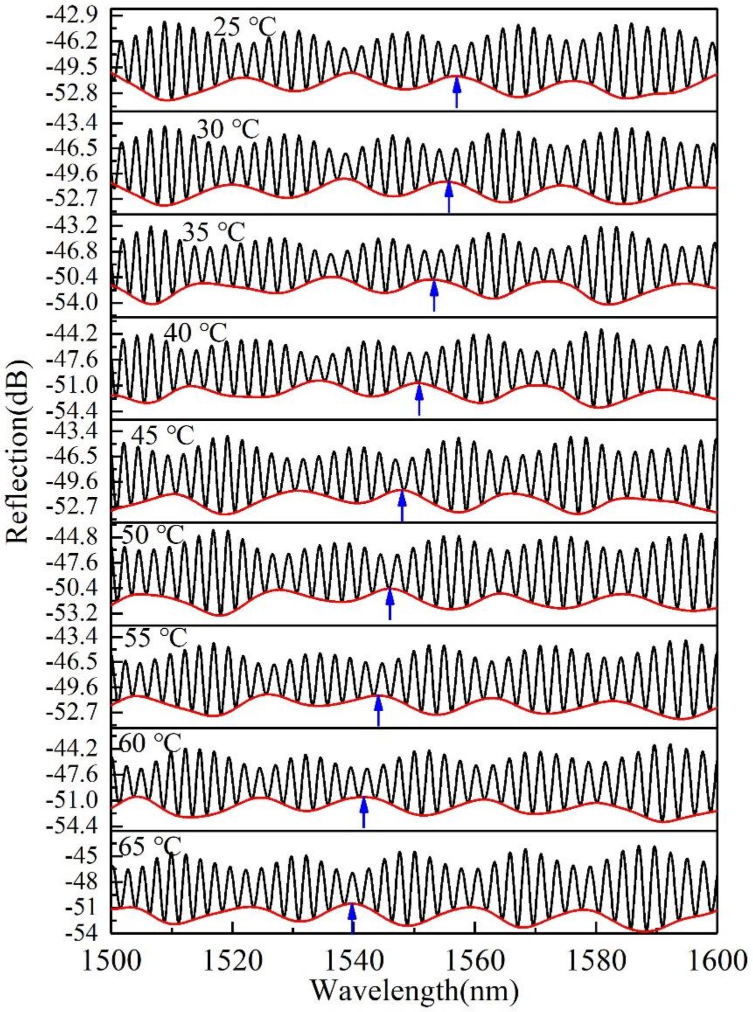

Fig. 5.13 The spectrums of the proposed sensor under different temperatures.

As for temperature measurement, the sensitivity S_T can be expressed as Eq. (5.10) based on the theories of the thermo-optical effect and thermal effect of solid materials.

$$S_T = \frac{d\lambda}{dT} = \frac{2}{m}\left[(3n_2 - 2n_1)\frac{dL}{dT} + L\left(3\frac{dn_2}{dT} - 2\frac{dn_1}{dT}\right)\right] \tag{5.10}$$

Substituting Eq. (3.6) into Eq. (10), the S_T can be calculated as

$$\begin{aligned} S_T &= \frac{\lambda}{L}\frac{dL}{dT} + \frac{\lambda}{3n_2 - 2n_1}\left(3\frac{dn_2}{dT} - 2\frac{dn_1}{dT}\right) \\ &= \frac{\lambda}{L}\alpha + \frac{\lambda}{3n_2 - 2n_1}(3\xi - 2\varsigma) \end{aligned} \tag{5.11}$$

Where $\boldsymbol{\alpha}$ is the thermal expansion coefficient of the fiber material, which is 5.2×10^{-7}/°C [111]. ξ is -9.295×10^{-7} at room temperature (20 °C) and standard atmospheric pressure (101.325 kPa) according to (7). ζ is the thermo-optical coefficient of the fiber material, which is 1.1×10^{-5}/°C [111]. Then, the theoretical S_T can be calculated to be 426.34 pm/°C.

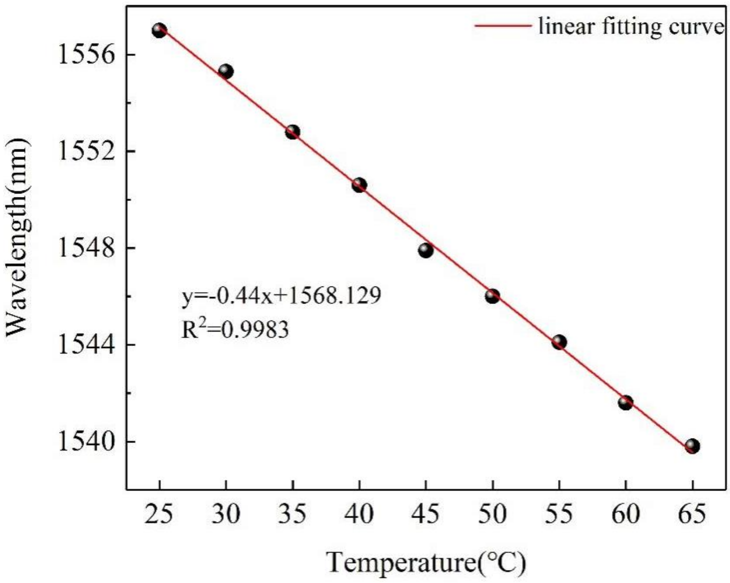

Fig. 5.14 The fitted curves between temperature and wavelength shift of the chosen peak.

The light path of the temperature sensing experiment is identical to that in the gas pressure sensing experiment but uses a temperature-controlled cabinet instead of a gas chamber. In complete contrast to the gas sensing experiment, the spectrum shifts to the short wavelength monolithically with the temperature increasing, as shown in Fig. 5.13. The peak wavelength around 1550 nm is chosen as the observation point.

According to the linear fitting result shown in Fig. 5.14, the proposed sensor can also respond linearly to the temperature change from 25 ℃ to 65 ℃ with a sensitivity of ~-440 pm/℃, which is very close to the theoretical sensitivity calculated in Chapter 5.3. Then, the temperature cross-sensitivity can be calculated as 2.4 kPa/℃, which is at a normal level compared to other sensors.

5.4.3 Comparison between Different Gas Pressure Sensors

The sensors displayed in Table V are all based on the cascaded structures with the OVE in the past five years. The sensitivity of the proposed sensor is at least two times higher than others. The ultrahigh sensitivity is attributed to the secondary reflection at the wall between the air hole and the HCF according to (9). Except for the sensor reported in [108] and our work, the sensors in the Table need a laser machine to drill an open cavity to ensure the external air can reach inside sensor structures, making the fabrication more complex. The proposed sensor presents better performance on temperature cross-sensitivity than the sensor reported in [107, 112] but is weaker than the sensors in [105, 106, 108, 111]. A temperature compensation such as FBG can be employed to solve this problem in practical measurements.

Table V The sensing performance of different fiber gas pressure sensors with OVE

Sensor structure	Gas pressure sensitivity (nm/MPa)	Temperature cross-sensitivity (kPa/°C)	Ref.
DSHF(MZIs)	-60	0.55	[105]
MMF+HCF (MZI)	-73.32	0.72	[106]
FPIs	86.64	5.18	[107]
SMF–SOHST–OFC(FPI)	80.3	1.33	[108]
HCFs (FPI)	80.8	2.2	[112]
Parallel FPIs	47.76	5.1	[113]
TCSHF+HCF	183	2.4	This work

5.5 Summary

An ultrasensitive gas pressure sensor based on the SCSHF with OVE is proposed in this chapter. The fabrication process of this sensor is quite simple, which only needs the operation of fusion splicing. A short section of the SCSHF is fusion splicing between the NCF and HCF. The function of the NCF is to expand the light field. The HCF serves as the connection channel between the inner section of the sensor and the external environment. The fusion splicing parameters are obtained from multiple attempts. Then the compositions of the sensor spectrum are analyzed to find the proper spectrum for the sensing experiment. The experimental results show that the proposed sensor has a sensitivity of 183 nm/MPa in 0~100 kPa, which is relatively high compared to the other sensors based on OVE. The good sensing repeatability and the long-term stability of the proposed sensor are also demonstrated by experiments. Since the proposed sensor works based on the reflected mode, it can be used in the remote sensing area. The temperature cross-sensitivity of the proposed sensor is calculated as -2.4 kPa/ ℃, which is only at a normal level compared to other sensors. Fortunately, this problem can be solved by employing a temperature compensation such as FBG. Thus, the proposed sensor has great application value in the sensing areas requiring high sensitivity, a simple fabrication process, remote sensing, and long-term stability.

However, the measurable range of the proposed sensor is not large enough, which limits its application. In the next step, we will try combining the gas pressure sensor with deep learning to enlarge the measurable range.

Chapter 6 Parallel Connection of Dual Michelson Interferometers for Lateral Stress Sensing Based on Polarization Maintaining Fiber with Optical Vernier Effect

In the last chapter, a probe-type FPI structure is proposed and experimentally demonstrated for gas pressure measurement. The probe-type sensors work based on the reflected light, which is more suitable for narrow places than sensors based on the transmitted light because there is no need for more space to be reserved for fiber bending. The light emission and receiver can be accommodated in the same fiber, which is cost-effective.

6.1 Introduction

The lateral stress sensor plays a crucial role in various optical fiber monitoring systems, serving diverse applications. For instance, in automotive technology, a lateral stress sensor integrated into car seat cushions aids in identifying seat occupancy [114]. Similarly, in building management systems, such sensors contribute to monitoring the structural health of large buildings [115]. Moreover, in vital signs monitoring systems, lateral stress sensors facilitate the detection of human heartbeat and respiratory rates [116].

Numerous fiber structures for lateral stress measurement have been reported recently. These include structures based on optical fiber gratings, such as FBG [117], LPFG [118], and TFBG [119]. Additionally, interferometer structures like MZI [120], SI [121], FPI [122], and MI [123] have also been built up for lateral stress measurement. However, the sensitivity of these individual structures is relatively low due to limitations in fiber deformation quantity [124].

To enhance sensor sensitivity for practical applications, researchers have shifted focus from individual structures to cascaded structures based on the OVE. For instance, Wang et al. designed cascaded MZI and SI structures with a lateral stress sensitivity of 1.28 nm/kPa [125]. Xu et al. demonstrated a dual FPI structure with a lateral stress sensitivity of 0.29 pm/psi [126]. Additionally, Yan et al. proposed a hybrid FPI/MZI interferometer for lateral stress sensing in 2011 [127]. In 2022, Li et al. designed a cascaded MI and SI structure for dual-parameter measurement of axial strain and lateral stress [128]. Although cascading interferometers together can amplify sensor sensitivity, this method increases system complexity [129].

In this Chapter, we propose a single MI-based lateral stress sensor utilizing PMF and the OVE. The high birefringence effect in PMF allows for the introduction of OVE into this single MI structure, enhancing sensitivity without the need for additional structures. Experimental results have validated the feasibility of this approach in enhancing sensitivity. Moreover, the proposed structure’s sensitivity can be customized according to specific requirements by adjusting the PMF length. This flexibility allows for fine-tuning the sensor's performance to meet desired sensitivity levels, enhancing its versatility across various applications. This sensor, functioning on a reflected light scheme, offers broader applications compared to sensors based on transmitted light schemes.

Another common challenge for optical fiber sensors is temperature cross-sensitivity [130]. To address this, we utilize an FBG as a temperature compensation element to demodulate temperature fluctuations. Experimental results demonstrate that the proposed sensor operates smoothly across temperatures ranging from 25°C to 65°C. Additionally, owing to its simple fabrication process, low cost, light size, and high sensitivity, this MI structure holds the potential for integration into various joint monitoring systems.

6.2 Michelson Interference and Optical Vernier Effect

6.2.1 Panda polarization-maintaining fiber

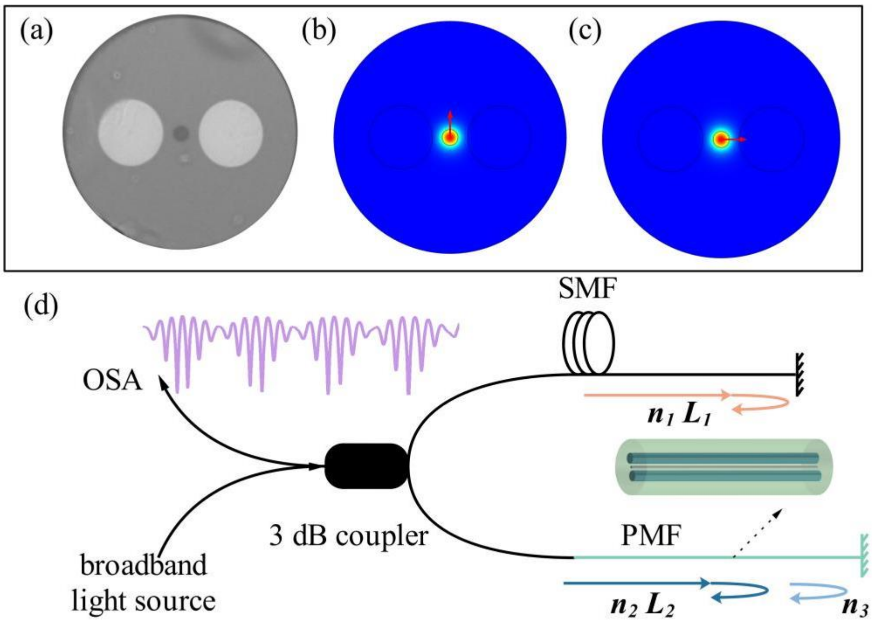

Fig. 6.1 (a) The cutaway view of the Panda-PMF, (b) and (c) The simulation results of the fundamental mode distribution in the Panda-PMF, (d) The structure chart of the proposed sensor.

The cutaway view of the Panda polarization-maintaining fiber (PMF) as observed under the Refractive Index Profiler (RIP, Arden Photonics nPA-400) is illustrated in Fig. 6.1 (a). The diameters of the fiber core and the stressed zone measured approximately 9.8 μm and 17 μm, respectively, with a distance of approximately 27 μm between them. The ERI of the stressed zone, core, and cladding are 1.43, 1.445, and 1.44, respectively.

Fig. 6.1 (b) and (c) depict the outcomes of the 2-D fundamental mode distribution simulation. The red arrow indicates the polarization direction of the electric field vector, which is mutually orthogonal. The ERI of the two polarization modes are 1.4417 and 1.442. The minor discrepancy between these modes arises from the high birefringence of the Panda PMF, quantified at 3.0×10^{-4}.

Using the above Panda PMF, a novelty sensor with OVE is designed, of which the fundamental structure is an MI. As shown in Fig. 6.1 (d), one arm of the MI is a section of SMF with a smooth cutting end. Another arm is a section of PMF with a well-cleaved end. Generally, a well-cleaved end of a fiber reflects about 4% of the incident light back to the fiber. Thus, in this work, the well-cleaved ends act as the reflected mirrors.

6.2.2 Spectrum Analysis

Because of the high-birefringence effect in the Panda PMF, the launched non-polarized light will orthogonally excite two polarization modes into the Panda-PMF. Thus, if a broadband laser light is injected into this fiber, there will be two reflected lights from the PMF end. Finally, these three back-reflected lights from two arms would interfere with each other after transmitting through the optical coupler, resulting in a Vernier spectrum with enhanced sensing characteristics.

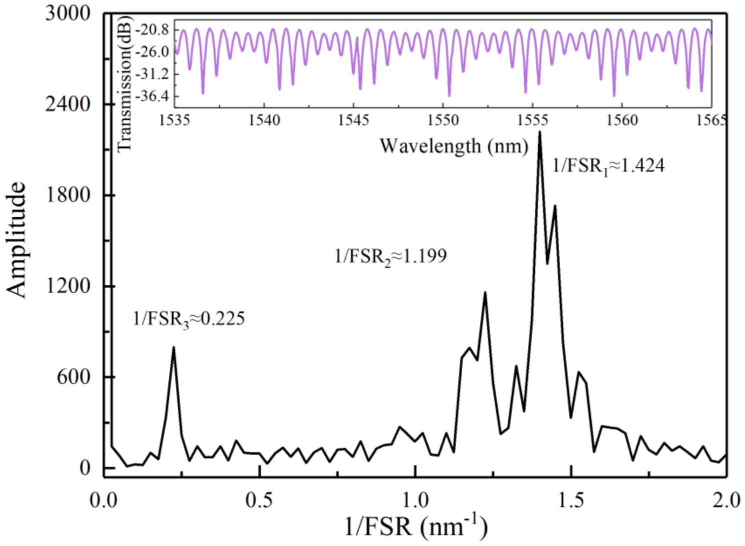

Fig. 6.2 The A-FFT result of the sensor spectrum

If the SMF length is **L_1**, the Panda-PMF length is **L_2**, the electric field intensity and ERI of the light in the SMF is E_1 and **n_1**, the electric field intensity and effective reflective index of the two lights in the Panda-PMF is **E_2** and **n_2**, **E_3**, and **n_3**, the final output electric field intensity can be express as following equation [131-136].

$$\begin{aligned} E_r &= E_1 \exp(-i\frac{4\pi n_1 L_1}{\lambda}) + E_2 \exp(-i\frac{4\pi n_2 L_2}{\lambda}) \\ &+ E_3 \exp(-i\frac{4\pi n_3 L_2}{\lambda}) \end{aligned} \tag{6.1}$$

Then, the reflected light intensity received at the optical coupler’s outport can be calculated as:

$$I_r = \left|E_r\right|\left|E_r^*\right| = E_1^2 + E_2^2 + E_3^2 + 2E_1E_2\cos\left[\frac{4\pi}{\lambda}\left(n_1L_1 - n_2L_2\right)\right]$$
$$+2E_1E_3\cos\left[\frac{4\pi}{\lambda}\left(n_1L_1 - n_3L_2\right)\right] + 2E_2E_3\cos\left[\frac{4\pi}{\lambda}\left(n_2 - n_3\right)L_2\right]$$

(6.2)

From Eq. (6.2), the output spectrum is a superimposition of three cosine function modulated waveforms, which is a typical OVE spectrum. The three interferometers' FSR can be calculated as:

$$FSR_1 \approx \frac{\lambda^2}{2(n_1L_1 - n_2L_2)}, FSR_2 \approx \frac{\lambda^2}{2(n_1L_1 - n_3L_2)}, FSR_3 \approx \frac{\lambda^2}{2(n_2 - n_3)L_2} \quad (6.3)$$

The relationship between the three FSRs can be expressed as:

$$FSR_3 = \frac{FSR_1 \bullet FSR_2}{\left|FSR_1 - FSR_2\right|} \quad (6.4)$$

Thus, the period of the Vernier envelope FSR_v is:

$$FSR_v = FSR_3 = \frac{\lambda^2}{2\left(n_2 - n_3\right)L_2} = \frac{4.004}{L_2} \quad (6.5)$$

The dip wavelength of the Vernier envelop λ_v can be calculated when the phase value of the envelope curve function is equal to 2(m+1)π.

$$\lambda_v = \frac{8BL_2}{2m+1}, m = 0,1,2...... \quad (6.6)$$

Where $B=|n_2-n_3|$, which is the birefringence index of the Panda-PMF. In this work, $B=3.0\times10^{-4}$, L_2=90 cm. The theoretical FSR_v and λ_v can be calculated as 4.45 nm and 1553.95 nm.

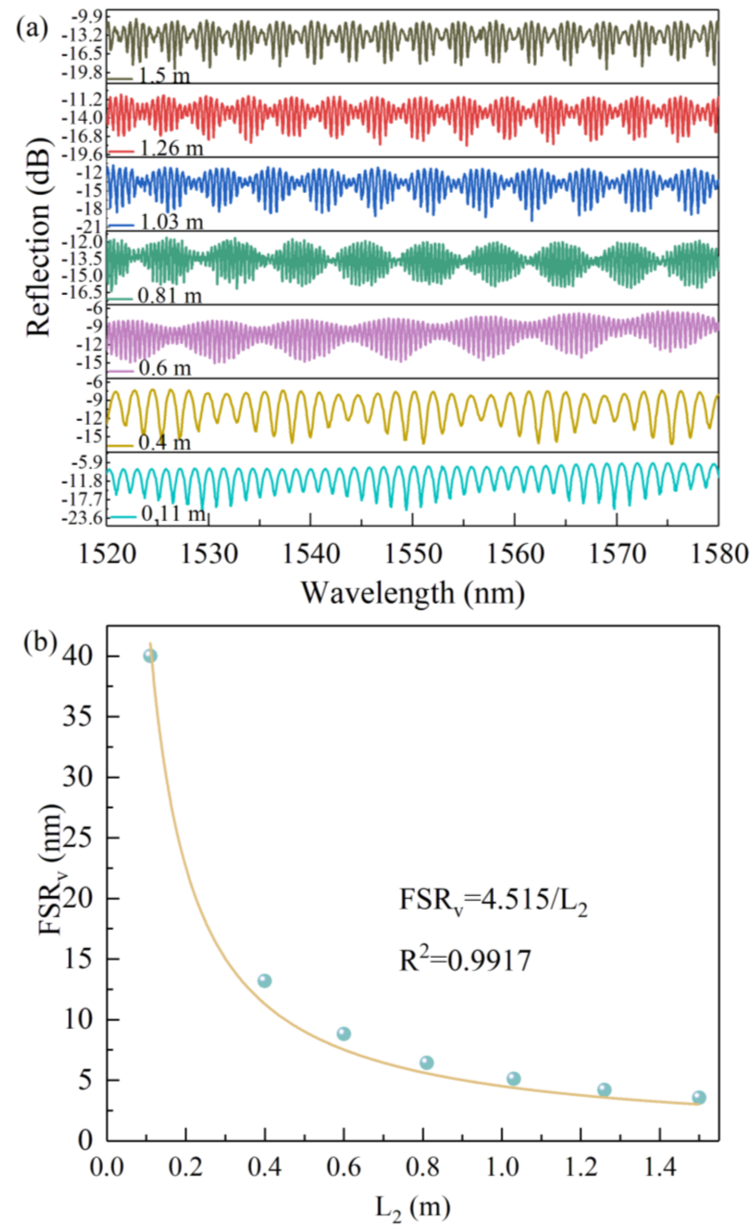

Fig. 6.3 The reflection spectrum of the proposed MI structure with different Panda-PMF lengths, (b) The fitting relationship between the period of the Vernier envelope FSR_v and the Panda-PMF length L_2

The A-FFT algorithm can be used to find out frequency components for wavelength domain signals, as shown in Fig. 6.2, where these three distinct peaks indicate the frequency components of our proposed sensor. The real FSR_v and λ_v are 4.6 nm and 1554.36 nm, which are all close to the theoretical values.

From Eq. (6.5), it can be inferred that the $\boldsymbol{FSR_v}$ is determined by PMF length $\boldsymbol{L_2}$. Fig. 6.3 (a) displays the spectrums of structures with different PMF lengths. The $\boldsymbol{FSR_v}$ gradually becomes larger with the $\boldsymbol{L_2}$ becoming shorter. Fig. 6.3 (b) shows the fitting specific change trends between $\boldsymbol{FSR_v}$ and $\boldsymbol{L_2}$. The parameter of the fitting equation is almost no different from the theoretical one in (6.5). The low accuracy of the fiber length $\boldsymbol{L_2}$ measurement and the reading of $\boldsymbol{FSR_v}$ possibly result in an error-fitting result.

6.3 Sensing Principle

Because of the non-circular symmetry structure of the PANDA-PMF, the lateral stress added to the PMF change results in the ERI change of the fundamental mode, then finally leading to the Vernier point shift, as Eq. (6.6) shows.

Then, the lateral stress sensing sensitivity is calculated as:

$$\frac{d\lambda_v}{dP} = \frac{8L_2}{2m+1}\frac{dB}{dP} \tag{6.7}$$

The sensitivity is proportional to the sensing part length of the PANDA-PMF. Thus, the proposed sensor’s sensitivity could be customized according to different application scenarios.

For temperature measurement, the Vernier point will also show a clear shift because of the thermos-optical effect and elasto-optical effect. The following equation can calculate the theoretical sensitivity of temperature measurement.

$$\frac{d\lambda_v}{dT} = \frac{8}{2m+1}\left(\frac{dB}{dT}L_2 + B\frac{dL_2}{dT}\right) \tag{6.8}$$

6.4 Experimental Results

6.4.1 Lateral Stress Measurement

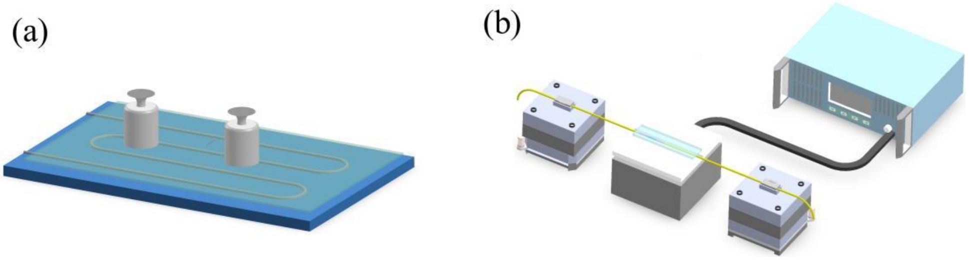

Fig. 6.4 The fiber placement way: (a) in lateral stress sensing experiment, (b) in temperature sensing experiment.

When conducting the lateral stress sensing experiment, a section of Panda-PMF is stuck on an acrylic plate as the detection element, as shown in Fig. 6.4(a). Another acrylic plate is put on the fiber sensing part to ensure an even distribution of the lateral stress. The changing of lateral stress added to the fiber is achieved by putting different numbers of farmers on the acrylic plate. Fig. 6.5(a) shows the output spectrums under rising lateral stresses with an interval of 1250 Pa. With lateral stress increasing, the spectrum moves to a longer wavelength direction.

Fig. 6.5(b) illustrates the fitting result between the Vernier peak at approximately 1550 nm and the lateral stress. The slope of this linear curve indicates the structure’s lateral stress sensitivity, which is ~0.564 nm/kPa. With a fitting degree of 0.9992, it indicates that the sensor exhibits a highly linear response to changes in lateral stress.

In the experimental setup, approximately 15 cm PMF, is casually positioned between two acrylic plates without differentiation between the fast and slow axes. Consequently, the normalization sensitivity can be computed as 0.564/0.15 = 3.76 nm/(kPa·m), a value independent of the fiber length.

Typically, reported sensitivities of interferometric sensors hover around tens of picometers per thousand Pascals [137]. However, owing to the OVE, the structure’s sensitivity significantly surpasses that of conventional interferometric sensors, registering several times higher sensitivity.

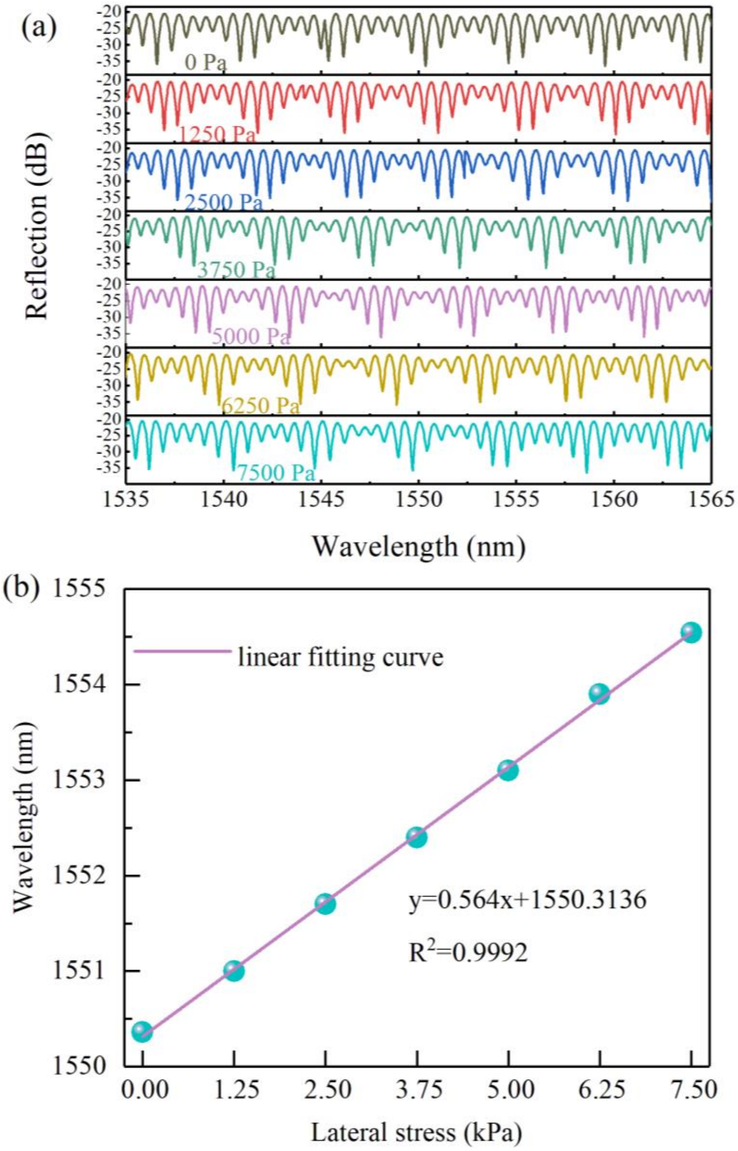

Fig. 6.5 (a) The Vernier spectrums obtained after adding different lateral stress, (b) the fitting result between the lateral stress added on the fiber and the wavelength of the Vernier point.

6.4.2 Temperature Measurement

The temperature response of the structure is also tested using the equipment in Fig 6.4(b). The test results are shown in Fig. 6.6 (a) and (b). With temperature increasing from 24 ℃ to 38 ℃, the spectrum moves linearly to a shorter wavelength direction with a sensitivity of 0.3155 nm/℃. Then, the temperature cross-sensitivity can be calculated as -0.56 kPa/℃. Although this value is not very high, it still can result in a relatively large error for lateral stress measurement in practical applications.

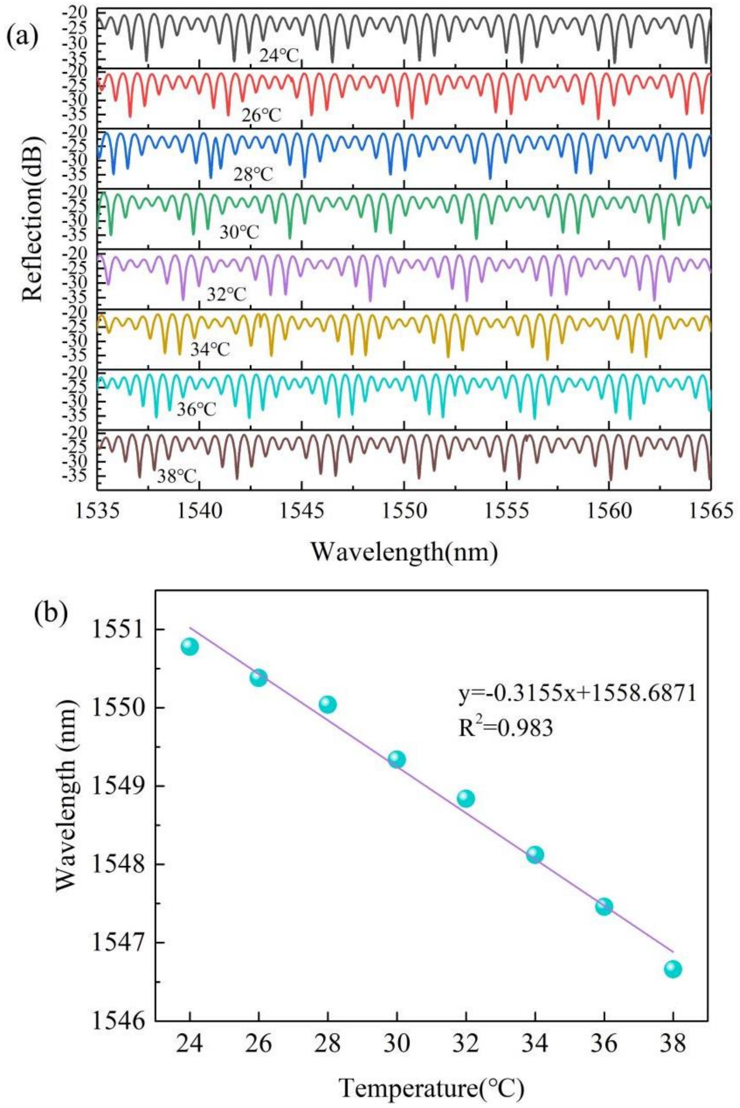

Fig. 6.6 (a) The reflection spectrums recorded from 24 ℃ to 38 ℃, (b) the fitting result between temperature and Vernier point wavelength.

6.4.3 Temperature Compensation based on an FBG

To eliminate the temperature cross-sensitivity, an FBG is used as the temperature compensation element. The FBG is cascaded at the optical coupler's output port to ensure the MI's arm difference is not changed as shown in Fig. 6.7. If the phase difference changes, the final spectrum and sensitivity change correspondingly, resulting in errors for the following temperature demodulation process.

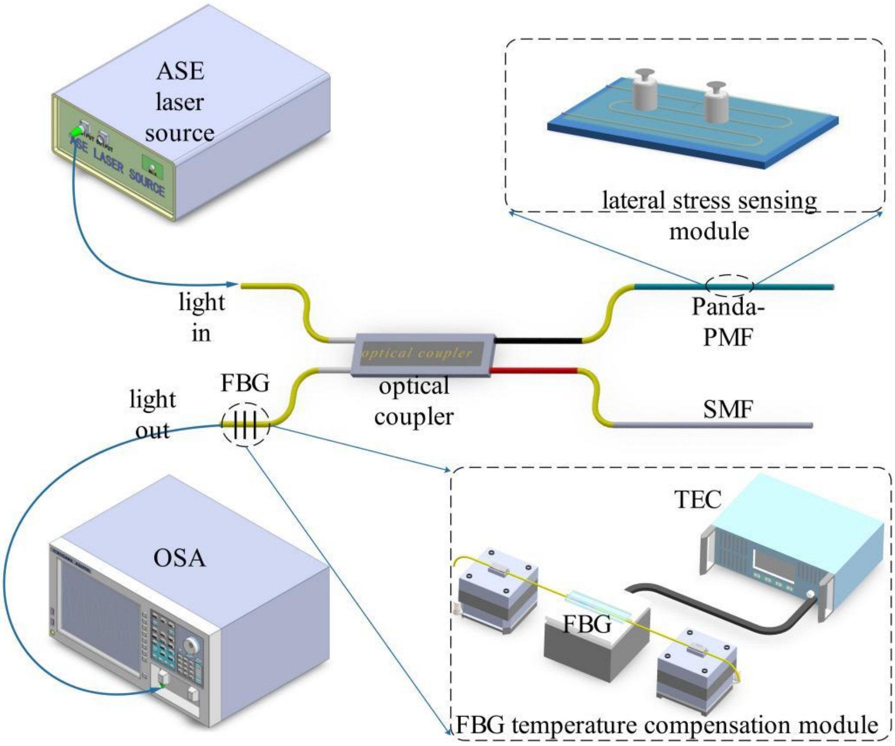

Fig. 6.7 The lateral stress measurement system with an FBG as temperature compensation component.

This experiment comprises two stages. Firstly, the lateral stress applied to the PMF is changed from 0 Pa to 1000 Pa while concurrently increasing the environmental temperature from 20 °C to 25 °C. Subsequently, while maintaining constant lateral stress, the temperature is further increased from 25 °C to 65 °C with 5 °C increments.

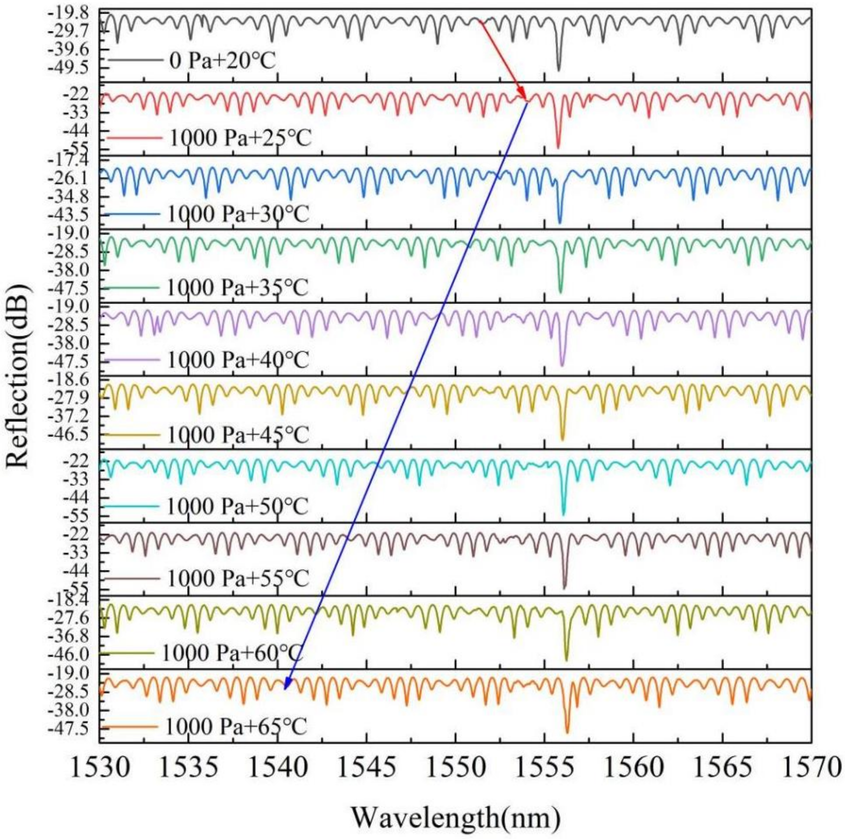

Fig. 6.8 The reflection spectrum under different conditions in the temperature compensation experiment.

Fig. 6.8 depicts the spectra acquired during the experimental process, revealing a distinct loss dip induced by the FBG. Fig. 6.9 illustrates the wavelength of the FBG loss dip under different temperatures. Notably, the FBG loss dip shifts to longer wavelengths with temperature rising. The temperature sensitivity of the utilized FBG is ~ 10 pm/℃.

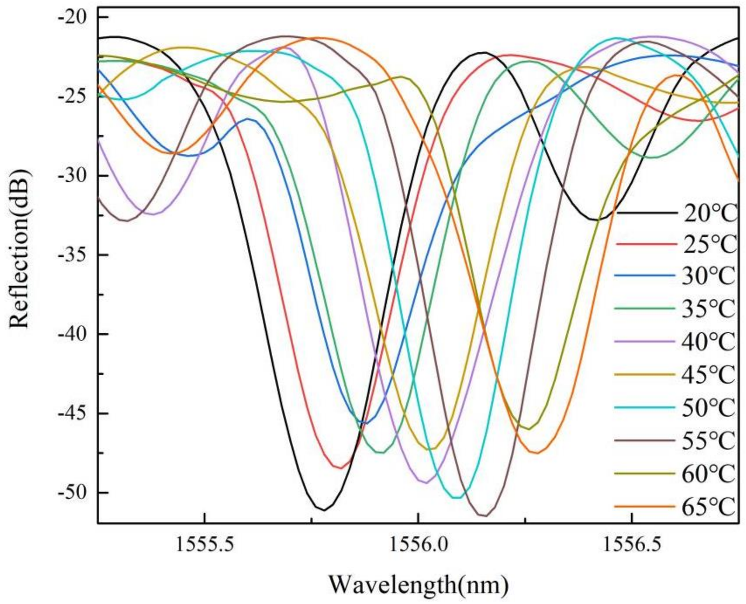

Fig. 6.9 The wavelength of the FBG loss dip under different temperatures.

The demodulation process involves three distinct steps. Firstly, the temperature change value is demodulated by calculating the wavelength shift value of the FBG loss dip. Subsequently, the vernier spectrum is realigned to its original position before the temperature shift. Finally, the restored spectrum is compared with the original spectrum to derive the lateral stress change value. Lateral stress changes of 500 Pa, 1000 Pa, and 1500 Pa are individually applied to the fiber. The demodulation results are illustrated in Fig. 6.10. Take the orange series of dots as an example, the ordinate values of the points present the actual temperature value. The abscissa values are the demodulated lateral stress values. The blue areas present the permitted error range of ± 200 Pa. If a point position is in the blue area, this demodulation result is correct.

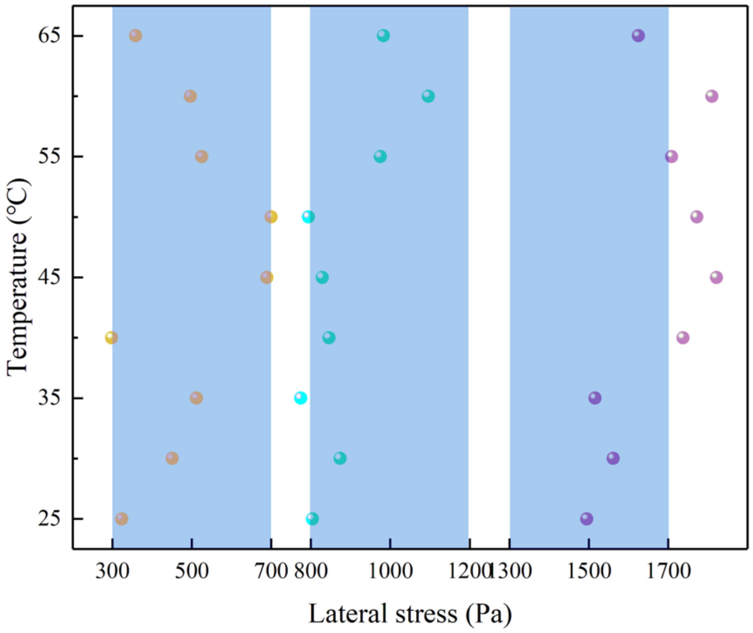

Fig. 6.10 The lateral stress demodulation results of the temperature compensation experiment.

In the permitted error range of ± 200 Pa, the lowest accuracy rate is 44.4%, and the best of 77.8% can be achieved with a resolution of 500 Pa. The OSA's low resolution and FBG sensitivity can lead to inaccurate temperature demodulation values and result in error lateral stress values. Besides using high-resolution OSA and high-sensitivity FBG, relying on the machine learning algorithm to solve this problem is the research direction for our next step. In this experiment, using the FBG as the temperature compensation element greatly expands the operating temperature range of the proposed sensor.

6.4.4 Comparison with Other Lateral Stress Sensors

Table VI The sensing performance comparison between different sensor structures

Structure	Sensitivity (pm/MPa)	Measurement Range (kPa)	Ref.
Dual FPIs	42.56	2.2	[126]
MI+SI	$3.13*10^6$	1.2	[128]
FBG-grapefruit fiber	12.86	25000	[138]
SHTC	110.8	200000	[139]
PMF-PCF	4210	20000	[140]
Dual MIs	$3.76*10^6$	7.5	This work

From Table VI, the sensitivity of the fabricated MI structure is much higher than that of other types of sensors. However, the measurement range of the proposed sensor is not competitive with other sensors. This problem is also a common failing for interferometric sensors. Machine learning can help solve this problem, which is also the research point for our next step.

6.5 Summary

In this chapter, we introduce an ultra-sensitive optical lateral stress sensor incorporating OVE, whose feasibility is empirically validated. The sensor's core structure comprises an optical fiber MI constructed around an optical coupler. One arm of the MI consists of SMF with a precisely cleaved end, while the other arm comprises Panda-PMF with a similarly cleaved end. Leveraging fiber end reflection and the birefringence effect, the interaction of three reflected lights from the two arms yields a significantly enhanced sensing capability, manifesting as a large envelope modulation in the output spectrum. Experimental findings demonstrate the sensor's linear response to lateral stress variations, boasting a sensitivity of 3.76 nm/(kPa · m). Additionally, this structure has a temperature cross-sensitivity of approximately -0.56 kPa/°C.

The proposed sensor employs readily available commercial fibers as its raw materials, rendering it cost-effective for mass production. Moreover, its fabrication process involves only fusion splicing, ensuring simplicity and efficiency. Notably, the sensor's lateral stress sensitivity surpasses that of similar sensors, offering superior performance. Furthermore, operating on reflected light rather than transmitted light, the sensor is well-suited for integration as a probe in various sensing applications, enhancing its versatility across monitoring systems.

Temperature compensation experiments using FBG are also conducted to simulate the actual usage. The best accuracy of 77.8% is achieved under temperature disturbance. Additionally, the prospect of integrating the sensor with machine learning techniques presents an intriguing avenue for further research.

Chapter 7 Conclusion and Future Work

7.1 Conclusion

In this thesis, four interferometric sensor structures are experimentally demonstrated for different sensing applications. Although the four sensor structures are different, their working mechanism is all based on amplitude splitting interference. In the second place, they are built up based on a section of micro-structure fiber. The temperature cross-sensitivity problem is solved properly by dual parameters measurement or temperature compensation method. The sensing results coincided with the theoretical analysis. Thus, the proposed sensors have great application potential in different fields.

The first sensor is a lateral stress sensor based on the SI. A section of BiF is used in the Sagnac loop to motivate two polarization lights for interference. Because the fiber used is not circularly symmetric, the change of the lateral stress on the fiber can result in the shifting of the interference fringe. The sensitivity is about 1.72 nm/kPa. If a laser beam at a specific wavelength is injected into the sensor structure, this sensor can be used for heartbeat and breath rate monitoring. Compared to the electrocardiograph monitoring method, this sensor can not only recover the heartbeat signal without any error but also can monitor the breath signal simultaneously. In addition, this sensor shows great characteristics of resisting temperature because the fiber material is pure silica without any doped materials. Thus, the proposed sensor can replace the electrocardiograph monitoring method in the high electromagnetic environment.

The second sensor, an ultra-sensitive axial strain sensor employing the OVE, comprises two cascaded MZIs with differing FSRs. Each MZI is crafted by fusion splicing approximately 3 mm of TCSHF between two segments of about 5 mm of NCF. Independently, each MZI displays linear responsiveness to alterations in axial strain and temperature. The sensitivities are roughly 0.6 pm/με and 34 pm/℃. When linked in series, the cascaded MZIs demonstrate an amplified sensitivity, augmented by approximately 30 times due to the OVE. The cascaded structure achieves sensitivities of approximately 17 pm/με within the range of 0 to 2000 με for axial strain sensing, and of roughly 1.16 nm/℃ within the range of 30 to 70 ℃ for temperature sensing. Additionally, the cascaded structure enables simultaneous measurement of axial strain and temperature changes within acceptable error margins.

The third sensor, an ultra-sensitive gas pressure sensor, is formed by fusion splicing a segment of SCSHF between NCF and HCF. Exclusively involving fusion splicing, this structure is fabricated with OVE. The theoretical sensing principles underlying the sensor's operation are elaborated comprehensively. Utilizing the reflected mode, the sensor effectively functions as a probe in confined spaces. Within the range of 0 to 100 kPa, the sensor's capability to detect gas pressure changes with a sensitivity of approximately 183 nm/MPa. Repeated experiments confirm the sensor's exceptional sensing repeatability and long-term stability. Furthermore, the sensor exhibits a low-temperature cross-sensitivity of about 2.4 kPa/°C. Thus, the proposed sensor holds promise for practical application in sensing scenarios requiring high sensitivity, a straightforward fabrication process, and long-term stability.

The last sensor is an ultra-sensitive optical lateral stress sensor with the OVE. The fundamental structure of this sensor is an optical fiber MI based on an optical coupler. One arm of the MI is built up by the SMF with a well-cleaved end while the other arm is built up by the Panda PMF with a well-cleaved end. Due to the fiber end reflection and the birefringence effect, the OVE is motivated, generating an extensive envelope modulation with enhanced sensing capabilities on the output spectrum. This structure exhibits a linear response to lateral stress variations ranging from 0 to 7.5 kPa, with a uniformization sensitivity of 3.76 nm/(kPa·m). Additionally, the temperature cross-sensitivity of the sensor is approximately ~0.56 kPa/°C. By compensating for temperature cross-sensitivity using an FBG, the sensor can operate ideally within an extended temperature range while remaining within the acceptable error margins.

7.2 Future Works

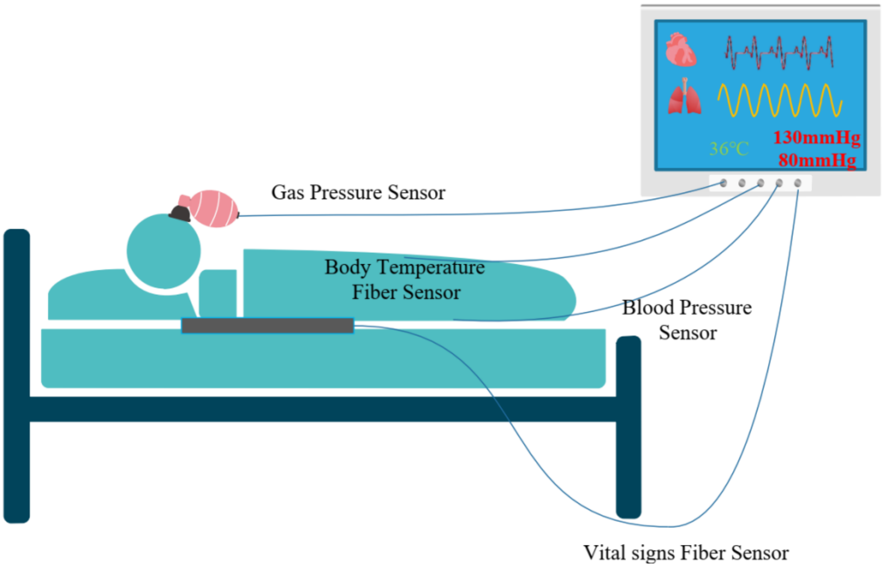

Fig. 7.1 All fiber sensors-based vital signs monitoring system.

For the next step, an all-fiber sensors-based vital signs monitoring system will be studied based on different types of fiber sensors to evaluate body conditions all around. This system cannot only monitor the heartbeat and breath rate, but also many other vital signs such as the body temperature, blood pressure, and exhaled gas composition.

For human beings, there are many different working mechanisms to detect heart signals. For example, small body vibrations are caused by the heartbeat, pulse signals at the wrist, and pulsating blood flow signals at the fingertip. By detecting the time delay between different heartbeat signals, blood pressure can be easily obtained. Combining the proposed non-contact sensor in Chapter 3 with another type of fiber sensor can achieve simultaneous measurement of heat beat ratio and blood for the bed patients.

There are more than 3000 volatile organic compounds (VOCs) in human exhaled air, which are directly or indirectly related to the body's pathophysiological processes [141]. Therefore, detection and quantitative analysis of VOCs can help discover and evaluate some diseases in the early period. The sensor proposed in Chapter 5 can measure the gas pressure change by detecting the air ERI change caused by pressure change. If this sensor is combined with materials that are sensitive to the specific gas, the sensor can achieve non-invasive, painless, economical, and time-saving exhaled breath analysis [142]. It is a new field that is developing rapidly and has great potential in disease screening and clinical diagnosis.

The body temperature can be easily detected by the temperature sensor. However, the problem is that the fluctuation range of body temperature is quite small even in the case of having a high fever. Thus, the temperature sensor needs high resolution to ensure measurement accuracy [143]. In addition, because the temperature at different epidermis parts is different and the most accurate part is oxter, the reflected type of sensor may be more suitable [144].

Addressing sensor structure challenges is imperative for developing an all-fiber sensor-based vital signs monitoring system. Moreover, attention to data processing and transmission aspects is crucial for future applications [145]. Further research is warranted to overcome these challenges and realize the full potential of all-fiber sensor technology in healthcare monitoring.

Bibliography

[1] Brian Culshaw, “Optical Fiber Sensor Technologies: Opportunities and - Perhaps - Pitfalls,” J. Lightwave Technol. vol 22, no.1, pp.39-50, Jan. 2004.

[2] B. Lee, S. Roh, J. Park, “Current status of micro- and nano-structured optical fiber sensors”, Optical Fiber Technology, vol. 15, no.3, pp.209-221, June 2009.

[3] P. C, Silva I. “Optical Fiber Sensors and Sensing Networks: Overview of the Main Principles and Applications”, Sensors, vol. 22, no. 19, art. 7554, Oct. 2022.

[4] Bado MF, Casas JR, “A Review of Recent Distributed Optical Fiber Sensors Applications for Civil Engineering Structural Health Monitoring”, Sensors, vol. 21, no.5, art. 1818, Mar. 2021.

[5] K. Wang *et al*., “Advances in Optical Fiber Sensors Based on Multimode Interference (MMI): A Review”, IEEE Sensors Journal, vol. 21, no. 1, pp. 132-142, Jan. 2021.

[6] Chen Y, Zhao L, Hao S, Tang J. “Advanced Fiber Sensors Based on the Vernier Effect”, Sensors, vol. 22, no.7, art. 2694, Mar. 2022.

[7]A. G. Leal-Junior, C. A. R. Diaz, L. M. Avellar, M. J. Pontes, C. Marques and A. Frizera, “Polymer optical fiber sensors in healthcare applications: A comprehensive review”, *Sensors*, vol. 19, no. 14, pp. 3156, Jul. 2019.

[8]C. Broadway, R. Min, A. G. Leal-Junior, C. Marques and C. Caucheteur, “Toward commercial polymer fiber Bragg grating sensors: Review and applications”, *J. Lightw. Technol.*, vol. 37, no. 11, pp. 2605-2615, Jun. 2019.

[9] S. Pevec and D. Donlagic, “Multiparameter fiber-optic sensors: A review”, *Opt. Eng.*, vol. 58, no. 7, pp. 1-26, 2019.

[10] H.-E. Joe, H. Yun, S.-H. Jo, M. B. Jun and B.-K. Min, “A review on optical fiber sensors for environmental monitoring”, Int. J. Precis. Eng. Manuf.-Green Technol., vol. 5, no. 1, pp. 173-191, 2018.

[11] Kunimasa Saitoh and Shoichiro Matsuo, “Multicore Fiber Technology,” J. Lightwave Technol., vol.34, no. 1, pp. 55-66, Aug. 2016.

[12] S. D. Personick, Fiber Optics, New York: Plenum, 1985.

[13] Udd, E., “The Emergence of Fiber Optic Sensor Technology”, In Fiber Optic Sensors, Jul. 2011.

[14] Yong Zhao, Hang Zhao, Ri-qing Lv, Jian Zhao, “Review of optical fiber Mach-Zehnder interferometers with micro-cavity fabricated by femtosecond laser and sensing applications,” Optics and Lasers in Engineering, vol. 117, pp. 7-20, June 2019.

[15] Tanya M. Monro, and Heike Ebendorff-Heidepriem, “Progress in microstructured optical fibers,” Annual Review of Materials Research, vo. 36, pp.467-495, Aug. 2006.

[16] M. Yang, J. Dai, C. Zhou and D. Jiang, “Optical fiber magnetic field sensors with TbDyFe magnetostrictive thin films as sensing materials”, Opt. Exp., vol. 17, no. 23, pp. 20777-20782, 2009.

[17] M. J. Gander, W. N. MacPherson, J. S. Barton, R. L. Reuben, J. D. C. Jones, R. Stevens, et al., “Embedded micromachined fiber-optic Fabry-Perot pressure sensors in aerodynamics applications”, IEEE Sensors J., vol. 3, no. 1, pp. 102-107, Feb. 2003.

[18] S. Silva et al., "Ultrahigh-sensitivity temperature fiber sensor based on multimode interference", Appl. Opt., vol. 51, no. 16, pp. 3236-3242, Jun. 2012.

[19] X.-D. Wang and O. S. Wolfbeis, “Fiber-optic chemical sensors and biosensors (2015–2019)”, *Anal. Chem.*, vol. 92, no. 1, pp. 397-430, Jan. 2020.

[20] A. Leung, P. M. Shankar, and R. Mutharasan, “A review of fiber-optic biosensors”, *Sens. Actuators B Chem.*, vol. 125, no. 2, pp. 688-703, 2007.

[21] S. Pevec and D. Donlagic, “Multiparameter fiber-optic sensors: A review”, *Opt. Eng.*, vol. 58, no. 7, pp. 1-26, 2019.

[22] Z. Ding et al., “Distributed optical fiber sensors based on optical frequency domain reflectometry: A review”, *Sensors*, vol. 18, no. 4, pp. 1072, Apr. 2018,

[23] B. Lee, “Review of the present status of optical fiber sensors”, *Opt. Fiber Technol.*, vol. 9, no. 2, pp. 57-79, 2003.

[24] Guzmán-Sepúlveda JR, Guzmán-Cabrera R, Castillo-Guzmán AA., “Optical Sensing Using Fiber-Optic Multimode Interference Devices: A Review of Nonconventional Sensing Schemes”, *Sensors*, vol. 21, no. 5, art. 1862, Feb. 2021.

[25] Lee, B.H., Kim, Y.H., Park, K.S., Eom, J.B., Kim, M.J., Rho, B.S., and Choi, H.Y., “Interferometric fiber optic sensors”, *Sensors*, vol. 12, no. 3, pp. 2467–2486, Feb. 2012.

[26] Viennot, L. “Superposition of waves and optical imaging”. In Teaching Physics. Springer, Dordrecht, pp. 147-179.

[27] J. Salz, “Coherent Lightwave communications,” in *AT&T Technical Journal*, vol. 64, no. 10, pp. 2153-2209, Dec. 1985.

[28] Gomes AD, Ferreira MS, Bierlich J, Kobelke J, Rothhardt M, Bartelt H, Frazão O., “Optical Harmonic Vernier Effect: A New Tool for High Performance Interferometric Fiber Sensors”, *Sensors*, vol. 19, no.24, art. 5431. 2019.

[29] Nan, T., Liu, B., Wu, Y., Wang, J., Mao, Y., Zhao, L., Sun, T., Wang, J., “Ultrasensitive strain sensor based on Vernier-effect improved parallel structured fiber-optic Fabry-Perot interferometer,” *Opt. Express*, vol. 27, no. 12, pp. 17239–17250, June 2019.

[30] P. Zhang et al., “Cascaded fiber-optic Fabry-Perot interferometers with Vernier effect for highly sensitive measurement of axial strain and magnetic field,” *Opt. Express*, vol. 22, no.16, pp. 19581-19588, Aug. 2014.

[31] J. Zhang et al., “Ultrasensitive Temperature Sensor with Cascaded Fiber Optic Fabry–Perot Interferometers Based on Vernier Effect,” *IEEE Photon. J.*, vol. 10, no. 5, pp. 1-11, Oct. 2018.

[32] Y. Wu, L. Xia, W. Li, and J. Xia, "Highly Sensitive Fabry–Perot Demodulation Based on Coarse Wavelength Sampling and Vernier Effect," *IEEE Photon. Technol. Lett.*, vol. 31, no. 6, pp. 487-490, 2019.

[33] Hao Liao, Ping Lu, Xin Fu, Xinyue Jiang, Wenjun Ni, Deming Liu, and Jiangshan Zhang, "Sensitivity amplification of fiber-optic in-line Mach–Zehnder Interferometer sensors with modified Vernier-effect," *Opt. Express*, vol. 25, no. 22, pp. 26898-26909, Oct. 2017

[34] M. Xie, H. Gong, J. Zhang, C. Zhao, and X. Dong, "Vernier effect of two cascaded in-fiber Mach–Zehnder interferometers based on a spherical-shaped structure," Appl. Opt. vol. 58, no. 23, pp. 6204-6210, Aug. 2019.

[35] H. Lin, F. Liu, H. Guo, A. Zhou, and Y. Dai, "Ultra-highly sensitive gas pressure sensor based on dual side-hole fiber interferometers with Vernier effect," *Opt. Express* vol. 26, no. 22, pp. 28763-28772, Oct. 2018.

[36] Y. Li, P. Xu, W. Lyu, Y. Liu and C. Yu, "Fiber Lateral Stress Sensor Based on Michelson Interference and Optical Vernier Effect," *J. Lightwave Technol.*, early access, doi: 10.1109/JLT.2024.3382105.

[37] S. Zhang, Y. Liu, H. Guo, A. Zhou and L. Yuan, “Highly Sensitive Vector Curvature Sensor Based on Two Juxtaposed Fiber Michelson Interferometers with Vernier-Like Effect,” *IEEE Sens. J.*, vol. 19, no. 6, pp. 2148-2154, Mar. 2019.

[38]P. M. R. Robalinho, A. D. Gomes and O. Frazão, “High Enhancement Strain Sensor Based on Vernier Effect Using 2-Fiber Loop Mirrors,” IEEE Photonics Technol. Lett., vol. 32, no. 18, pp. 1139-1142, Sept. 2020.

[39] B. Wu, C. Zhao, B. Xu, Y. Li, “Optical fiber hydrogen sensor with single Sagnac interferometer loop based on vernier effect”, Sens. Actuators, B, vol. 55, no.3, pp. 3011-3016, Feb. 2018.

[40] Y. Ying, C. Zhao, H. Gong, S. Shang, L. Hou, “Demodulation method of Fabry-Perot sensor by cascading a traditional Mach-Zehnder interferometer”, Opt. Laser Technol., vol. 118, pp. 126-131, Oct. 2019.

[41] W. Yang, R. Pan, L. Zhang, Y. Yang, L. Li, S. Yu, X. Sun, and Xi. Yu, “Highly sensitive fiber-optic temperature sensor with compact hybrid interferometers enhanced by the harmonic Vernier effect,” Opt. Express vol. 31, no.9, pp.14570-14582, April 2023

[42] Hoang ChuDuc, Kien NguyenPhan, Dung NguyenViet, “A Review of Heart Rate Variability and its Applications,” APCBEE Procedia, vol.7, pp. 80-85, 2013.

[43]Acharya U, R., N, K., Sing, O.W. *et al.*, “Heart rate analysis in normal subjects of various age groups.” *BioMed. Eng. Online*, vol. 3, art. no. 24, July 2004.

[44]Heikki V. Huikuri, Timo H. Mäkikallio, “Heart rate variability in ischemic heart disease”, *Autonomic Neuroscience*, vol. 90, no. 1–2, pp. 95-101, July 2001.

[45]S. Boonnithi and S. Phongsuphap, “Comparison of heart rate variability measures for mental stress detection”, *2011 Computing in Cardiology*, Hangzhou, China, pp. 85-88, 2011.

[46]Nogués, Martín A. MD, Benarroch, Eduardo MD., “Abnormalities of Respiratory Control and the Respiratory Motor Unit”, The Neurologist, vol. 14, no. 5, pp. 273-288, Sept. 2008.

[47]N. Giardino, P. Lehrer, and R. Edelberg, “Comparison of finger plethysmograph to ECG in the measurement of heart rate variability,” *Psychophysiology*, vol. 39, no. 2, pp. 246–253, 2002.

[48] D. Biswas, N. Simoes-Capela, C. Van Hoof, and N. Van Helleputte, “Heart rate estimation from wrist-worn

photoplethysmography: a review,” *IEEE Sens. J.* vol. 19, no. 16, pp. 6560–6570, 2019.

[49]C. L. Levkov, “Orthogonal electrocardiogram derived from the limb and chest electrodes of the conventional 12-lead system,” *Med. Biol. Eng. Comput.*, vol. 25, no. 2, pp. 155–164, 1987.

[50]C. Massaroni et al., “Validation of a wearable device and an algorithm for respiratory monitoring during exercise”, *IEEE Sens. J.,* vol. 19, no. 12, pp. 4652–4659, 2019.

[51]A. Ukil, H. Braendle and P. Krippner, “Distributed temperature sensing: Review of technology and applications”, *IEEE Sensors J.*, vol. 12, no. 5, pp. 885-892, May 2012.

[52]Z. Chen *et al.*, “Simultaneous measurement of breathing rate and heart rate using a micro-bend multimode fiber optic sensor,” *J. Biomed. Opt.*, vol. 19, no. 5, pp. 057001, May. 2014.

[53] C. Massaroni *et al.*, “Design and Feasibility Assessment of a Magnetic Resonance-Compatible Smart Textile Based on Fiber Bragg Grating Sensors for Respiratory Monitoring,” *IEEE Sensors Journal*, vol. 16, no. 22, pp. 8103-8110, Nov.15, 2016.

[54] Fengze Tan, Shuyang Chen, Weimin Lyu, Zhengyong Liu, Changyuan Yu, Chao Lu, and Hwa-Yaw Tam, “Non-invasive human vital signs monitoring based on twin-core optical fiber

sensors," Biomed. Opt. Express, vol. 10, no. 11, pp. 5940-5952, Oct. 2019.

[55] Weihao Yuan, Lingduo Li, Yu Wang, Zhenggang Lian, Daru Chen, Changyuan Yu, and Chao Lu, "Temperature and curvature insensitive all-fiber sensor used for human breath monitoring," Opt. Express, vol. 29, no. 17, pp. 26375-26384, Aug. 2021.

[56]P. Jiang, L. Ma, Z. Hu, and Y. Hu, "Low-Crosstalk and Polarization-Independent Inline Interferometric Fiber Sensor Array Based on Fiber Bragg Gratings," J. Lightwave Technol., vol. 34, no. 18, pp. 4232-4239, 2019. 56

[57] C. Y. Lin, L. A. Wang, and G. W. Chern, "Corrugated long-period fiber gratings as strain, torsion, and bending sensors," J. Lightwave Technol., vol. 19, no.8, pp.1159–1168, 2001.

[58] Y. Li, P. Lu, C. Zhang, W. Ni, D. Liu, and J. Zhang, "Sensing Characterization of Helical Long Period Fiber Grating Fabricated by a Double-Side CO^2 Laser in Single-Mode Fiber," IEEE Photon. J., vol. 11, no. 3, pp.1-8, 2019.

[59]Z. Zhang, T. Guo, and B. Guan, "Reflective Fiber-Optic Refractometer Using Broadband Cladding Mode Coupling

Mediated by a Tilted Fiber Bragg Grating and an In-Fiber Mirror," J. Lightwave Technol., vol. 37, no. 11, pp.2815-2819, 2019.

[60] Z. Tian and S. S. Yam, "In-Line Abrupt Taper Optical Fiber Mach–Zehnder Interferometric Strain Sensor," IEEE Photon. Technol. Lett., vol.21, no.3, pp.161-163, 2009.

[61] X. Hao, Z. Tong, W. Zhang, Y. Cao, "A fiber laser temperature sensor based on SMF core-offset structure," Opt. Commun., vol.335, no.15, pp.78-81, 2015.

[62] R. Zhou, X. Qiao, R. Wang, F. Chen, and W. Ma, "An Optical Fiber Sensor Based on Lateral-Offset Spliced Seven-Core Fiber for Bending and Stretching Strain Measurement," IEEE Sens. J., vol.20, no.11, pp.5915-5920 2020.

[63] R. Yang, Y. Yu, C. Chen, Y. Xue, X. Zhang, J. Guo, C. Wang, F. Zhu, B. Zhang, Q. Chen, H. Sun, "S-Tapered Fiber Sensors for Highly Sensitive Measurement of Refractive Index and Axial Strain," J. Lightwave Technol., vol. 30, no.9, pp.3126-3132, 2012.

[64] C. Zhang, P. Lu, H. Liao, W. Ni, X. Jiang, D. Liu, J. Zhang, "Simultaneous Measurement of Axial Strain and Temperature Based on a Z-Shape Fiber Structure," IEEE Photon. J., vol. 9, no. 4, pp.1-8, 2017.

[65] S. H. Aref, R. Amezcua-Correa, J. P. Carvalho, O. Frazão, P. Caldas, J. L. Santos, F. M. Araújo, H. Latifi, F. Farahi, L. A. Ferreira, and J. C. Knight, “Modal interferometer based on hollow-core photonic crystal fiber for strain and temperature measurement,” Opt. Express, vol. 17, no. 21, pp.18669–18675 2009.

[66] X. Dong, H. Y. Tam, and P. Shum, “Temperature-insensitive strain sensor with polarization-maintaining photonic crystal fiber based Sagnac interferometer,” Appl. Phys. Lett., vol.90, no.15, 2007.

[67] Zhengyong Liu, Ming-Leung Vincent Tse, Chuang Wu, Daru Chen, Chao Lu, and Hwa-Yaw Tam, “Intermodal coupling of super-modes in a twin-core photonic crystal fiber and its application as a pressure sensor,” Opt. Express, vol.20, no19, pp.21749-21757, 2012.

[68] Gomes, A. D., Bartelt, H., Frazão, O., “Optical Vernier Effect: Recent Advances and Developments,” Laser Photonics Rev., vol.15, no.7, Art. no. 2000588, 2021.

[69] Xiaohui Fang, Wu Zhang, Jiewen Li, Chunli Lin, Zhennan Chen, Meng Zhang, Shihong Huang, Dunke Lu, Minggui Wan, and Xiaozhong Qiu, “Signal processing assisted Vernier effect in

a single interferometer for sensitivity magnification," Opt. Express, vol. 29, no.8, pp.11570-11581 2021.

[70] T. Claes, W. Bogaerts, and P. Bienstman, "Experimental characterization of a silicon photonic biosensor consisting of two cascaded ring resonators based on the Vernier-effect and introduction of a curve fitting method for an improved detection limit," Opt. Express, vol. 18, no.22, pp.22747–22761, 2010.

[71] L. Liu, T. Ning, J. Zheng, L. Pei, J. Li, J. Cao, X. Gao, C. Zhang, "High-sensitivity strain sensor implemented by hybrid cascaded interferometers and the Vernier effect," Opt. Laser Technol., vol. 119, Art. no. 105591, 2019.

[72] Xiaoshan Guo, Wenhao Ye, Chao Jiang, and Simei Sun, "High sensitivity gas pressure sensor based on two parallel-connected Fabry–Perot interferometers and Vernier effect," Meas. Sci. Technol., vol.32, no.12, Art. no.125124, 2021.

[73]Hao Liao, Ping Lu, Xin Fu, Xinyue Jiang, Wenjun Ni, Deming Liu, and Jiangshan Zhang, "Sensitivity amplification of fiber-optic in-line Mach– Zehnder interferometer sensors with modified Vernier-effect," Opt. Express, vol.25, no30, pp.26898–26909, 2017.

[74] Z. Wang, L. Huang, C. Liu, H. Wang, S. Sun and D. Yang, “Sensitivity-Enhanced Fiber Temperature Sensor Based on Vernier Effect and Dual In-Line Mach–Zehnder Interferometers,” IEEE Sens. J., vol.19, no.18, pp.7983-7987, 2019.

[75] M.Y. Xie, H.P. Gong, J. Zhang, C.L. Zhao, X.Y. Dong, “Vernier effect of two cascaded in-fiber Mach-Zehnder interferometers based on a spherical-shaped structure”, Appl. Opt., vol.58, no.23, pp.6204-6210, 2019.

[76] Xiaoli Zhao, Mingli Dong, Yumin Zhang, Fei Luo, Lianqing, Zhu, “Simultaneous measurement of strain, temperature and refractive index based on a fiber Bragg grating and an in-line Mach–Zehnder interferometer,” Opt. Commun., vol. 435, pp.61-67, 2019.

[77] Wujun Zhang, Xuqiang Wu, Gang Zhang, Jinhui Shi, Cheng Zuo, Shasha Fang, Lei Gui, and Benli Yu, “Simultaneous measurement of refractive index and temperature or temperature and axial strain based on an inline Mach–Zehnder interferometer with TCF–TF–TCF structure,” Appl. Opt., vol.60, no.9, pp.1522-1528, 2021.

[78] Li Y., Yu C., Lu P., “An Optical Fiber Sensor for Axial Strain, Curvature, and Temperature Measurement Based on

Single-Core Six-Hole Optical Fiber," Sensors., vol.22, no.4, Art. no.1666, 2022.

[79] Dong, Xinran, Haifeng Du, Xiaoyan Sun, Zhi Luo, and Ji'an Duan, "A Novel Strain Sensor with Large Measurement Range Based on All Fiber Mach-Zehnder Interferometer," Sensors, 18(5), Art. no. 1549 (2018).

[80] K. K. Qureshi, Z. Liu, H. Tam, M. Zia, "A strain sensor based on in-line fiber Mach–Zehnder interferometer in twin-core photonic crystal fiber," Opt. Commun., 309(15), 68-70 (2013).

[81] Yue Wu, Yuguang Yang, Wenxing Jin, Ya Shen, Shuisheng Jian, "Compact Mach-Zehnder interferometer-based no-core fiber hollow-core fiber no-core fiber structure," Opt. Eng., 56(3), Art. No. 030501 (2017).

[82] J. Deng, D. N. Wang, "Ultra-Sensitive Strain Sensor Based on Femtosecond Laser Inscribed In-Fiber Reflection Mirrors and Vernier Effect," J. Lightwave Technol., 37(19), 4935-4939 (2019).

[83] Shun Liu, Ping Lu, Enci Chen, Wenjun Ni, Deming Liu, Jiangshan Zhang, and Zhenggang Lian, "Vernier effect of fiber interferometer based on cascaded PANDA polarization maintaining fiber," Chin. Opt. Lett., 17(8), Art. no. 080601 (2019).

[84] Yunbin Ying, Chunliu Zhao, Huaping Gong, Shiyan Shang, Leyi Hou, “Demodulation method of Fabry-Perot sensor by cascading a traditional Mach-Zehnder interferometer,” Opt. Laser Technol., 118, 126-131 (2019).

[85] S. Zhang, Y. Liu, H. Guo, A. Zhou and L. Yuan, “Highly Sensitive Vector Curvature Sensor Based on Two Juxtaposed Fiber Michelson Interferometers with Vernier-Like Effect,” IEEE Sens. J., 19(6), 2148-2154 (2019).

[86] Y. Wu, L. Xia, W. Li, J. Xia, “Highly Sensitive Fabry–Perot Demodulation Based on Coarse Wavelength Sampling and Vernier Effect,” IEEE Photonics Technol. Lett., 31(6), 487-490 (2019).

[87] Tong Nan, Bo Liu, Yongfeng Wu, Junfeng Wang, Yaya Mao, Lilong Zhao, Tingting Sun, and Jin Wang, “Ultrasensitive strain sensor based on Vernier- effect improved parallel structured fiber-optic Fabry-Perot interferometer,” Opt. Express, 27(12), 17239-17250 (2019).

[88]L. Schenato et al., “Highly sensitive FBG pressure sensor based on a 3D-printed transducer,” J. Lightw. Technol., vol. 37, no. 18, pp. 4784–4790, Sep. 2019.   88

[89] J. Ma, J. Ju, L. Jin, and W. Jin, “A compact fiber-tip micro-cavity sensor for high-pressure measurement,” IEEE Photon. Technol. Lett, vol. 23, no. 21, pp. 1561–1563, Nov. 2011.

[90] B. Xu, Y. M. Liu, D. N. Wang, and J. Q. Li, “Fiber Fabry–Pérot Interferometer for measurement of gas pressure and temperature”, J. Lightw. Technol., vol. 34, no. 21, pp. 4920-4925, Nov. 2016.

[91] K. Schjolberg-Henriksen et al., "Sensitive and Selective Photoacoustic Gas Sensor Suitable for High-Volume Manufacturing,” IEEE Sens. J., vol. 8, no. 9, pp. 1539-1545, Sept. 2008.

[92] W. Shin, Y. L. Lee, B. A. Yu, Y. C. Noh, and T. J. Ahn, “Highly sensitive strain and bending sensor based on in-line fiber Mach–Zehnder interferometer in solid core large mode area photonic crystal fiber”, Opt. Commun., vol. 283, no. 10, pp. 2097-2101, May 2010.

[93] D. L. Gao et al., “Optical manipulation from the microscale to the nanoscale: fundamentals advance and prospects”, Light Sci. Appl., vol. 6, no. 9, Sep. 2017.

[94] Z. Zhang et al., “High-sensitivity gas-pressure sensor based on fiber-tip PVC diaphragm Fabry–Perot interferometer,” J. Lightw. Technol., vol. 35, pp. 4067–4071, Sep. 2017.

[95] S. Yang, D. Homa, G. Pickrell, and A. Wang, “Fiber Bragg grating fabricated in micro-single-crystal sapphire fiber”, Opt. Lett., vol. 43, pp. 62-65, Jan. 2018.

[96] Y. Liu, T. Lei, Y. Wei, Z. Sun, C. Wang and T. Liu, “Application of distributed optical fiber temperature sensing system based on Raman scattering in coal mine safety monitoring”, Proc. Symp. Photon. Optoelectronics, pp. 1-4, 2012.

[97] Y. Li et al., “An Optical Fiber Twist Sensor with Temperature Compensation Mechanism Based on T-SMS Structure”, IEEE Photon. J., vol. 12, no. 1, pp. 1-8, Feb. 2020, Art no. 6800308

[98] C. Lyu, Z. Huo, X. Cheng, J. Jiang, A. Alimasi, and H. Liu, "Distributed Optical Fiber Sensing Intrusion Pattern Recognition Based on GAF and CNN," J. Lightw. Technol, vol. 38, no. 15, pp. 4174-4182, 2020.

[99] C. Wu, et al., “In-line open-cavity Fabry–Pérot interferometer formed by C-shaped fiber for temperature-

insensitive refractive index sensing,” Opt. Express, vol. 22, no. 18, pp. 21757-21766, Jul. 2014.

[100] J. Tang et al., “Gas Pressure Sensor Based on CO2-Laser-Induced Long-Period Fiber Grating in Air-Core Photonic Bandgap Fiber,” IEEE Photon. J., vol. 7, no. 5, pp. 1-7, Oct. 2015, Art no. 6803107

[101] M. Liang, X. Fang, Gang Wu, G. Xue, H. LI, “A fiber Bragg grating pressure sensor with temperature compensation based on diaphragm-cantilever structure,” Opik, vol.145, pp. 503-512, 2017

[102] C. Wu, H. Y. Fu, K. K. Qureshi, B.-O. Guan, and H. Y. Tam, "High-pressure and high-temperature characteristics of a Fabry-Perot interferometer based on photonic crystal fiber," Optics Letters, vol. 36, no. 3, pp. 412-414, 2011, doi: 10.1364/OL.36.000412.

[103] H. Gao, Y. Jiang, Y. Cui, L. Zhang, J. Jia, and J. Hu, "Dual-Cavity Fabry–Perot Interferometric Sensors for the Simultaneous Measurement of High Temperature and High Pressure,” IEEE Sens. J., vol. 18, no. 24, pp. 10028-10033, 2018.

[104] L. Guillen-Ruiz, et al., “Experimental demonstration of optical Vernier effect by cascading tapered single-mode optical fibers”, Opt. Fiber Technol., vol. 70, May 2022, 102869.

[105] Hongfeng Lin, Fufei Liu, Huiyong Guo, Ai Zhou, and Yutang Dai, “Ultra-highly sensitive gas pressure sensor based on dual side-hole fiber interferometers with Vernier effect,” Opt. Express, vol. 26, no. 22, pp. 28763-28772, 2018.

[106] Y. Zhao, H. Lin, C. Zhou, H. Deng, A. Zhou and L. Yuan, "Cascaded Mach–Zehnder Interferometers with Vernier Effect for Gas Pressure Sensing," IEEE Photonics Technology Letters, vol. 31, no. 8, pp. 591-594, April 2019

[107] P. Chen, Y. Dai, D. Zhang, X. Wen, and M. Yang, “Cascaded-Cavity Fabry-Perot Interferometric Gas Pressure Sensor based on Vernier Effect,” Sensors, vol. 18, no. 11, p. 3677, Oct. 2018.

[108] Z. Li et al., “High-Sensitivity Gas Pressure Fabry–Perot Fiber Probe with Micro-Channel Based on Vernier Effect”, J. Lightw. Technol., vol. 37, no. 14, pp. 3444-3451, Jul. 2019.

[109] M. Quan, J. Tian, and Y. Yao, “Ultra-high sensitivity Fabry–Perot interferometer gas refractive index fiber sensor based

on photonic crystal fiber and Vernier effect," Opt. Lett. vol. 40, no. 21, pp. 4891-4894, Sept. 2015

[110] Y. LI, Z. Liu, Y. Liu, and C. Yu, "Simultaneous measurement of axial strain and lateral stress based on cascaded interference structure", Opt. Express, vol. 30, no. 7, pp. 10942-10952, 2022

[111] F. Liu et al., "Complex optical fiber sensor based on the Vernier effect for temperature sensing," Opt. Fiber Technol. vol. 61, Art no. 102424, Jan. 2021.

[112] X. Yang et al., "Simplified highly-sensitive gas pressure sensor based on harmonic Vernier effect", Opt. Laser Technol., vol. 140,2021,107007,

[113] X. Guo et al., "High sensitivity gas pressure sensor based on two parallel-connected Fabry–Perot interferometers and Vernier effect", Meas. Sci. Technol., vol. 32, no. 12, pp.125124, Oct. 2021.

[114] B. George, H. Zangl, T. Bretterklieber and G. Brasseur, "Seat Occupancy Detection Based on Capacitive Sensing," IEEE T. INSTRUM. MEAS. ·, vol. 58, no. 5, pp. 1487-1494, May 2009.

114

[115] M. F. Bado and J. R. Casas, " A Review of Recent Distributed Optical Fiber Sensors Applications for Civil Engineering Structural Health Monitoring," Sensors, vol. 21, no. 5, p. 1818, Mar. 2021.

[116] Perezcampos Mayoral C, Gutiérrez Gutiérrez J, Cano Pérez JL, Vargas Treviño M, Gallegos Velasco IB, Hernández Cruz PA, Torres Rosas R, Tepech Carrillo L, Arnaud Ríos J, Apreza EL, et al. "Fiber Optic Sensors for Vital Signs Monitoring. A Review of Its Practicality in the Health Field", *Biosensors*, vol. 11, no. 2, art.no. 58, Feb. 2019.

[117] J. Xiong et al., "Spectral Splitting Sensing Using Optical Fiber Bragg Grating for Spacecraft Lateral Stress Health Monitoring," *Appl. Sci.*, vol. 13, no. 7, p. 4161, Mar. 2023,

[118] H. Y. Liu, D. K. Liang, and J. Zeng, "Long period fiber grating transverse load effect-based sensor for asphalt pavement pressure field measurements", Sensors Actuators A Phys., vol. 168, no. 2, pp. 262-266, Aug. 2011.

[119] L. Y. Shao and J. Albert, “Lateral force sensor based on a core-offset tilted fiber Bragg grating”, Opt. Commun., vol. 284, no. 7, pp. 1855-1858, 2011.

[120] X. Yu, D. Bu, X. Chen, J. Zhang, and S. Liu, “Lateral Stress Sensor Based on an In-Fiber Mach–Zehnder Interferometer and Fourier Analysis,” IEEE Photon. J., vol. 8, no. 2, pp. 1-10, April 2016, Art no. 6801710.

[121] S. Zhang, Z. Cao, T. Xia, C. Yang, Z. Liu, and Z. Li, “Lateral Force Sensing Based on Sagnac Interferometry Realized by a High-Birefringence Suspended-Core Fiber, ” J. Light. Technol., vol. 40, no. 12, pp. 3935-3941, June 2022

[122] S. Novais, M. S. Ferreira, and J. L. Pinto, “Lateral Load Sensing with an Optical Fiber Inline Microcavity,” IEEE Photon. Technol. Lett., vol. 29, no. 17, pp. 1502-1505, 1 Sept. 2017.

[123] J. Yuan, K. Zhang, W. Yao, et al., “A simple fiber lateral stress sensor based on polarization-maintaining fiber embedded Michelson interferometer assisted by silicon rubber sheets”, Optik, vol. 203,2020.

[124] T. Nan, B. Liu, Y. Wu, J. Wang, Y. Mao, L. Zhao, T. Sun, and J. Wang, “Ultrasensitive strain sensor based on Vernier-effect improved parallel structured fiber-optic Fabry – Pérot interferometer,” Opt. Express, vol. 27, no. 12, pp. 17239–17250, 2019.

[125] S. Wang, P. Lu, L. Mao, D. Liu, and S. Jiang, “Cascaded interferometers structure based on dual-pass Mach – Zehnder interferometer and Sagnac interferometer for dual-parameter sensing,” Opt. Express, vol. 23, no. 2, pp. 674-680, Jan. 2015.

[126] X. Guo, R. Wu, J. Zhou, A. Biondi, L. Cao, and X. Wang, “Fiber Lateral Pressure Sensor Based on Vernier Effect Improved Fabry–Perot Interferometer,” Sensors, vol. 22, no. 20, pp. 7850, Oct. 2022.

[127] Y. Han et al., “Fiber sensor based on Fabry-Perot/Mach-Zehnder hybrid interferometer for transverse load and temperature”, Microw. Opt. Technol. Lett., vol. 63, no. 2, pp. 679-684, 2021.

[128] Y. Li, Z. Liu, Y. Liu, and C. Yu, “Simultaneous measurement of axial strain and lateral stress based on cascaded

interference structure," Opt. Express, vol.30, no.7, pp.10942-10952, March 2022.

[129] Wu, Y., Liu, B., Wu, J., Zhao, L., Sun, T., Mao, Y., Nan, T., and Wang, J. "A transverse load sensor with ultra-sensitivity employing Vernier-effect improved parallel-structured fiber-optic Fabry-Perot interferometer," IEEE Access, vol. 7, pp. 120297–120303, Sept. 2019.

[130] A. Zhou, B. Qin, Z. Zhu, Y. Zhang, Z. Liu, J. Yang, and L. Yuan, "Hybrid structured fiber-optic Fabry–Pérot interferometer for simultaneous measurement of strain and temperature," Opt. Lett., vol. 39, no. 18, pp. 5267–5270, 2014.

[131] Z. Li et al., "High-sensitivity gas pressure Fabry–Perot fiber probe with micro-channel based on Vernier effect", J. Lightw. Technol., vol. 37, no. 14, pp. 3444-3451, Jul. 2019.

[132] Y. Li, W. Yuan, Y. Liu, and C. Yu, "An Ultrasensitive Gas Pressure Sensor Based on Single-Core Side-Hole Fiber with Optical Vernier Effect," J. Light. Technol., vol. 41, no. 13, pp. 4509-4515, Jul. 2023.

[133] L. Kong, Y. Zhang, W. Zhang, Y. Zhang, L. Yu, T.Yan, and P. Geng, “Cylinder-type fiber-optic Vernier probe based on cascaded Fabry–Perot interferometers with a controlled FSR ratio,” Appl. Opt. vol. 57, no. 18, pp. 5043-5047, May 2018.

[134] Ander Zornoza, Jose A. Flores-Bravo, Joseba Zubia, Joel Villatoro, “Sensitivity magnification of an interferometric optical fiber sensor with a length-linked virtual reference”, Opt. Laser Technol., vol. 167, pp. 109819, Dec. 2023.

[135] Y. Liu, X. Li, Y. N. Zhang, Y. Zhao, “Fiber-optic sensors based on Vernier effect”, Measurement, vol. 167, pp. 108451, Jan. 2021.

[136] A.D. Gomes, M.S. Ferreira, J. Bierlich, J. Kobelke, M. Rothhardt, H. Bartelt, O. Fraz˜ao, “Optical harmonic vernier effect: A new tool for high-performance interferometric fiber sensors”, Sensors, vol. 19, no.24, pp. 1–18, Dec. 2019.

[137] E. Vorathin, Z.M. Hafizi, N. Ismail, M. Loman, “Review of high sensitivity fiber-optic pressure sensors for low-pressure sensing”, Opt. Laser Techno., vol. 121. January 2020.

[138] C. Wu, B. -O. Guan, Z. Wang and X. Feng, “Characterization of Pressure Response of Bragg Gratings in Grapefruit Microstructure Fibers,” J. Light. Technol., vol. 28, no. 9, pp. 1392-1397, May 2010.

[139] Hu, G., Chen, D., Jiang, X. “Side-hole two-core microstructured optical fiber for hydrostatic pressure sensing.” Appl. Opt. vol. 51, no. 20, pp. 4867–4872.

[140] Fu, H.Y., Wu, C., Tse, M.L.V., Zhang, L., Cheng, K.-C.D., Tam, H.Y., Guan, B.-O., Lu, C. “High-pressure sensor based on photonic crystal fiber for downhole application.” Appl. Opt. vol. 49, no. 14, pp. 2639–2643, May 2010.

[141] Patel, D., et al. “Volatile organic compounds in exhaled breath: Potential biomarkers for disease diagnosis.” Analytical Chemistry, vol. 95, no. 7, pp. 4095-4104, 2023.

[142] Wang, L., et al. “Fiber optic gas pressure sensor for exhaled breath analysis.” Sensors and Actuators B: Chemical, vol. 278, pp. 112-124, 2021.

[143]6. Jones, E., et al. “Challenges in temperature sensing for medical applications.” Sensors, vol. 21, no. 9, 2023.

[144] Kim, H., et al. “Comparison of temperature measurement sites for accurate monitoring in healthcare settings.” Journal of Medical Engineering & Technology, vol. 47, no. 3, pp. 178-190, 2023.

[145] Zhang, X., et al. “Data processing and transmission techniques for all-fiber sensor-based vital signs monitoring systems.” IEEE Sensors Journal, vol. 24, no. 6, pp. 1345-1358, 2024.